3-11-2011

Performance Characterization of a Novel Plasma Thruster to Provide a Revolutionary Operationally Responsive Space Capability with Micro- and Nano-Satellites

John-David C. De la Harpe

PERFORMANCE CHARACTERIZATION OF A NOVEL PLASMA THRUSTER TO PROVIDE A REVOLUTIONARY OPERATIONALLY RESPONSIVE SPACE CAPABILITY WITH MICRO- AND NANO-SATELLITES

THESIS

John-David C. de La Harpe, Captain, USAF

AFIT/GA/ENY/11-M02

DEPARTMENT OF THE AIR FORCE
AIR UNIVERSITY

AIR FORCE INSTITUTE OF TECHNOLOGY

Wright-Patterson Air Force Base, Ohio

AFIT/GA/ENY/11-M02

PERFORMANCE CHARACTERIZATION OF A NOVEL PLASMA THRUSTER TO PROVIDE A REVOLUTIONARY OPERATIONALLY RESPONSIVE SPACE CAPABILITY WITH MICRO- AND NANO-SATELLITES

THESIS

Presented to the Faculty

Department of Aeronautics and Astronautics

Graduate School of Engineering and Management

Air Force Institute of Technology

Air University

Air Education and Training Command

In Partial Fulfillment of the Requirements for the

Degree of Master of Science in Astronautical Engineering

John-David C. de La Harpe, BS

Captain, USAF

March 2011

AFIT/ENY/11-M02

PERFORMANCE CHARACTERIZATION OF A NOVEL PLASMA THRUSTER TO PROVIDE A REVOLUTIONARY OPERATIONALLY RESPONSIVE SPACE CAPABILITY WITH MICRO- AND NANO-SATELLITES

John-David C. de La Harpe, BS
Captain, USAF

Approved:

Lt Col Richard E. Huffman, Jr. (Chairman)	11 Mar 11 Date
William A. Hargus, Jr., PhD (Member)	3 March 2011 Date
Lt Col Carl R. Hartsfield (Member)	15 Mar 11 Date
Lt Col Richard D. Branam (Member)	3 Mar 2011 Date

Abstract

Few options currently exist to provide propulsion for extremely small satellites due to design constraints on power, volume, and weight. However, future operation will require a capability to conduct orbital maneuvers, momentum dumping, and precision pointing for these low cost satellites. The research presented here represents the first effort to operate and quantify the performance of a new micro plasma thruster design which provides a novel solution to these disparate competing constraints. The thruster in this study represents a deviation from traditional circular Hall thruster design practices, because it eschews a central magnetic circuit, which results in nearly parallel electric and magnetic field lines within the thruster discharge channel. This design decision reduces thruster complexity and thermal susceptibility, but it also reduces the ionization efficiency. The cornerstone of this study involved the direct measurement of thrust in order to quantify the efficiency and specific impulse of this innovative thruster. The investigation also included characterization of the thruster exhaust plume, voltage-current characteristics, and operating limits. Results are enumerated and suggestions for improvement provided.

I dedicate this body of work my wife, who has simultaneously handled the tasks of completing her Ph.D. and caring for a husband, home, and cat with a deft grace and intelligence that belies her mortal nature. She is my singular salient source of gravity, beauty, and inspiration.

Acknowledgements

I would like to thank Lt Col Huffman, my thesis advisor, for his wisdom, patience, and unfailing trust. I would like to thank Lt Col Branam for his instruction and infectious enthusiasm that formed the basis upon which this endeavor began. I would like to thank Lt Col Hartsfield for his original ideas and many enjoyable conversations. I would like to thank Dr. William Hargus for his personal guidance and the contribution he has made to the field of electric propulsion, which served to enlighten my path early in the development of this project. It is with gratitude that I recognize the support and guidance provided by Jay Anderson and his team of lab technicians: John Hixenbaugh, Wilbur Lacy, Berry Page, and Chris Zickefoose. For their outstanding technical support, I recognize the contributions of Bruce Pote and Surjeet Paintal of Busek. I would also like to acknowledge the support of Mr. Michael Huggins of AFRL/RZS. It is with admirations and respect that I would like to recognize the help I received from Capt Lee Watson, LCDR Spencer "Silverback" Tempkin, and Capt Dave Liu while working in the SPASS laboratory. I would like to thank the Air Force for entrusting me with the last 18 months to hone my technical skills and grow as a technical leader in the aerospace community.

John-David C. de La Harpe

Table of Contents

Page

Page

List of Figures

Page

Page

Page

List of Tables

Page

List of Symbols

σ_{abs}	Absorption Cross-Sectional Area
$\dot{m}_a$	Anode Mass Flow Rate
$\vec{E}$	Applied Electric Field
$\bar{v}$	Average Propellant Velocity
$v_{\perp}$	Azimuthal Velocity
I_b	Beam Current
η_b	Beam Current Efficiency
V_b	Beam Voltage
k_B	Boltzmann's constant
Δb_{cal}	Calibration Bias
F_{cal}	Calibration Force
V_{cal}	Calibration Voltage
$\dot{m}_c$	Cathode Mass Flow Rate
ΔE	Change in Energy to Induce Specific Electron Energy State Jump
(ΔV)	Change in Velocity to Meet Mission Requirement
q	Charge of a Particle
γ	Correction Factor
g_i	Degeneracy from Electron Transitioning
I_d	Discharge Current
P_d	Discharge Power
V_d	Discharge Voltage
Θ	Divergence Angle
g_0	Earths Gravity at Sea Level $\left(9.80665\,\frac{m}{s^2}\right)$
A_{21}	Einstein Spontaneous Emission Rate Coefficient
η_o	Electrical Utilization Efficiency
e^-	Electron
n_e	Electron Density
E_1	Electron Energy at State 1
E_2	Electron Energy at State 2
m_e	Electron mass
T_e	Electron Temperature
v_e	Exit Velocity
F_t	Geometric Efficiency
$J(r)$	Ion Current Density
$\dot{m}_i$	Ion Mass Flow Rate
P_k	Keeper Power

r_L	Larmour Radius
$\vec{F}$	Lorentz Force
$\vec{B}$	Magnetic Field Strength
P_{mag}	Magnetic Power
$\dot{m}$	Mass Flow Rate
m	Mass of Particle
m_{prop}	Mass of Propellant
η_m	Mass Utilization Efficiency
λ_{MFP}	Mean Free path
μ	Normal Distribution Average
σ	Normal Distribution Standard Deviation
N_i	Number Density of Particles
I^{++}	Number of Doubly Ionized Atoms
n	Number of Samples in Population
I^{+}	Number of Singly Ionized Atoms
$\vec{v}$	Particle Velocity
l	Path Length
f	Photon Frequency
h	Plank's Constant $(4.13566733 \times 10^{-15}\ eV - s)$
r_p	Probe radius
Δb_{res}	Resolution Bias
I_{sp}	Specific Impulse
c	Speed of Light
t	Statistical Value
T	Thrust
F_a	Thrust Asymmetry Factor
α	Thrust Correction Factor
η_{Thrust}	Thrust Efficiency
Δb_d	Thrust Stand Drift
η_T	Total Efficiency
P	Total System Power
η_V	Voltage Ratio
λ	Wavelength

List of Abbreviations

AFIT	Air Force Institute of Technology
AFRL	Air Force Research Laboratory
BN	Boron nitride
CHT	Circular Hall Thruster
COMSAT	Communication satellite
EP	Electric Propulsion
ESA	European Space Agency
ESD	Electrostatic Discharge
HET	Hall effect thruster
HIVAC	High Voltage Hall Accelerator
LEO	Low Earth Orbit
LDS	Laser Displacement System
LVDT	Linear variable differential transformer
NASA	National Aeronautics and Space Administration
NRO	National Reconnaissance Office
NSSK	North-south station keeping
PPU	Power Processing Unit
SE	Standard Error
SMART	Small Missions for Advanced Research in Technology
SmCo	Samarium Cobalt
SPASS	Space Propulsion Analysis and Systems Simulation
SRG	Stirling Radioisotope Generator
STEX	Science Technology Experiments
UHT	Ultra-high temperature
US	United States
USSR	Union of Soviet Socialist Republics

PERFORMANCE CHARACTERIZATION OF A NOVEL PLASMA THRUSTER TO PROVIDE A REVOLUTIONARY OPERATIONALLY RESPONSIVE SPACE CAPABILITY WITH MICRO- AND NANO-SATELLITES

I. Introduction

The extraordinary cost associated with placing space vehicles into orbit (~12,000 dollars per kilogram) has served to justify significant research and development in order to identify the highest performing and most efficient sources of thrust for these vehicles [1]. Over the last 50 years, such efforts have revealed electric propulsion holds the greatest promise to fill most on-orbit needs and has become the only viable source for interstellar propulsion, as illustrated by Table 1. Nonetheless, no single propulsion technology has proven equally adept at meeting the needs of every conceivable mission. Instead, space vehicle designers must weigh factors such as specific impulse, efficiency, and system weight in order to identify the best thruster for a specific application.

Table 1. Typical propulsion performance characteristics, based on Humble [2].

Technology	Specific Impulse (s)			Thrust (N)		
Cold Gas				0.1	--	50
N_2	60					
H_2	250					
Chemical				0.01	--	12,000,000
Liquid						
Monopropellant	140	--	235			
Bipropellant	320	--	460			
Solid	260	--	300			
Hybrid	290	--	350			
Electric				0.0001	--	20
Electrothermal	500	--	1,000			
Electromagnetic	1,000	--	7,000			
Electrostatic	2,000	--	10,000			

Problem Statement

Busek Co., Inc., under contract with the Air Force Institute of Technology, has developed a unique circular magnet thruster design which underwent preliminary characterization as part of this study. The investigation included creation of voltage-current (V-I) curves, measurement of beam current using a Faraday probe, and direct measurement of thrust using a torsion balance. Results from these tests suggest this thruster, named the Busek BHT-20, behaves like a circular micro-Hall thruster in many ways, but has some peculiarities which will require further investigation in order to fully understand both their cause and impact on overall thruster performance. The current iteration of this design includes an ionization and acceleration chamber comprised of an opened ended circular section with the walls of the cylinder being made of boron nitride (BN). Surrounding the BN insulator is a cylindrical 0.135 Tesla samarium cobalt (SmCo) permanent magnet from Electron Energy Corp. in Landisville, PA. Encapsulating the assembly is a simple aluminum housing, as illustrated by Figure 1. At the entrance to the ionization chamber is a traditional stainless steel anode with a four-hole frit for xenon gas distribution. The center of the anode is covered with a 3.175 mm BN post. During initial testing, this thruster was paired with a 3.175 mm Busek BHC-1500 cathode. The geometry and manufacture of this device is straightforward when compared to traditional Hall effect thrusters, as illustrated by Figure 2; however, this new concept seeks to address several challenges relating to the use of previous designs for very small satellites including power consumption, lifetime, and thruster complexity.

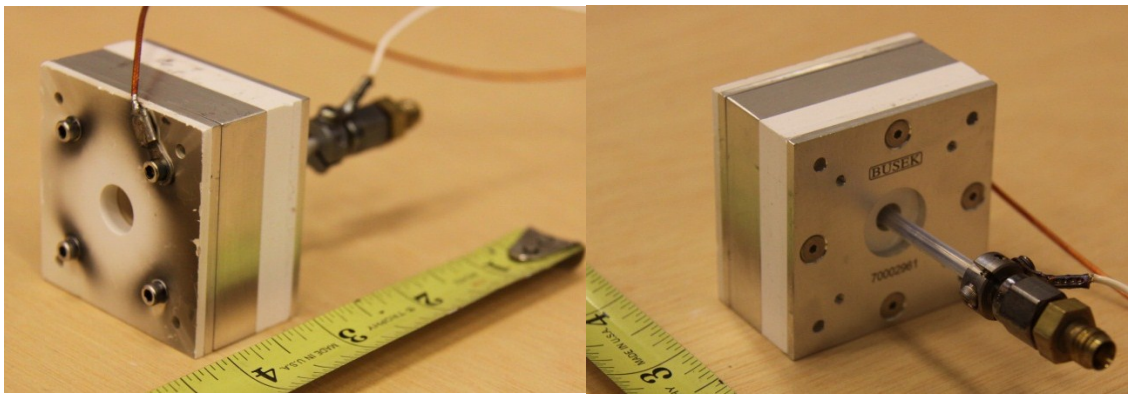

a) Front view of BHT-20. b) Back view of BHT-20.

Figure 1. Views of the BHT-20 thruster illustrating size and construction.

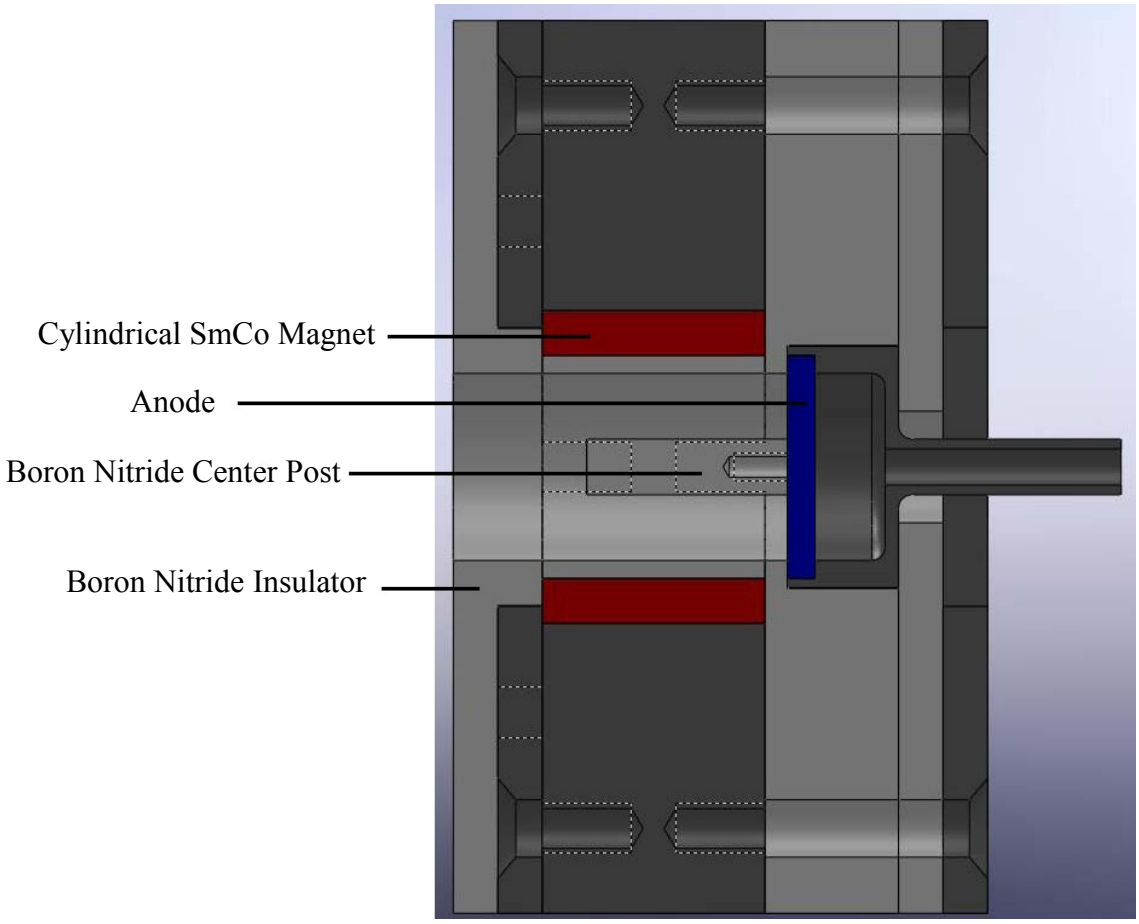

Figure 2. Cross-sectional diagram of BHT-20 thruster illustrating key components, taken from Paintal [3].

The layout of this thruster and the use of a permanent magnet are expected to reduce internal degradation, as compared to traditional designs, and enable acceptable efficiencies for the size class in which it operates. The primary failure mechanism for a typical Hall effect thrusters is sputtering erosion caused by plume impingement on the walls and mouth of thruster that slowly erode the insulator protecting the magnet assembly [4]. The strength and orientation of the magnetic field created by the SmCo magnet is sufficient to induce a magnetic pressure that contains the preponderance of the plasma within a narrow channel in the center of the thruster, as illustrated in Figure 3. Initial tests, representing more than 70 hours of operation, do not show any visible signs of erosion, which serve to justify further investigation into this point. The use of a permanent magnet is also ideal for a micro-Hall thruster – reducing the complexity of the thruster and improving the overall efficiency of the propulsion system by eliminating the current necessary to operate traditional electromagnets. Nevertheless, this design does pose some unique challenges.

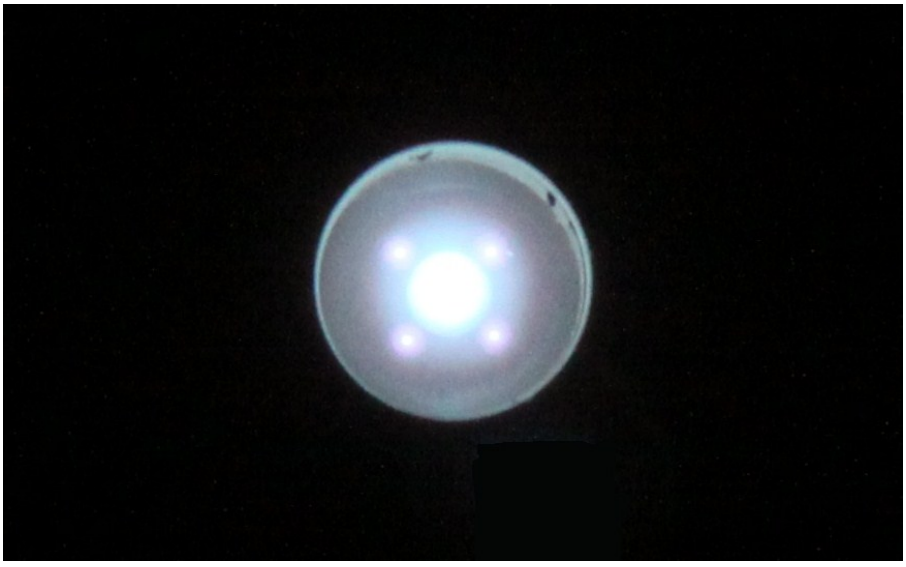

Figure 3. Thruster discharge channel during low power operation.

Inherent in the use of a permanent magnet is an acknowledgement of its operating limits in order to achieve a desirable lifetime for a low thrust space thruster. Over the last decade, work was performed to vastly improve the thermal stability and radiation resistance of rare earth permanent magnets for applications such as ion thrusters and high efficiency Stirling Radioisotope Generators (SRG) [5]. A relatively new class of ultra-high temperature (UHT) SmCo magnets has demonstrated minimal (less than 0.5%) magnetic irreversible losses at temperatures of 300°C over a period of three years. At higher temperatures (greater than 550°C) even the most thermally stable SmCo magnets will provide reduced flux densities. An accurate understanding of the thermal distribution of this new plasma thruster during operation is therefore a necessary component of future investigations. Throughout tests conducted for this project a record of magnetic field strength was maintained in order to determine if any degradation in magnet performance took place while testing. During this inaugural study, no loss of magnetic field strength could be identified using an F. W. Bell 5180 Gaussmeter. The baseline plot of magnetic field strength along the centerline of the plasma discharge channel is provided in Figure 4. This plot depicts typical behavior for a nearly uniformly charged hollow magnetic cylinder. The concentration of B-field lines reaches its maximum at the center of the channel and this concentration drops off quadratically in either direction from this point.

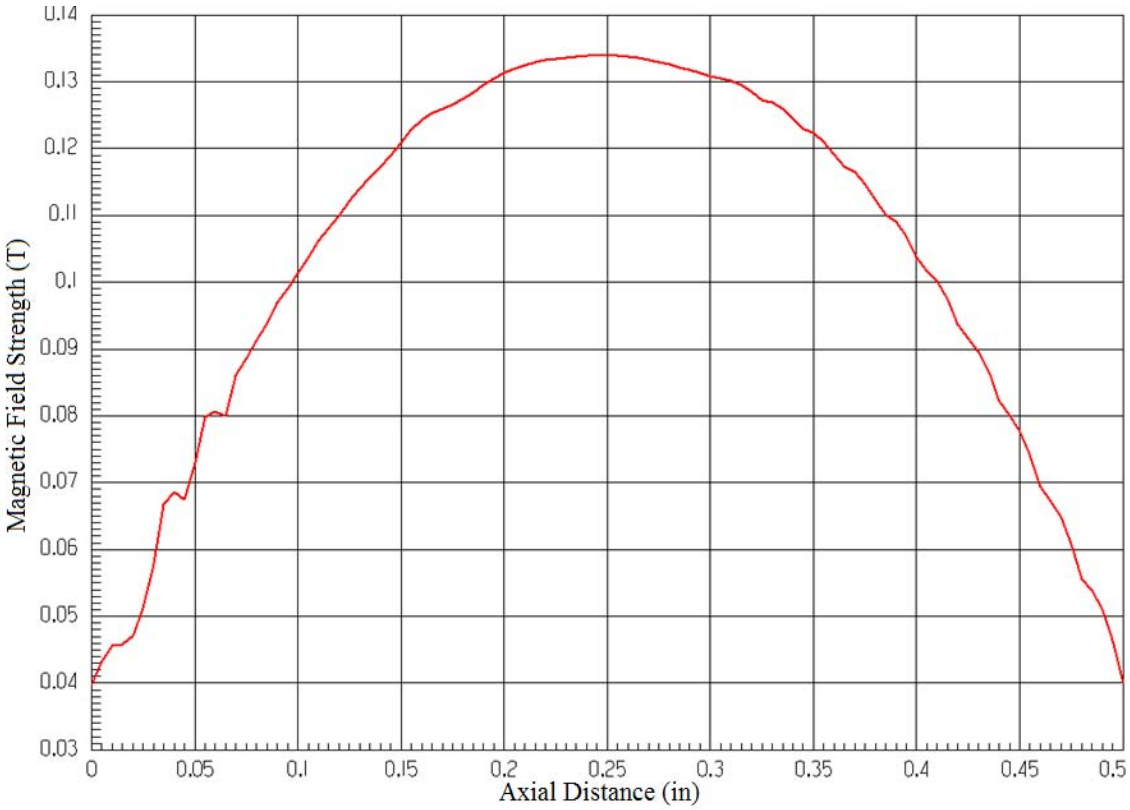

Figure 4. Magnetic field strength along thruster discharge channel, taken from Paintal [3].

The unusually small size and mass flow rate of this thruster complicates other aspects as well; initial tests have suggested that the operation of this thruster is intimately related to placement of the external cathode. This placement is partially due to the nature of this new thruster, but geometric constraints of the current configuration clearly have an impact. The outer diameter of the current hollow cathode with enclosed geometry keeper is significant, as illustrated in Figure 5. The size of this cathode not only limits its viable orientation, but it also would prove troublesome if trying to integrate the thruster onto a small space vehicle, such as a CubeSat. The employment of either a micro-hollow cathode or a lanthanum hexaboride single crystal emitter relying on ohmic heating to generate electrons will be explored in future research. Advantages to the latter being a

significant portion of the xenon propellant will not be used by the cathode itself (significant loss mechanism), as well as avoiding any asymmetric thrust created by the cathode itself. A BHT-20 specific cathode would represent a significant improvement, but it was decided that performance characterization of the existing system was more pressing. The value of this thruster concept can only be accurately communicated by performance figures of merit: thrust, specific impulse, and various measures of efficiency. The measurement of these attributes is based on traditional Hall thruster relationships and theory.

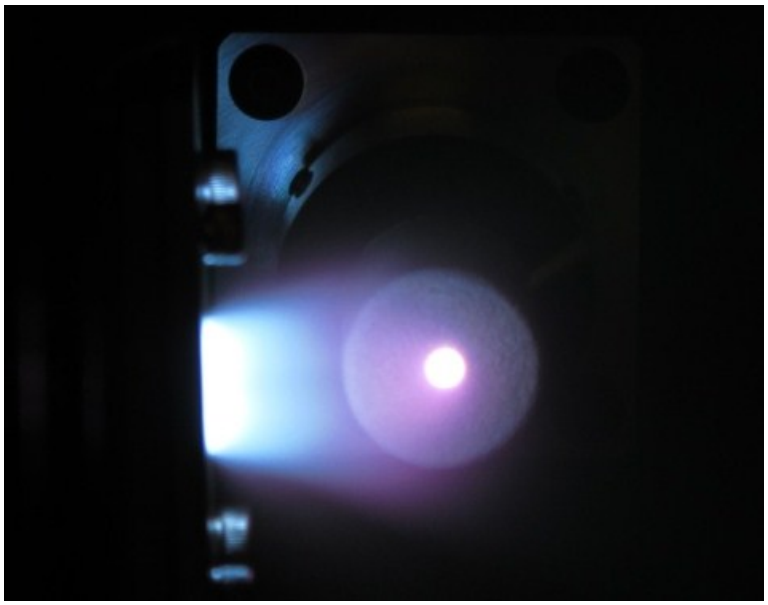

Figure 5. BHT-20 during operation, illustrating the large relative cross-section of the cathode to the plasma plume itself.

Research Objectives

The objective of this research effort is to quantify the performance of this novel deviation from traditional micro-Hall thruster designs, in-terms of thrust, specific impulse (I_{sp}), and efficiency. This research will use xenon for the propellant in the BHT-20. The thrust produced will be measured using a torsion balance system, which can resolve

micro-Newton forces. The thrust measurement in conjunction with measurements of propellant flow, cathode potential, and anode potential will be used to quantify I_{sp} and efficiency. A Faraday probe will be used to measure the current density within the plasma plume at various radii in order to determine the ion distribution and beam efficiency. Erosion of the boron nitride insulating material and magnetic field strength will be monitored in order to determine operational limits for the thruster and to determine viability for prolonged usage in the space environment. This information will factor into a judgment regarding the viability of this technology to fulfill various applications within the space propulsion regime to include precision attitude control for ESPA class and larger satellites and primary propulsion for CubeSats.

II. Theory and Previous Research

This chapter provides background information on the operation of Hall effect thrusters and methods to characterize their performance. A discussion of the physics governing Hall effect thrusters is included. Typical applications for this thruster design and inherent limitations are also explored. The diagnostic techniques that are used in this study are introduced along with experimental considerations. Finally, the relationships describing Hall thruster efficiency are introduced.

Hall Thrusters

Hall thrusters are included under the broad category of electric propulsion systems, because the mechanism by which these devices generate force involves imparting electric energy to ionized particles, which in-turn are accelerated to high velocity in order to achieve an efficient momentum transfer. Electrostatic and electromagnetic thrusters are the two most common forms for an electric propulsion device. Both approaches generate thrust using the Lorentz force [2].

$$\vec{F} = q\left(\vec{E} + \vec{v} \times \vec{B}\right) \tag{1}$$

The Lorentz force is equal to the product of the charge of the moving particles (q) and the sum of the applied electric field $\left(\vec{E}\right)$ and the cross product of the particles velocity $(\vec{v})$ and the magnetic field strength $\left(\vec{B}\right)$. Hall effect thrusters and ion thrusters are termed electrostatic thrusters because they use the qE component of the Lorentz force to generate thrust. Hall effect thrusters transfer momentum by using the axial electric field from the anode to accelerate the charged ions. The physics model to explain this

process in more detail is involved, but the physical form it necessitates is not, as illustrated by Figure 6.

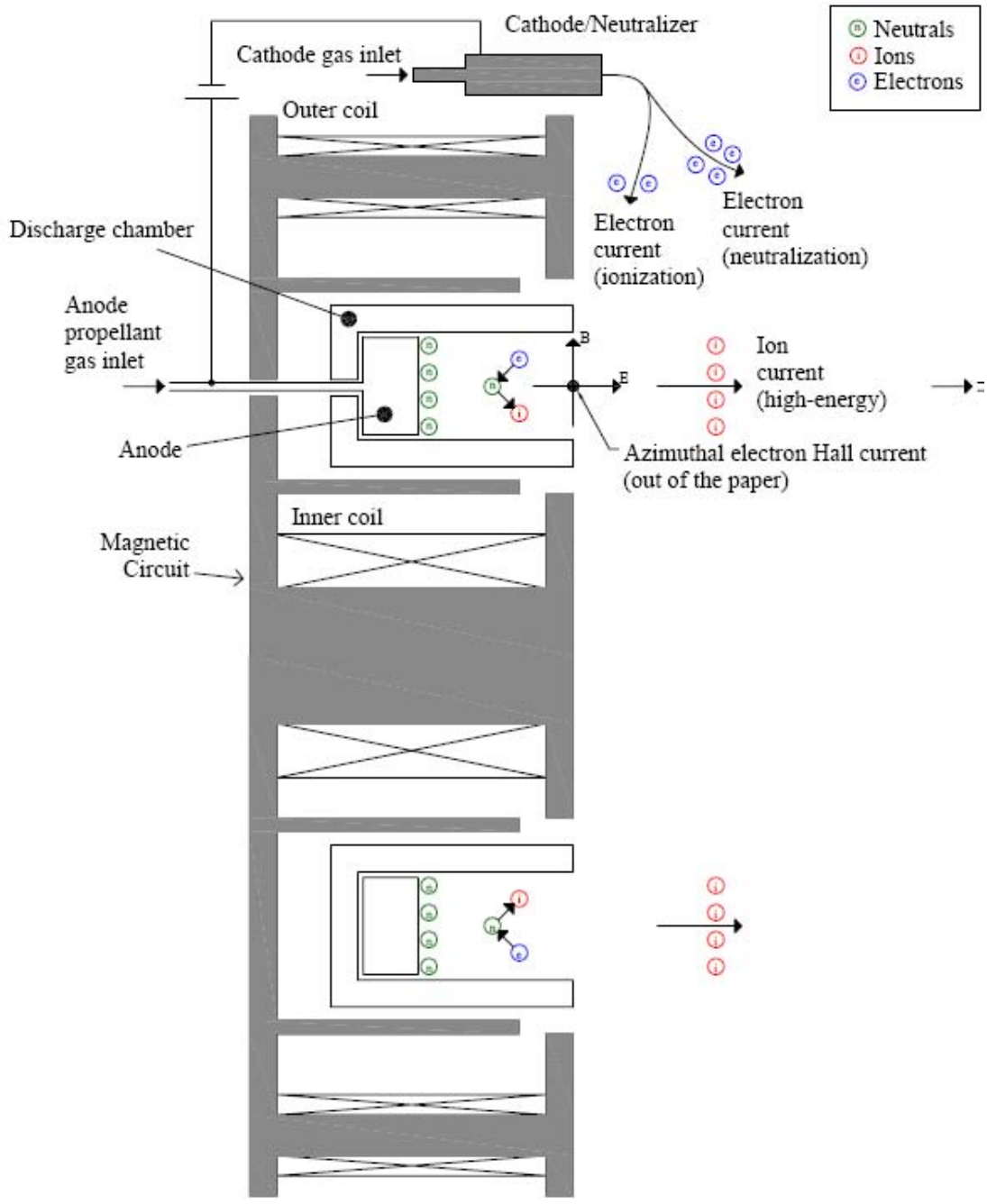

Figure 6. Hall effect thruster cross sectional view, taken from Warner [6].

Hall effect thrusters are commonly composed of an annular channel with walls made from an insulator, such as BN, and an anode and propellant dispersion medium at the inlet. A cathode is commonly mounted externally near the exit of this channel in order to produce electrons to neutralize the positively charged ions in the plasma plume. This is necessary to prevent a charge buildup on the spacecraft and the resulting back streaming of ions that would net no thrust [7]. The cathode can also be mounted down the centerline of the thruster, but this is less typical. Typically, within the inner BN cylinder and outside the outer BN cylinder are permanent or electromagnets that produce a radial magnetic field perpendicular to the BN walls. External to the thruster is a power supply that links the anode and cathode in order to generate the axial electric field.

Hall effect thruster operation starts from the fraction of the electron current generated by the cathode that is used for ionization. These electrons flow into the ionization channel due to their attraction to the anode (150+ V). The electrons cannot directly migrate to the anode due to Hall effect that is generated from the interaction of the axial electric field and radial magnetic field near the exit of the channel. This interaction produces a force on the electrons in the azimuthal direction that grows as they approach the channel walls due to the increased magnetic field strength [8]. The balance of these forces causes the electrons to circle the channel in a closed drift. Further, the azimuthal velocity ($v_\perp$) of these electrons generates a force $\left(q\left(v_\perp \times \vec{B}\right)\right)$ that causes the electrons to gyrate in the direction of their azimuthal velocity. The radius of this gyration is known as the Larmour radius (r_L) and is found using (2) where m is the mass of the electron and q is the charge of the electron.

$$r_L = \frac{mv_\perp}{q\vec{B}} \quad (2)$$

The depth of the ionization channel is sized such that the Lamour radius for the electrons is substantially smaller than the depth of the channel and the Lamour radius of the ions is substantially larger that the depth of the channel [8]. Sizing with respect to the electron is done to produce a high statistical likelihood of an ionizing collision between the neutrals and the electrons. Sizing with respect to the ions is done to ensure that the magnetic field does not drastically perturb the direction of ions acceleration out of the channel. The electrons will eventually work their way to the anode after collisions with particles and the channel walls where they will be recollected and serve to maintain the anode current.

The propellant is fed into the ionization channel near the anode after passing through a dispersion media [8]. A large percentage of the neutral propellant atoms, xenon being the most common choice due to its high atomic weight and low ionization potential, then interact with the electron cloud described above. The collisions with high energy electrons causes ionization of the propellant, and these ions are accelerated by the electric field to high axial velocities (>10 km/s). The ion plume outside the thruster is then neutralized by electrons being generated by the cathode in order to preserve a quasi-neutral plasma. The theory of operation for a traditional Hall thruster does not completely capture the physics underlying the BHT-20; nonetheless, all of the performance measurements developed from the theory outlined above are still valid for this thruster. The ability to make this assumption is important, because it allows this investigation to build on nearly 50 years of Hall effect research.

Hall effect thruster development began in 1960's in both the United States (US) and the former Soviet Union [9]. The United States then abandoned research involving this thruster for more than two decades after tests in the late 1960's suggested significantly higher values for I_{sp} could be generated by continued development of gridded ion engines. Alternatively, researchers in the Soviet Union elected to continue to research Hall thruster physics and subsequently made improvement in both thrust and efficiency. The Union of Soviet Socialist Republics (USSR) continued this development to the point where one manufacturer, the Experimental Design Bureau/Fakel, has designed and manufactured more than 110 flight Hall thruster [10]. A majority of these thrusters were used for north-south station-keeping (NSSK) missions with one variant of the SPT-100 demonstrating more than 7,000 hours of operation in orbit. The United States eventually become aware of these successes and interest developed in reevaluating the Hall effect thruster.

In the 1990's, following the end of the Cold War, institutions within the United States were able to acquire Hall thrusters from Russia for evaluation [9]. The evaluation was intended to validate performance claims, because the rate of technology transfer through results of previous research studies performed in the former Soviet Union was slowed by the lack of translated manuscripts [11]. Thus, the West needed to commission many studies in order to understand the physics and design of Hall effect thrusters and this blossomed into independently designed US and European thrusters with favorable performance. Recent work conducted by the Air Force Research Laboratory (AFRL) has demonstrated that the latest generation of Hall effect thrusters are capable of performing orbit transfer missions faster and deliver a greater payload than ion engines as a result of

their greater specific power [9]. Subsequently, the use of such thrusters to provide the transfer function for communication satellite (COMSAT) missions has been demonstrated [12]. The ability of the Hall thruster to provide orbit maintenance and momentum dumping after the transfer is an additional benefit. These successes have revitalized interest and investment into the further advancement of this technology.

The realization that Hall thrusters possessed further untapped potential has emboldened the National Aeronautics and Space Administration (NASA) to invest in the development of the High Voltage Hall Accelerator (HIVHAC) with improved I_{sp}, throttle-ability, and endurance in order to provide an alternative for cost-capped deep space science missions [13]. The objective of this endeavor is to build upon the successes of two previous Earth orbiting missions that utilized Hall effect thrusters: the United States National Reconnaissance Office's (NRO) Science Technology Experiments (STEX) spacecraft that was launched in 1998 and the European Space Agency's (ESA) Small Missions for Advanced Research in Technology (SMART-1) Lunar probe that was launched in 2003 [14]. These two spacecraft are illustrated in Figure 7. The ultimate objective is to make Hall thrusters a viable candidate for New Millennium missions where the objective is utilize smaller, lighter, and less expensive systems to accomplish scientific missions [15]. At the other end of the spectrum, interest is also growing to develop small low power Hall effect thrusters.

Tsuyohito Ito and coworkers, from Princeton, suggests there is increasing awareness of the potential to develop a relatively low powered Hall effect thruster (10-100W) in order to provide a viable propulsion alternative for small power-limited satellites [16]. Research at Stanford also substantiates this point [17]. The Russian SPT-

25 Hall effect thruster is one attempt to fill such a void. The SPT-25 possesses the following performance characteristics: power range of 50-150W, total efficiency of 14% at 60W, and a specific impulse of 550s at 60W [18]. In the United States, universities such as Stanford, MIT, and Princeton have experimented with variations on a traditional annular Hall effect thruster design in order to demonstrate thrusters operated at similar power levels [19]. Stanford used the geometric principles governing annular Hall effect thruster operation and scaled them appropriately, so their thruster could operate as low as 20 W [20]. Alternatively, Princeton explored the advantages of using a circular Hall thruster (CHT) design for operation below 100 W [21]. It is plausible that some of their future designs may be able to operate at even lower power levels with some sacrifice to I_{sp} and efficiency. It would be feasible to integrate such a thruster, operating in the 2.5 to 5 W range, onto a standard 3U CubeSat.

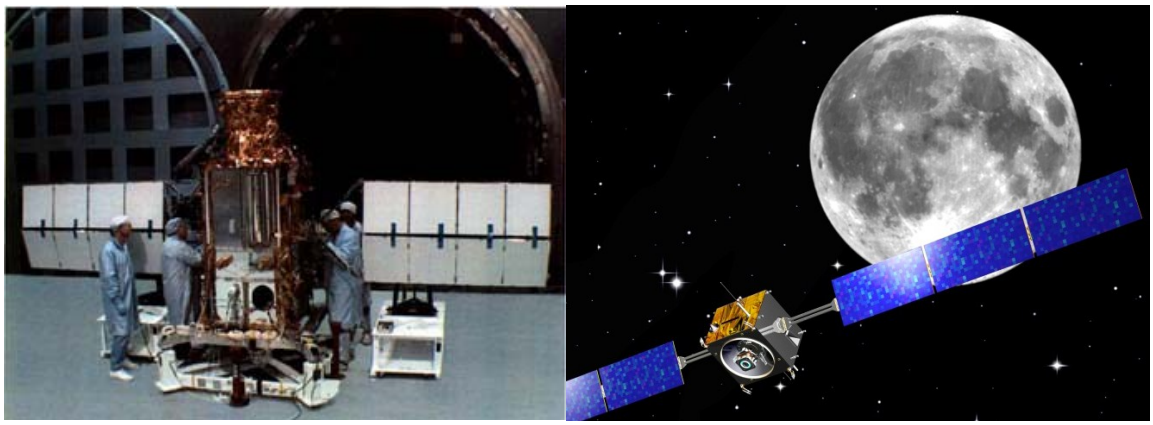

(a) STEX spacecraft, image: NRO [22] (b) SMART-1 spacecraft, image: ESA [23]

Figure 7. NRO STEX spacecraft during assembly and artist rendition of the ESA SMART-1 spacecraft on route to the moon.

Work in electric propulsion is an important enabling technology to expand the usefulness of CubeSats by means of increasing their achievable ΔV, providing additional

options for their attitude control, and supplying an efficient momentum dumping capability [19]. Micro Hall effect thrusters are an important part of the effort to realize these goals, because unlike some well-developed technologies, such as solid fueled rocket motors, an electric propulsion system could simultaneously contribute to all three objectives. The development of such as system would produce a paradigm shift in the constraints surrounding what is currently feasible with these flexible low cost experimental satellites. However, several challenges must be surmounted before the benefits afforded by electric propulsion (EP) are realized for these small satellites.

Among the engineering trades that must be made when optimizing electric thrusters is the amount of thrust that can be generated versus the electric power that can be allocated to the propulsion system [24]. The limited availability of electric power ultimately limits the achievable thrust levels for these devices. This is especially true on small power limited satellites, such as CubeSats. The efficiency of a Hall effect thruster tends to degrade exponentially with decreased size. Efficiencies for thrusters such as the Busik BHT-200 at 200 W is around 42%, whereas the efficiency for SPT-25 identified above was 14%. However, even lower electrical efficiencies may be acceptable for small satellite applications where the non-electric propulsion alternatives include cold gas thruster and butane micro-thrusters with I_{sp} values below 70 s [19].

A consequence of a Hall effect thruster's high I_{sp} and low thrust relative to traditional chemical thrusters is the Hall thruster must operate for significantly longer durations in order to produce the same change in velocity (ΔV). This implies Hall thrusters require a longer timeframe to achieve a given ΔV and must be designed for

longer lifetimes than traditional thrusters. In order to better understand the principle failure mode affecting these thrusters researchers at the University of Michigan have been working to build a hydrodynamic plasma model for simulating sputtering damage [25]. This analysis, as well as, research performed at the NASA Glenn Research Center (GRC) has demonstrated that the erosion profiles, in terms of thruster characteristics, are primarily a function of discharge voltage, magnetic field density, and magnetic field strength [26]. Erosion rate, in terms of propellant characteristics, is primarily a function of ion mass, atomic number, and the ionization ratio [27]. The propellant for the Busik thruster being investigated in this study is fixed; however, it will be important to characterize the thruster parameters and measure erosion as a function of time for the thruster in order to understand how the nontraditional magnetic field lines generated by the permanent magnet influences thruster lifetime. Specifically, it will be interesting to determine if the increased ion current density will significantly shorten this thruster's life as it does with other small thruster designs [28].

A consideration that must be taken into account when designing a spacecraft to include Hall effect thruster propulsion is thoughtful integration to prevent high energy divergent ions from damaging the spacecraft's components, such as solar panels [29]. Divergent particles near the edge of the plume can erode surface finishes such as those on solar panels, reducing power absorption if these parts are within the path of the particles [30]. Surfaces that are treated using electrostatic discharge (ESD) techniques are also susceptible. The size of this plume also has implications for satellite operating procedures. The distribution of charged particles can slightly increase the signal to noise

ratio of communication with ground stations while the thruster is operating. In both cases the obstacles are surmountable with prior planning.

Variants on the Annular Hall Thruster

It is relatively difficult to scale annular Hall thruster designs down to low power due to the need to hold the main dimensionless parameters constant. This implies decreasing the channel size and increasing the magnetic field strength. In-turn, this significantly complicates the design of the magnetic circuit, reduces the volume available to integrate heat shields and erosion resistant insulation, and can lead to significant heat loading and erosion of channel surfaces [31]. The one notable successful attempt to scale an annular Hall effect thruster to operate at less than 50 W was done by Stanford University [32]. This design included diamond lined channel walls in order to provide improved temperature and sputtering erosion resistance. Previous research performed at Stanford on an inherently less efficient linear geometry Hall thruster had demonstrated that diamond walls provided a 25% decrease in the sputtering erosion rate when compared with traditional boron nitride walls [33]. The one negative attribute associated with using diamond was the extremely high thermal conductivity. This is one of the reasons the Stanford annular design had to include significant water cooling of the thruster magnets in order to avoid the demagnetization that would have resulted from the uncooled operating temperature. These challenges led researchers at the Princeton Plasma Physics Laboratory to pursue development of a low power circular Hall thruster.

A cylindrical Hall thruster has a single central magnet that is generally flush or nearly flush with the anode, which decreases the insulator surface area to discharge

channel volume and simplifies construction for low power applications [34]. Similar to annular Hall thrusters, CHTs may use either permanent or electromagnets to generate quasi-orthogonal magnetic field lines between the central circuit and outer discharge channel wall. The axial component of magnetic field lines is significantly more pronounced than for annular designs, but the general physics underlying CHT operation does not appreciably change [35]. The BHT-20 can be seen as a further evolution of the CHT design where the central magnetic circuit is removed to ease packaging as the thruster is scaled to very low power levels.

The fundamental electromagnetic difference between the BHT-20 and a traditional CHT is the magnetic field lines for the BHT-20 are nearly axial in orientation. The lack of a significant radial component to the magnetic field lines implies that no significant Hall effect will be produced by electrons following the primarily axial electric field lines to the anode. It is supposed that this will reduce the electron dwell time in the discharge channel and possibly reduce the beam current efficiency as a result.

Diagnostic Techniques

Diagnostic instruments identified for this research include two different thrust stand designs and a Faraday probe. These diagnostic tools are well established within the field of electric propulsion and have been used extensively at AFIT to characterize both established and new thruster designs. The use of well vetted instruments was deemed important due to the lack of previous knowledge regarding the operation of this novel micro thruster design. The Faraday probe was the first instrument used, because the laboratory was already configured for this apparatus.

At its core, the Faraday probe consists of a metal collector plate that measures ion current at various points in the plasma plume. The accelerated ions in the plume strike a collector plate and this induces a flow of electrons, which is the current that the probe measures. In order to reduce one major source of error, the Faraday probe used in this experiment includes a guard that can be biased negative in order repel the electrons in the plume, and the ring reduces distortion of the sheath by the probe. These electrons would artificially reduce the measured current if they were to strike the collector plate. The measured current and the guard port area can be used to ascertain the current density at a point in the plasma plume. A map of the current density in a plane can be created once a series of measurements are taken at a constant radius from the centerline of the thruster discharge channel. The result provides insight into plume symmetry, divergence angle, and with numeric integration, the beam current. All of these performance measures help to reveal how the thruster functions and how well it functions, but a measurement of thrust is still necessary in order to identify the fundamental performance parameters for a thruster.

The most important performance measurement that is used to characterize a new propulsion device is thrust. In this experiment, an attempt was made to measure thrust with two different instruments. The average propellant velocity ($\bar{v}$) and I_{sp} can be directly derived using the measured value for thrust (T) and the mass flow rate of the propellant ($\dot{m}$) [36].

$$\bar{v} = \frac{T}{\dot{m}} \tag{3}$$

$$I_{sp} = \frac{T}{\dot{m}g} \tag{4}$$

The thrust efficiency can also be determined using T once the total system power P is measured.

$$\eta_T = \frac{2P}{\dot{m}g} \tag{5}$$

The first instrument that was used to measure the thrust output of the BHT-20 was a traditional inverted pendulum thrust stand. This stand design is commonly used to characterize low thrust (mN) electric propulsion devices, such as Hall effect thrusters. These instruments can generally be tuned to accommodate a wide variety of thruster weights and outputs through the appropriate selection of eight flexures and a primary spring. The accuracy of this stand is highly dependent on the validity of an assumption that all measurements are taken at a constant temperature. The use of active water cooling and frequent calibrations is the most common way to reduce this potential source of uncertainty [37].

The second instrument that was used to measure the thrust output of the BHT-20 was a torsional thrust balance built by Busek, which is capable of resolving continuous thrust levels of approximately 1μN [38]. This design requires the thruster to be mounted on one side of a balance arm with an appropriate counterweight on the opposite side in order to balance the arm and minimize any torques generated by the weight of the thruster. Motion of the balance arm is resisted by a calibrated torsional spring, and the displacement is measured using a laser displacement system (LDS). Within the operating range of the torsional balance, the LDS is capable of producing a nearly linear voltage

response curve with respect to displacement. A schematic of the torsional thruster stand and the associated support equipment is illustrated in Figure 8.

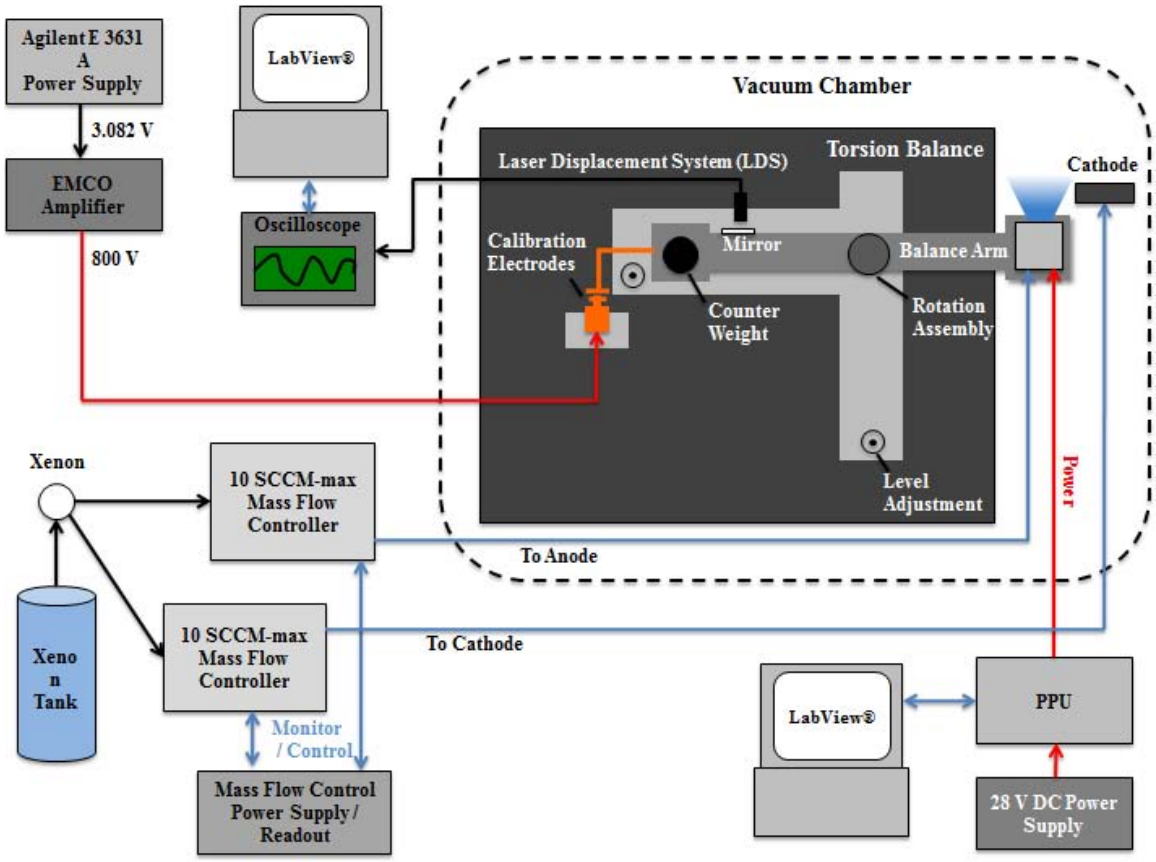

Figure 8. Schematic of torsion thrust balance for measuring μN thrust levels.

The torsional balance provides a precise technique to measure thrust, but the accuracy of the derived thrust values are highly sensitive to the accuracy of the calibration voltage that is generated during setup. The voltage reading will drift over time if the system does not operate at a constant temperature. This necessitates checking the system zero before and after each measurement in order to determine if any drift occurred. If drift was present then a linear approximation of the drift rate provides a simplified method to account for the influence on the reported voltage values with respect

to time. Thrust measurements at constant power simplify the analysis by avoiding difficulties arising from resolving transient loads with this instrument.

Experimental Considerations

AFIT currently possesses a 3.175 mm Busek BHC-1500 hollow cathode with enclosed keeper. While testing at Busek has demonstrated that this cathode will work with the thruster under investigation, the packaging, propellant utilization efficiency, and thrust vectoring that result are not desirable. One alternative would be to acquire a micro-hollow cathode of similar design, but with flow channel diameter of 1.5875 mm or smaller. The cost associated with this option is prohibitively expensive and the timeline associated with development of such a device is currently unknown. The other alternative appears more feasible at this point in time.

The hollow cathode could be replaced by a large lanthanum hexaboride single crystal emitter relying on ohmic heating to generate electrons. Lanthanum hexaboride (LaB_6) Cathodes offer the capability of long life relative to alternative electron emitters and are more than two orders of magnitude less sensitive to impurities present in the propellant than traditional alternatives [39]. The longevity of LaB_6 has been confirmed by tests including operation for over 300 h while being exposed to air more than 100 times without measureable degradation in emission [40]. Figure 9 offers a view of multiple LaB_6 emitters. The emitter pictured in the lower left-hand corner of the image is suitable for use with low current space propulsion devices due to the relatively large surface area of the crystal that can be ablated to produce electrons.

Figure 9. Depiction of multiple Lanthanum Hexaboride crystal emitter designs, used with permission of Applied Physics Technologies.

Efficiency Determinations

The total efficiency of a Hall effect thruster was previously described using the jet power relationship. The total efficiency can also be expressed as the decomposition of the component efficiencies, as shown in (6) from Goebel and Katz [8].

$$\eta_T = \gamma^2 \eta_b \eta_v \eta_m \eta_o \tag{6}$$

The correction factor (γ) is used to describe the effects of beam divergence and multiply charged ion content and is given by

$$\gamma = \alpha F_t. \tag{7}$$

The thrust correction factor (α) is used to account for the presence of doubly ionized atoms. Letting I^+ represent the number of singly ionized atoms and I^{++} represent the number of doubly ionized atoms produces the following expression for α,

$$\alpha = \frac{1+\frac{I^{++}}{\sqrt{2}I^+}}{1+\frac{I^{++}}{I^+}}. \tag{8}$$

Thus, the ratio of singly to doubly ionized atoms can be found directly using laser absorption. The geometric efficiency (F_t) represents the thrust loss from beam divergence and is found using the half-angle divergence of θ and the ion current density $(J(r))$, as shown in (9).

$$F_t = \frac{\int_0^r 2\pi J(r)\cos\theta(r)dr}{I_b} \tag{9}$$

The $J(r)$ distribution can be found experimentally using a Faraday probe at varying values of r. The beam current efficiency (η_b) is found from the ratio of the beam current to the discharge current.

$$\eta_b = \frac{I_b}{I_d} \tag{10}$$

The voltage ratio (η_v) is found from the ratio of the beam voltage to the discharge voltage.

$$\eta_v = \frac{V_b}{V_d} \tag{11}$$

The mass utilization efficiency (η_m) is found from the ratio of the mass flow of ions out of the thruster $(\dot{m}_i)$ to the sum of the mass flow rates from the anode $(\dot{m}_a)$ and cathode $(\dot{m}_c)$.

$$\eta_m = \frac{\dot{m}_i}{\dot{m}_a + \dot{m}_c} \tag{12}$$

The electrical utilization efficiency (η_o) is found from the ratio of the discharge power of the thruster (P_d) to the sum of P_d, the keeper power (P_k), and magnet power (P_{mag}).

$$\eta_o = \frac{P_d}{P_d + P_k + P_{mag}} \tag{13}$$

The total efficiency of this μ-Hall thruster will be found with the jet power relationship. The other isolated efficiencies above will be reported based on available information from testing in order to better characterize this thruster.

III. Methodology

This chapter details the methodology and experimental setup used to generate data for this new thruster design. Details regarding the laboratory equipment and facility used to conduct this research are provided. The procedures used to setup and conduct each experiment are delineated. The methods used to reduce the data from each experiment and the methods used to quantify the experimental error are described.

Vacuum Facility and Support Equipment

The experimental work detailed within this paper took place within the AFIT Space Propulsion Analysis and System Simulation (SPASS) Laboratory. This facility contained the largest and most versatile vacuum chamber at AFIT. The experimental setup centered around this 2.5 meter long by 1.8 meter vacuum chamber that was capable of achieving vacuum levels on the order of 10^{-7} torr. The chamber was produced and installed by PHPK Technologies. It featured multiple feed through and view ports that made it an ideal facility for supporting the instrumentation used to conduct this test, as illustrated in Figure 10. In order to expedite decreasing the tank pressure from atmospheric to 10^{-7} torr a staged system was utilized.

The first phase of the pump down sequence relied on a mechanical ruffing pump, a Leybold Trivac D65B, to reduce pressure within the chamber from atmospheric to its crossover pressure (100 millitorr) at which point it would deactivate. Upon initiation of the pump down sequence, a helium cooled CVI Torr Maser TM250 began cooling. This cryogenic pump was mounted atop the chamber, but separated from the tank with a gate valve that would not open until the crossover pressure was achieved. The TM250 then

began reducing the pressure within the chamber farther while four helium cooled CVI Torrmaster TM500 cryo-pumps began cooling. Upon reaching their operating temperature, which ranged from 15 to 20 Kelvin, the combined pumping capacity of these four pumps was 16,000 liters per second of xenon gas [38]. This translated to a typical operating pressure of approximately 10^{-6} torr while conducting experiments with the BHT-20. Accurate measurement of the pressure during operation was essential to ensure inadvertent cathode poisoning did not occur and to be able to record the pressure when experiments were being conducted.

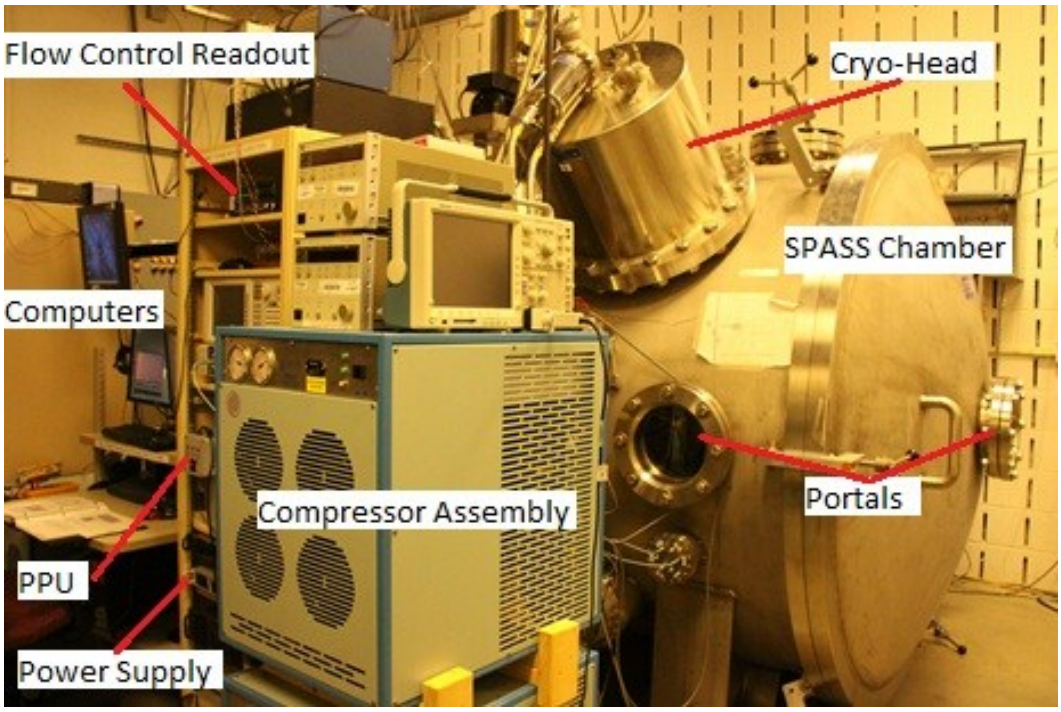

Figure 10. AFIT SPASS laboratory chamber and support equipment.

Two devices were used to monitor pressure and measure the gas species present in the vacuum chamber during testing. A Lesker 300 Series Convection vacuum gauge was used to measure pressures in excess of 0.1 millitorr, which was insightful during roughing pump operation. An Extorr XT100 Residual Gas Analyzer (RGA) was used to

measure pressures from 10^{-5} to 10^{-8} torr. This unit integrated three separate gauges, so it was capable of measuring pressures ranging from atmospheric to 10^{-11} torr. Extorr's VacuumPlus software was used during testing to provide both a continuous pressure reading and a plot of the partial pressure for the gas species present in the vacuum chamber, as shown in Figure 11. Special care was taken to ensure H_2O and O_2 levels were below 10^{-6} before cathode conditioning commenced to avoid unnecessary damage. The automation built into this system helped to decrease the opportunity for human error, increased test reproducibility, and expedited the pumping sequence.

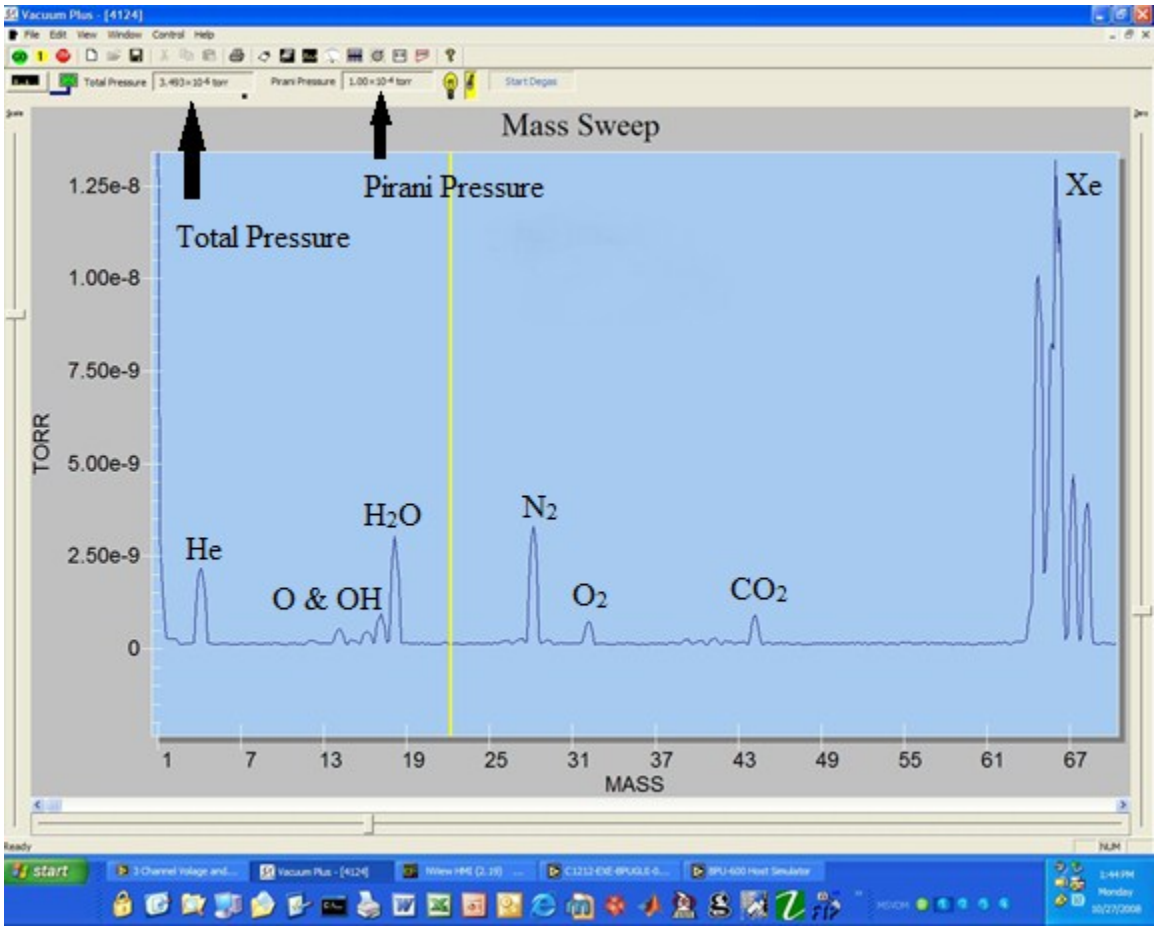

Figure 11. Screenshot of the Extorr VacuumPlus software interface with identification of significant gaseous species components.

The vacuum chamber was regularly pumped up to atmospheric pressure after the completion of a test in order to check the condition of the thruster's boron nitride insulator and permanent magnet. The procedure was not initiated until the cathode had ceased operation for at least one hour in order to ensure that the emitter was not hot during the pump-up sequence. To initiate the sequence a single stop button was depressed that caused the five cryo-pumps to cease operation. The chamber was filled with dry nitrogen once the CVI CBST 6.0 scroll compressors ceased cooling the pumps and the gate valve for the TM250 closed. The dry nitrogen was supplied via a compressor and battery of nitrogen generators. Once the chamber was at atmospheric pressure the battery of instruments and tools within the chamber were easily accessible for establishing new experimental setups.

To facilitate the precise placement of the cathode relative to the thruster and other instruments within the chamber, such as the Faraday probe, the cathode was mounted on a fixture constructed of 80/20™ aluminum components that were generally bolted to the vertical Z-axis of a three-axis Aerotech® translation system. The thruster was oriented pointing down the length of the chamber and it was fixed in this orientation, because the translation system could only move in the three primary axes which were oriented such that the X-axis was parallel to the length of the chamber. Each axis of the translation stage possessed a 60 cm range of motion with sub-millimeter accuracy on the movement of each axis. The flexibility afforded by this system made it possible to quickly transition the cathode from one position to another relative to the thruster without opening the chamber, as depicted in Figure 12. Because the thruster position was fixed, the Faraday probe also had to be mounted to a translation system, as illustrated by Figure 13.

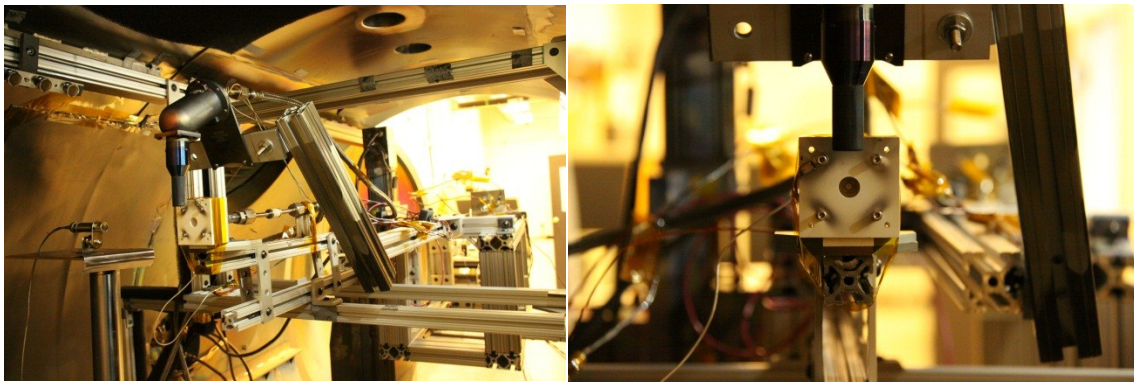

a) Side view of cathode translation mount b) Front view of cathode translation mount

Figure 12. Cathode mounted to translation stage for movement relative to thuster.

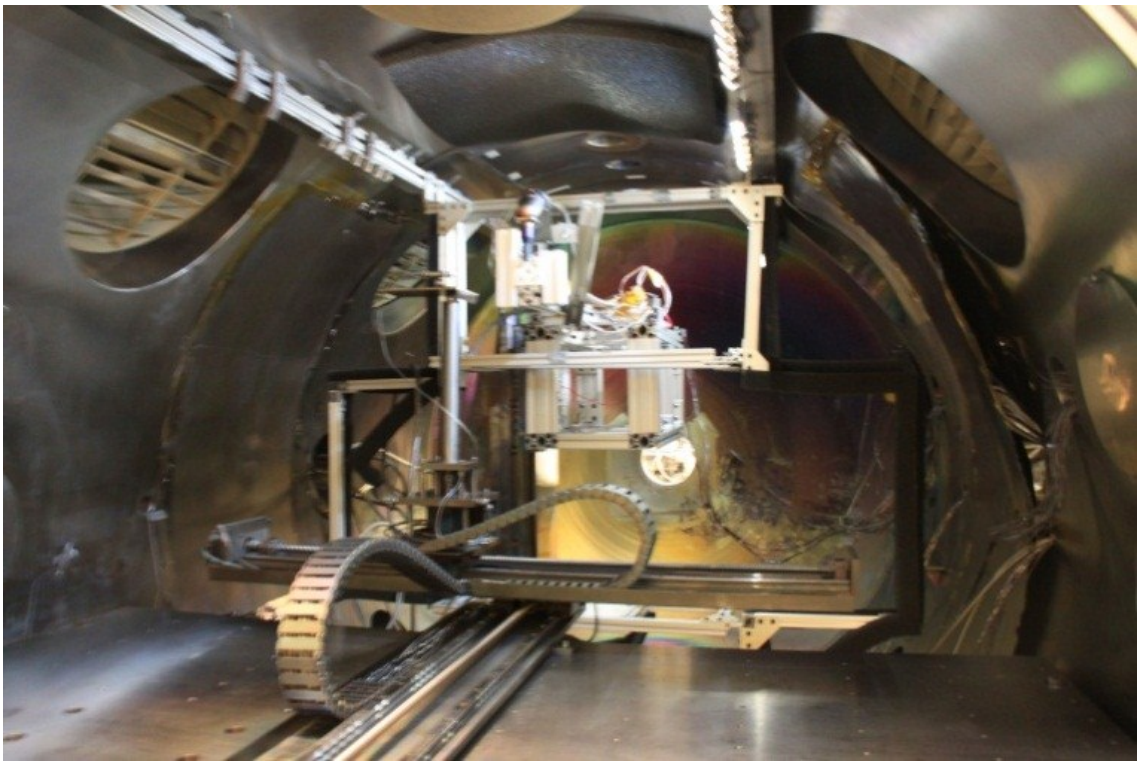

Figure 13. Faraday probe translation stage depicted in foreground.

The Faraday probe was mounted on a three axis translation and rotation system, which was designed by Colorado State University. The system included a radial stage (R), an axial stage (Z), and a rotational stage (θ). The R and Z stage both possessed a 1.0

meter range of motion and the θ stage possessed a 180° range of motion. The three stepper motors in this system were water cooled by a Thermo Scientific NESLAB RTE7 chiller external to the vacuum chamber. The stages and Faraday probe were all controlled by a single integrated LabView® VI developed by Colorado State University for this purpose.

BHT-20 Control System

The BHT-20 thruster was operated over a range of voltages and discharge currents that were found to be stable during the generation of voltage-current curves. The thruster was paired with an external BHC-1500 cathode that was operated at the manufacturer's suggested parameters. An individual xenon propellant feed line was used for both the thruster and cathode during operation, and both devices were controlled using a Busek Power Processing Unit (PPU). The operating procedures established by the author for the BHT-20 are included in Appendix A.

The SPASS laboratory was plumbed to provide either xenon or krypton for use in electric thrusters. The xenon gas used in this experiment was stored in a pressurized tank with a regulator that was used to reduce the line pressure from approximately 600 psi to 20 psi. The xenon propellant, flowing at 20 psi, was then routed to four MKS model 180A precision mass flow controllers, as shown in Figure 14. Two of these mass flow controllers had a full range of 50 sccm and two had a range of 10 sccm. All of the controllers have an accuracy of 0.01% of their full flow value [41]. Both the cathode and thruster used a 10 sccm controller. Xenon flow was routed from these controllers to the

thruster and cathode with a combination of stainless steel and PTFE lines. Flow rates were controlled and monitored using an MKS Type 247 four-channel readout.

Figure 14. Xenon and krypton bottle and battery of four mass flow controllers.

Power for the thruster and cathode were provided by a Busek BPU-600 Power Processing Unit (PPU), which reported discharge voltage with an accuracy of 0.1% [42]. The PPU received its power from a Sorensen DCS55-55 power supply, which was capable of 0-55 V and 0-55 A. Control of the PPU was achieved using Busek's BPU-600 Host Simulator, which was a LabView® software interface and is shown in Figure 15. This program provided both the capability to control the functions associated with the thruster and cathode, as well as, monitor their performance.

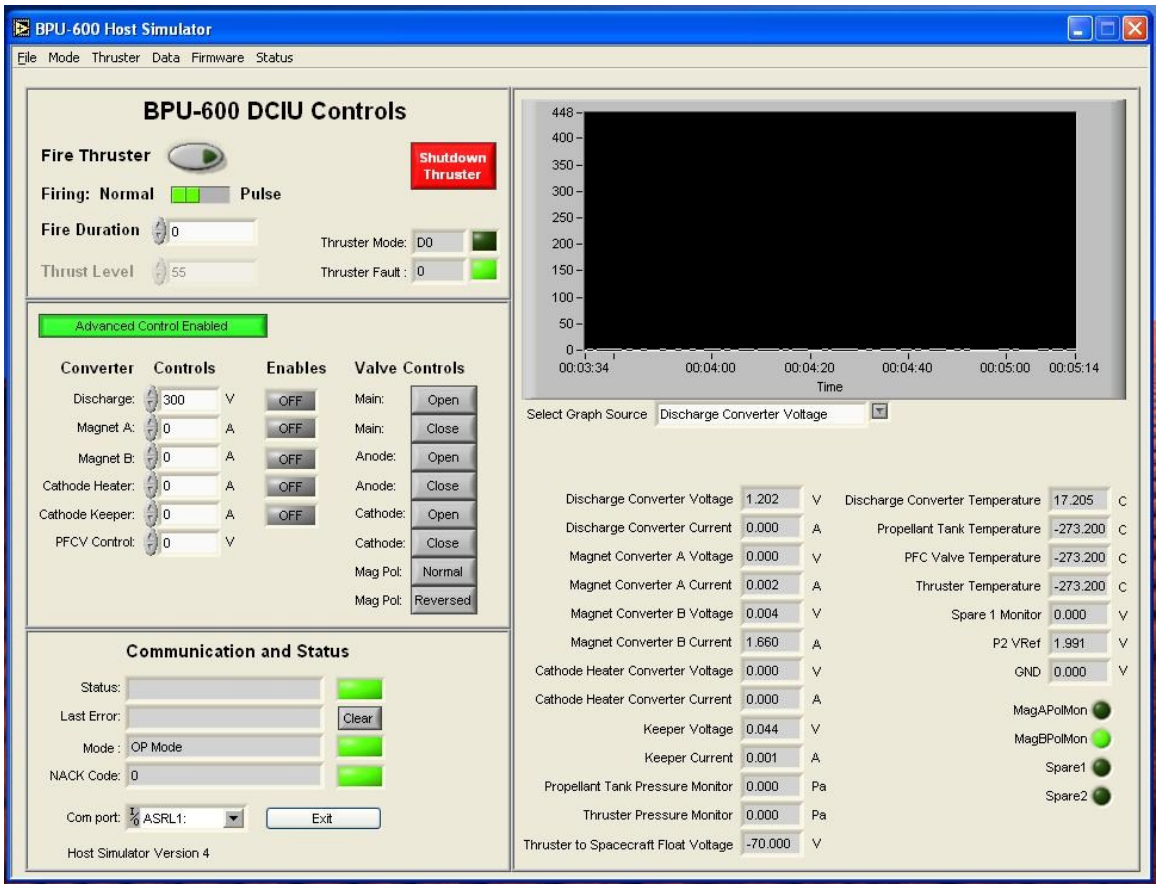

Figure 15. BPU-600 Host Simulator software interface.

Voltage-Current Measurement

In order to generate voltage-current (V-I) curves, the voltage and current for the thruster and cathode had to be measured and recorded. The anode voltage was commanded and monitored using Busek's BPU Host Simulator Software. Shunt resistors connected in series were used in conjunction with Ohm's Law to measure current for the anode and cathode keeper. A National Instruments SCXI-1321 4-channel readout was used to measure the voltage drops across the resistors, and these voltages were used to generate current values within the LabView® program for controlling the PPU. A special 80/20™ mounting structure for the thruster and cathode was produced that

enabled the thruster to face one portal while it was orthogonal to two others, which enable high resolution photography of the plasma plume during operation, as shown in Figure 16.

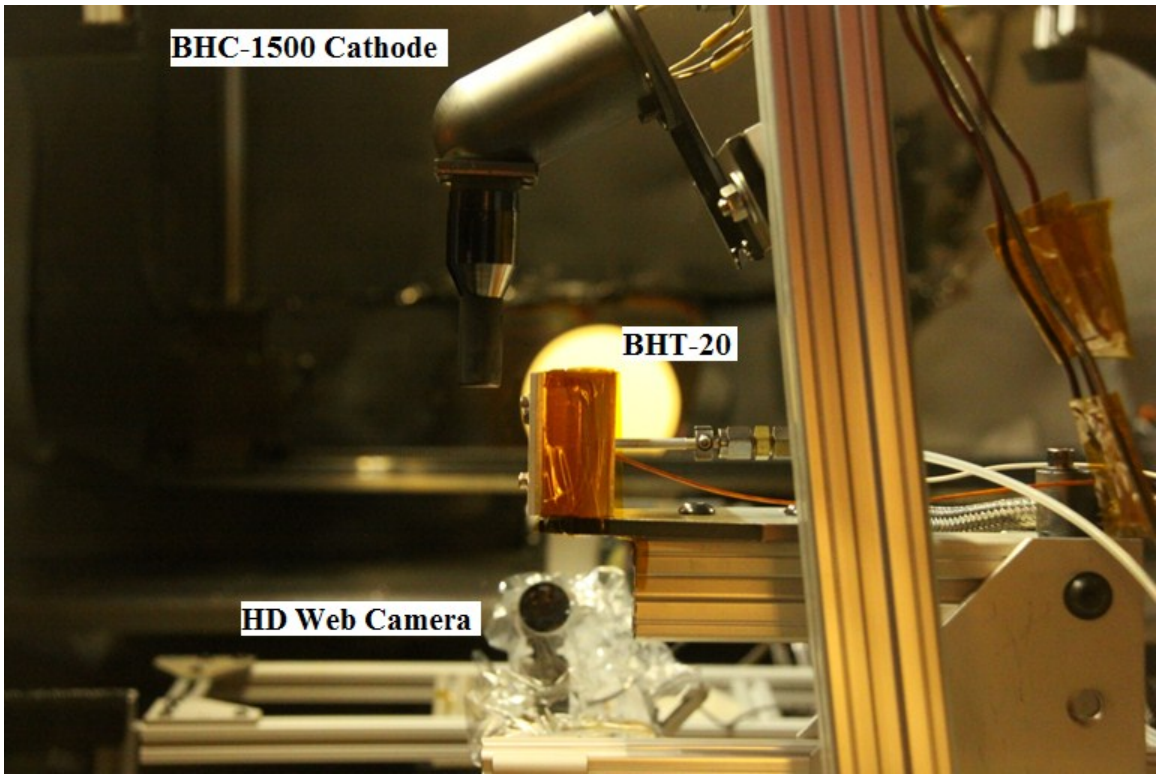

Figure 16. Voltage-current measurement test setup.

With the necessary infrastructure in place, V-I curves were then produced by setting the anode flow rate to a constant value and adjusting the discharge voltage between 140 and 250 V. At each voltage the associated discharge current was noted and tabulated. This procedure was repeated for five different flow rates. In specific cases where the discharge current did not settle to a single stable value, six different values would be recorded in order to capture the range of currents displayed.

Faraday Probe

The Faraday probe was used in this analysis to measure the current density in the plasma plume generated by the thruster. The probe was a straightforward device which consisted of a collector disk that had a potential applied to it and a resistor that was used to measure the drop in voltage (V) across it. The collector plate was biased positive in order to repel low energy charge-exchange ions existing in the plume that should not be included in the measured discharge voltage. The Faraday probe used in this experiment was a guarded design that included an enclosure surrounding the collector plate that was biased negative in order to repel electrons and an aperture with a diameter of 0.762 mm, in this case, to allow ions to enter and strike the collector disk, which is illustrated in Figure 17. Thus, the following formula was used to determine the current density (j_B) [43].

$$j_B = \frac{V \cdot 1000}{R \cdot A_{apeture}} \left(\frac{mA}{cm^2}\right) \tag{14}$$

Where R is the value of the resistor being used, 4.66 MOhm in this case, and $A_{apeture}$ is the area of the probe guard aperture. The collector plate was biased to +30 V using a Kiethley 6517A electrometer/high resistance meter and the probe body was biased to -30 V using an Agilent 6018A power supply. The voltage drop across the probe's resistor was measured using an Agilent 34970A data acquisition unit accurate to ±0.02% and transmitted to a LabView® VI designed to record the data to a tab delineated file.

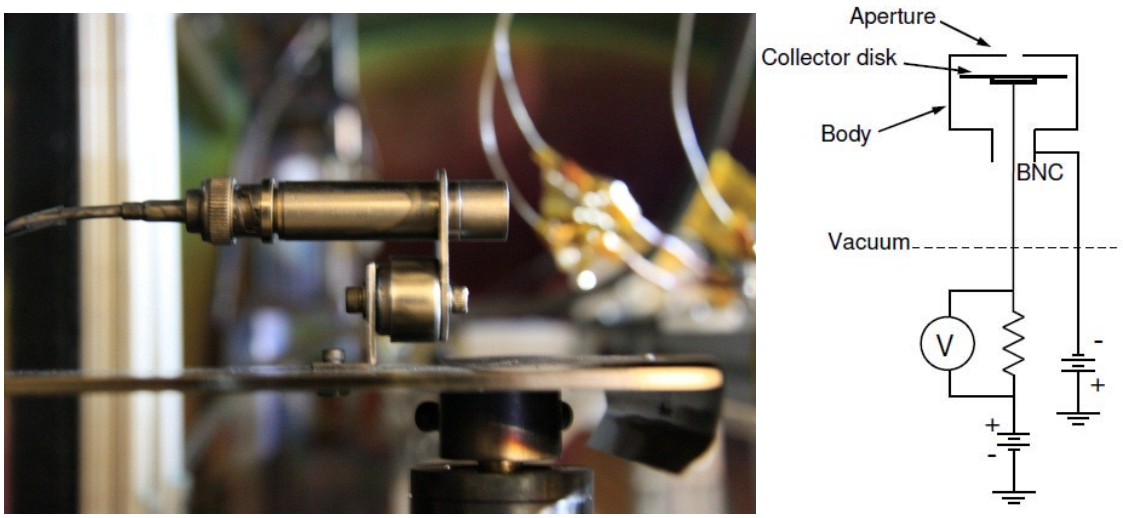

a) Picture of guarded Faraday probe used in this test. b) Schematic, from Rotter [42].

Figure 17. Faraday probe depiction and schematic.

Special care was taken to achieve accurate alignment of the thruster with the Faraday probe. The method used was to first center the Faraday probe along the R stage, then to move the probe all the way forward with respect to the Z stage, and finally to set the θ stage to 0, which oriented the thruster along the length of the chamber. A DeWalt™ laser level was then mounted to a Manfrotto™ tripod and oriented such that the laser dot was centered on the back of the Faraday probe. The Faraday probe was then moved to the far corner and the thruster moved along the Aerotech's® Y- and Z-axes until the laser dot was centered in the thruster channel. Finally, the laser level was removed and the distance between the Faraday probe aperture and thruster face precisely measured with calipers, so the thruster could be moved forward to a position of Z = 0 with respect to the Faraday probe stages. The first three steps in this process are detailed below in Figure 18.

a) Laser level positioned.

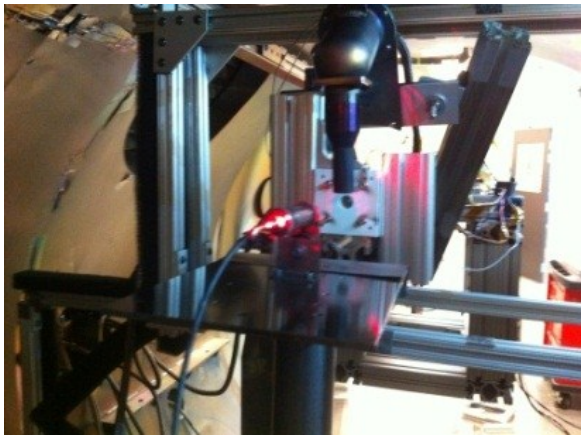

b) Laser centered.

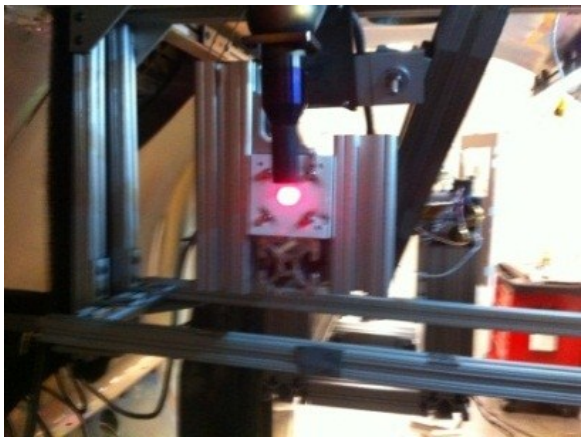

c) Thruster alignment.

Figure 18. Thruster alignment for Faraday probe data collection.

The Faraday probe was attached to a translation system that enabled the Faraday probe to traverse a semicircle around the thruster about the plane bisecting the thruster along its vertical axis. Measurements were taken every 1° along constant radii of 13 and 15 cm, as illustrated in Figure 19. The software automatically calculated the θ value necessary to keep the Faraday aperture pointed at the center of the thruster channel exit, which was also the center of rotation. The software interface for controlling the Faraday probe and collecting the associated data is captured in Figure 20.

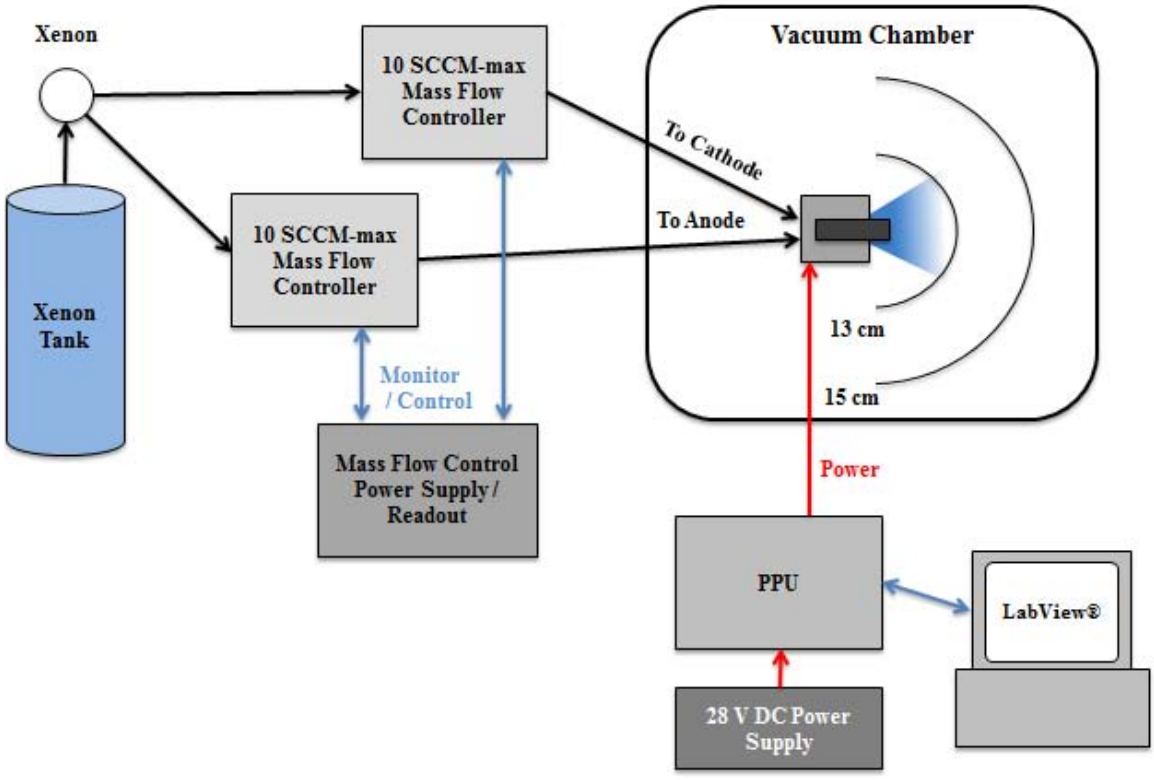

Figure 19. Schematic of Faraday probe experimental setup with illustration of 13 and 15 cm sweep radii.

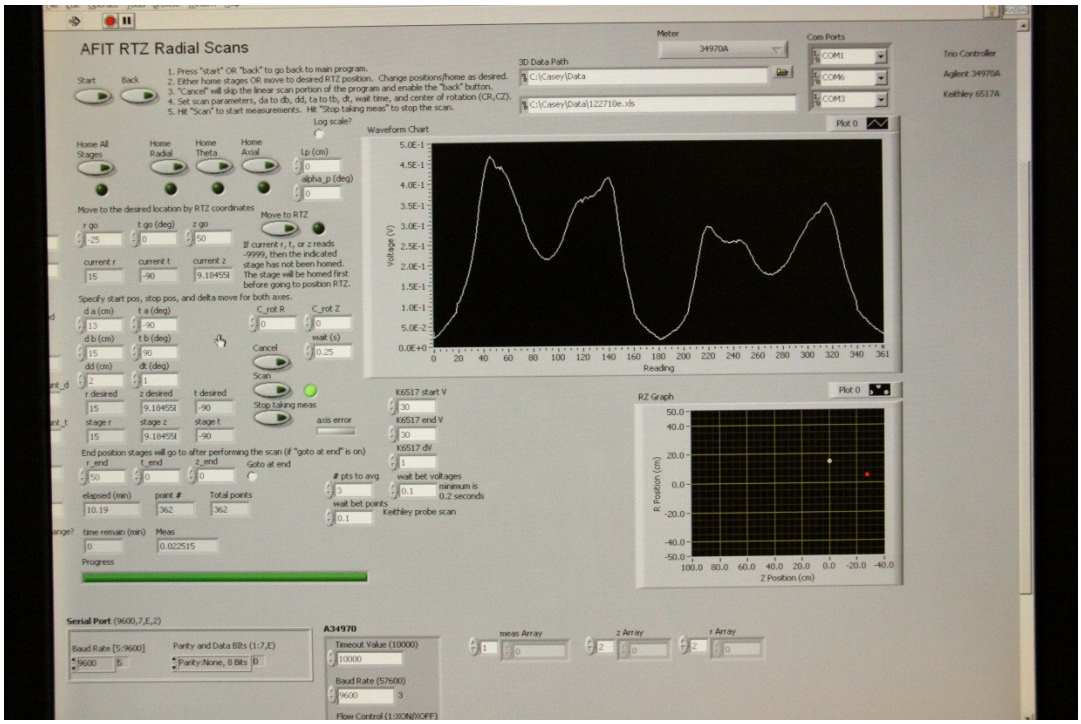

Figure 20. Faraday probe control and collection LabView interface.

Manipulation of the Faraday data yielded a current density value at each point of measurement, which could then be integrated numerically to yield an estimate for the total current through a theoretical half-sphere shell of a given sweep radius. The assumption was made that half of the hemisphere would be characterized by the sweep values left of the thruster centerline and half of the hemisphere would be characterized by the sweep values right of the thruster centerline. Thus, the total beam current was given by

$$I_b = \iint_{S_0}^{S_f} j_b dS \ (A) \tag{15}$$

Additionally, the authors found it necessary to characterize the effective asymmetric bias of the beam current, which for the purpose of this work was denoted as (F_a). This new term was used to capture the portion of the divergent beam current that

would not cancel based on a comparison of the integration of the left half-hemisphere and right half-hemisphere, respectively, as shown in (16).

$$F_a = \frac{\left(\iint_{LHH_0}^{LHH_f} j_b \sin(\theta) dS - \iint_{RHH_0}^{RHH_f} j_b \sin(\theta) dS\right)}{I_b} \tag{16}$$

Faraday probe error was computed by conducting five consecutive repeat runs at identical test radii, typically 13 and 15 cm. An average beam current for each run, at each test radius, was then calculated. The standard deviation, σ, was then computed for the averages at each radii. A conservative estimate for the measurement error associated with the Faraday probe was produced by computing the standard error, as illustrated in (17).

$$SE = t\frac{\sigma}{\sqrt{n}} \tag{17}$$

A t value of 1.96 was used in order to produce a confidence factor of 95%. In all cases, the value for n was 5.

Generally, alignment error would be determined using quantification of the full width half max value (FWHM) and a comparison made between where this current density value was achieved on one side of the plume versus the other. In this case, the extreme asymmetry present in plumes made this technique unreliable. Extreme care was taken in each case to achieve consistent and accurate alignment of the thruster using the laser level technique described above. Based on previous attempts to use this method with other thrusters, it is estimated that the shift was not more than two degrees in any

case. This level of misalignment is well within the angular tolerance of the Faraday probe [44].

Inverted Pendulum Stand

AFIT's inverted pendulum stand was purpose built by Busek for electric propulsion thrust measurement. The core of this instrument was a linear variable differential transformer (LVDT) that was used to measure the linear motion of the thruster support stand in response to an applied force. It was discovered that the initial resting position of the thrust stand placed the LVDT well outside of its linear response range, so the LVDT collar had to be manually adjusted in order to get the LVDT within a range where the fine adjustment screw could be used to zero the instrument. This task required disassembly of the thrust stand and repositioning of the collar, which was secured by a set screw. The new position for the LVDT caused some concern, because it necessitated that the LVDT collar was almost completely protruding from its mounting bracket, as illustrated in Figure 21. However, no apparent issues arose as a result of this placement. After the collar was relocated, the fine adjustment screw was used to ensure the instrument was centered within its linear range between each test.

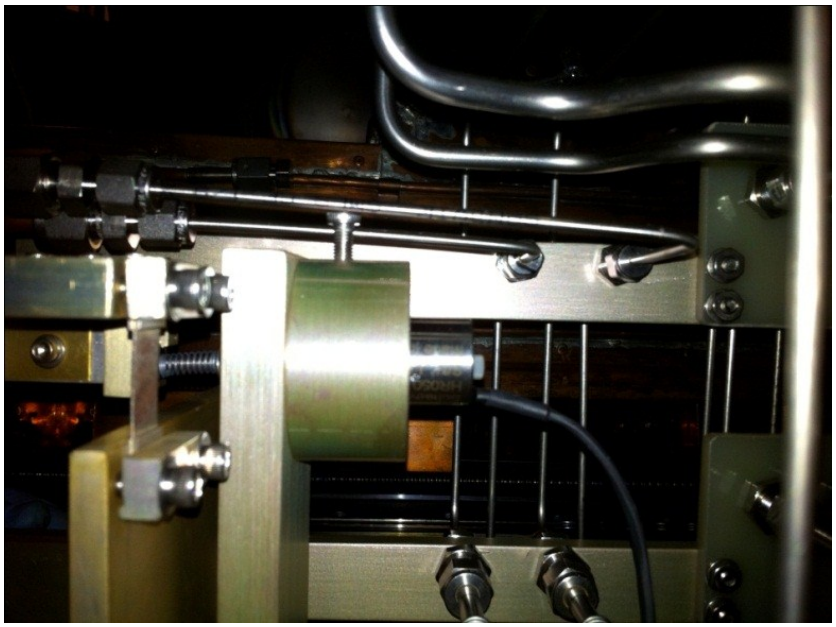

Figure 21. LVDT collar protruding from circular mounting bracket.

The output from the LVDT was transferred via a bundled cable and cannon plug chamber pass through to a readout unit developed by Busek, which is shown in Figure 22. The unit included a Schaevitz MP2000 LVDT readout controller that was used in multimeter mode [45]. The amplified analog voltage output from the MP2000 was recorded by the 'Thrust Stand' LabView software interface. The stand also included a passive eddy-current damper that was used when mounting the thruster in order to reduce large oscillations. The damper did not quell the small random vibrations that were transmitted through the chamber, so it was not engaged during calibration runs or thrust measurement. Another element on the thrust stand control unit was an inclinometer readout that provided information from the inclinometer mounted to the thrust stand's lower platen. The inclinometer was used to provide a feedback circuit when adjusting the stand level with a stepper motor, and the inclination was noted during all tests. A

previous effort using this thrust stand revealed that changes in the stand level produced a highly correlated bias that could be corrected if this data was noted during testing. The LVDT would often drift slightly during testing, but an attempt was made to minimize this drift through the use of active water cooling.

Figure 22. Thrust stand readout unit.

As discussed in chapter 2, the repeatability of the data produced by the thrust stand was highly dependent on an assumption of constant temperature. The stand included the liberal use of water cooling lines on an external thermal jacket and surrounding thruster pedestal, as illustrated in Figures 23 and 24. The external water jacket was designed to eliminate radiative heat transfer from the thruster plume and other thermal sources in the chamber. The lines surrounding the thruster pedestal were meant to eliminate any conductive heat transfer that might pass from the thruster body to the mounting plate. Cooling water was supplied from a NESLAB RTE7 water chiller outside the chamber, which provided a temperature stability of ±0.01 degrees Celsius [46].

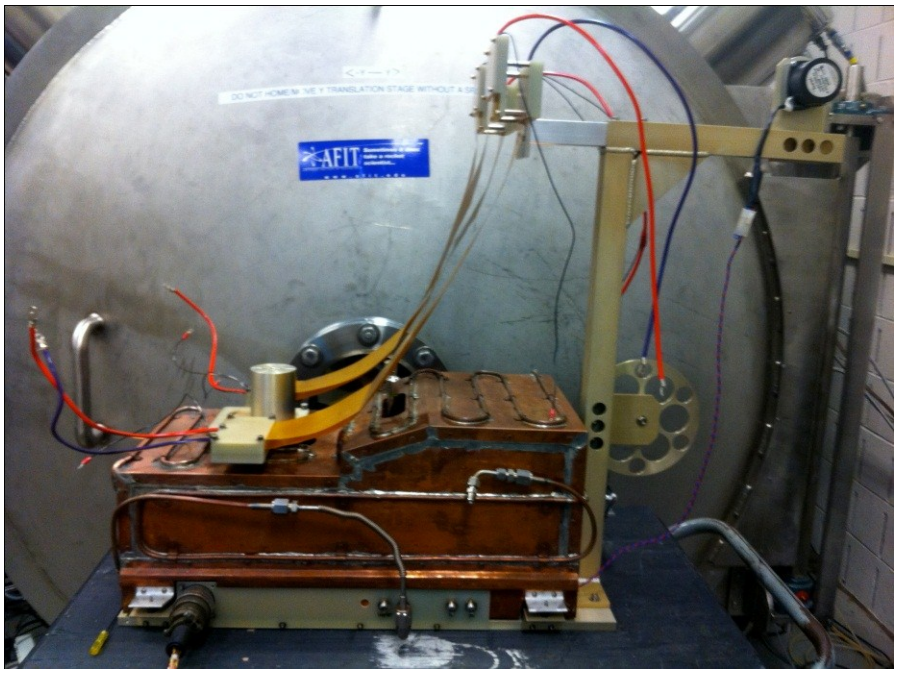

Figure 23. Thrust stand with water jacket and wiring harness in place.

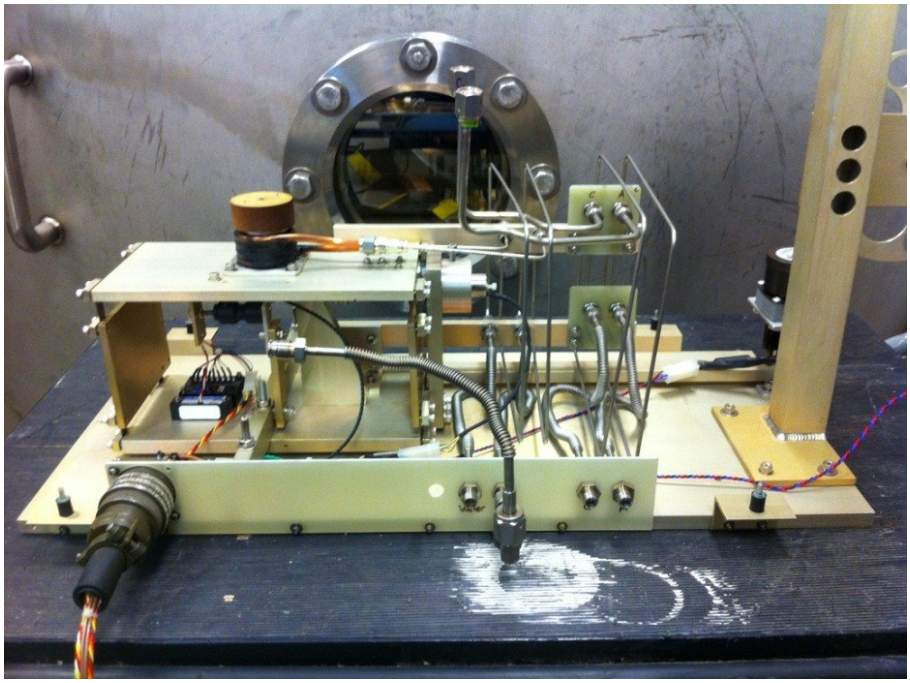

Figure 24. Thrust stand internal workings.

The thrust stand was installed in the vacuum chamber on a large steel platen in order to provide a stable base for performing thrust measurements, as illustrated in Figure 25. The cathode was mounted on an external sting in order to reduce the complexity of thruster integration. After some experimentation with the collection of calibration curves it was discovered that adding additional weight to the thrust stand platen helped to reduce the magnitude of the oscillations resulting from random noise transferred through the chamber to the thrust stand. For testing, two 0.5 kg weights were included with the thruster on the mounting pedestal.

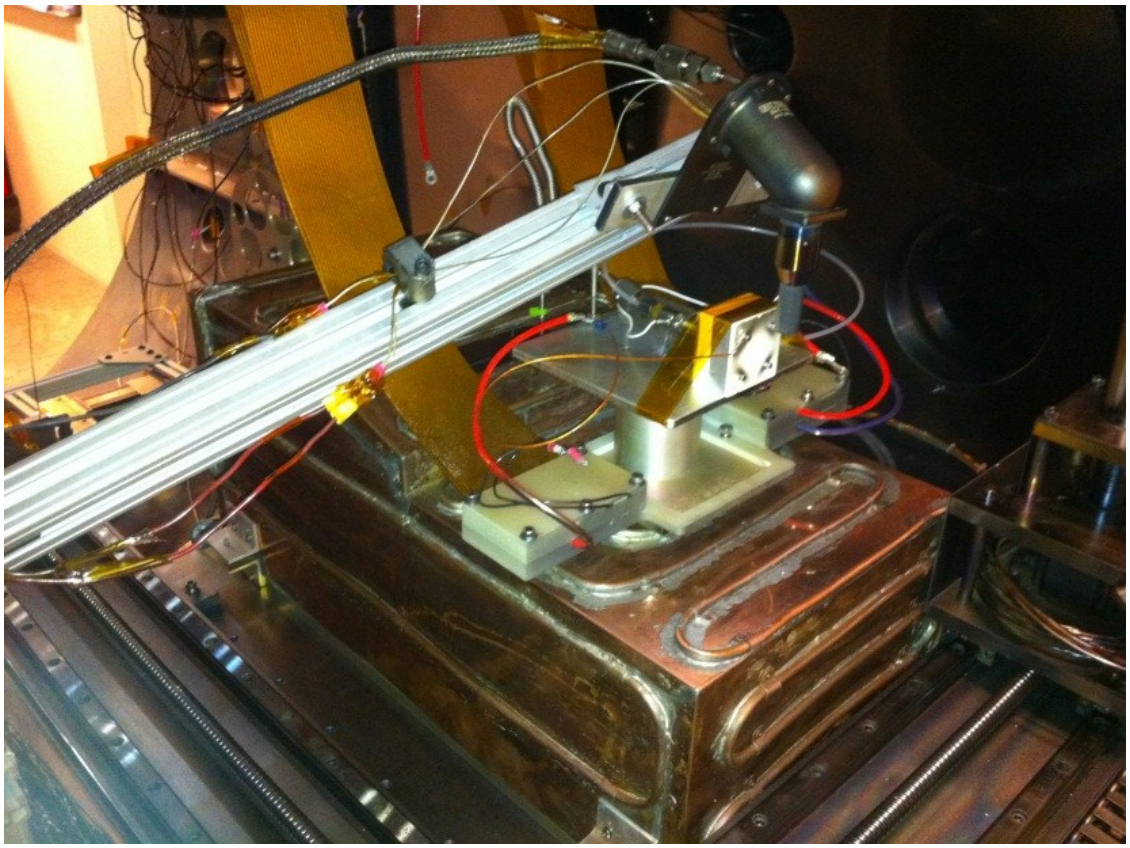

Figure 25. Thrust stand installed in chamber with BHT-20 mounted on pedestal and cathode mounted on an external sting to reduce complexity.

The thruster was calibrated before and after each attempt to measure thrust. The process involved using a stepper motor that was controlled via a switch on the thruster

readout unit to load and unload weights suspended on fishing line. These weights passed over a large, low friction, pulley in order to translate their vertical motion to a horizontal applied force on the thrust pedestal. The combined weight of each weight plus the associated length of fishing line was 0.134 grams, which provided calibration over a 0-5.2 mN range. The weights used were specifically selected for this test in order to reduce the magnitude of individual calibration steps when compared to previous setups. The thinnest flexures and lightest return spring available for the thruster stand were used in order to maximize the resolution of each calibration step. This produced reasonable calibration curves, as evidenced by Figure 26; however, the noise floor inherent in this instrument ultimately proved too large to collect any useable thrust data, as shown in Figure 27.

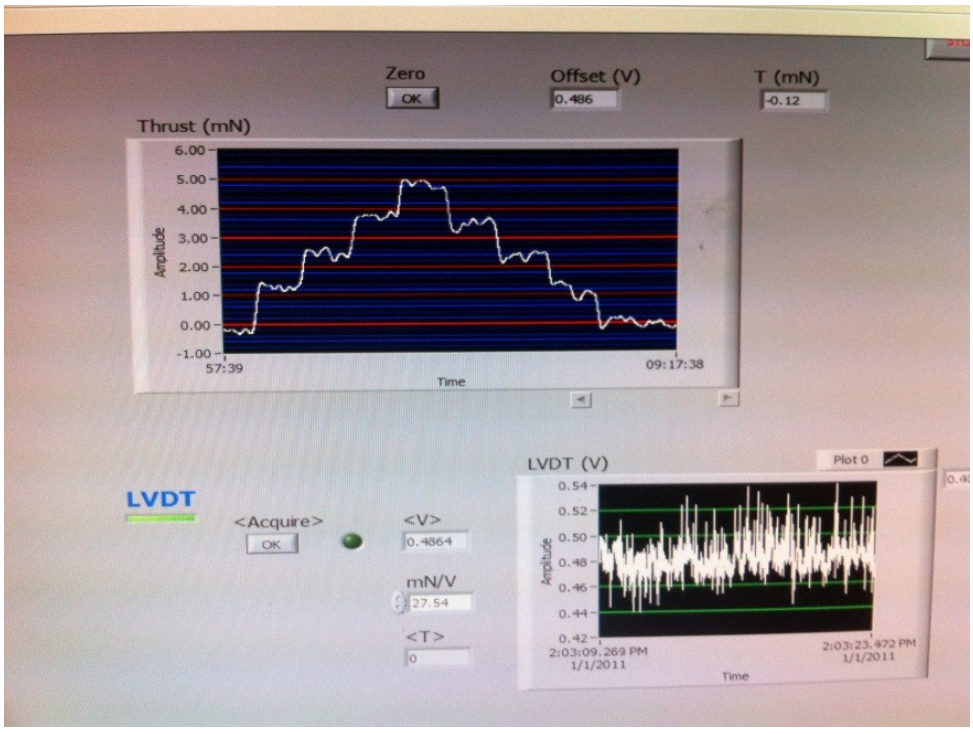

Figure 26. Thrust stand calibration curve showing some hysteresis, as illustrated by LabView interface.

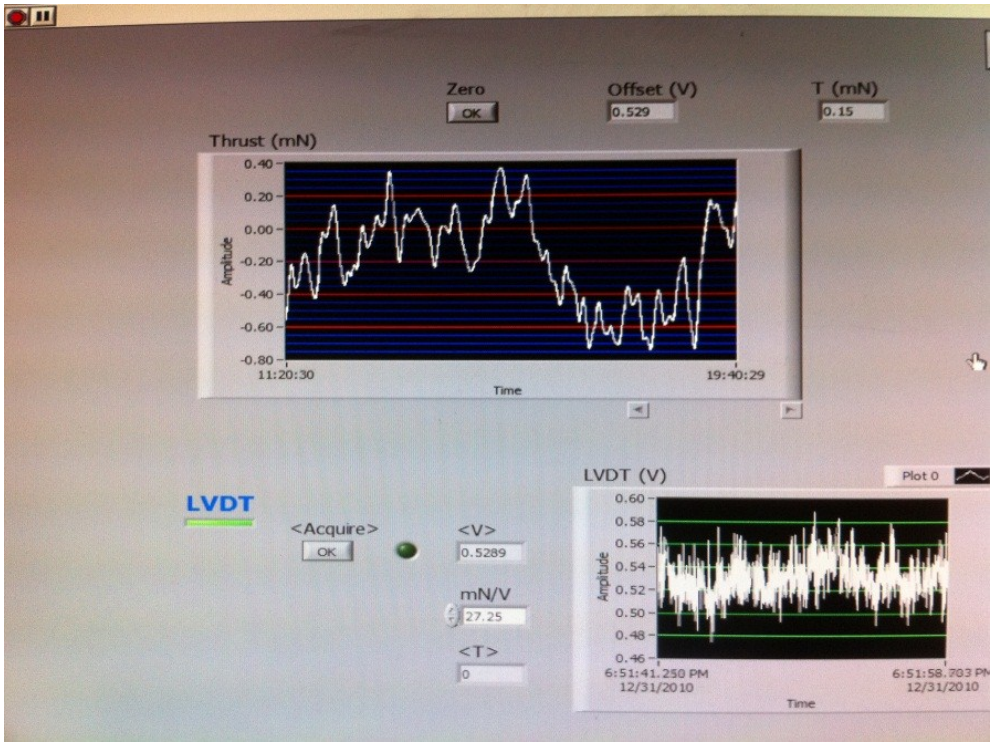

Figure 27. Thrust stand random noise collected over 20 minutes.

Torsion Balance System

AFIT's torsion balance system was designed and built by Busek to measure the low thrust levels generated by micro pulsed plasma thrusters and similar devices. The author turned to this device after it became apparent that the inverted pendulum stand simply did not possess the resolution to measure the sub-mN forces produced by the BHT-20. Several design features of the torsion balance collate to produce an extremely sensitive and stable thrust measurement platform. At the heart of this instrument is a Philtec model D125-AB fiber optic laser displacement sensor (LDS), as shown in Figure 28.

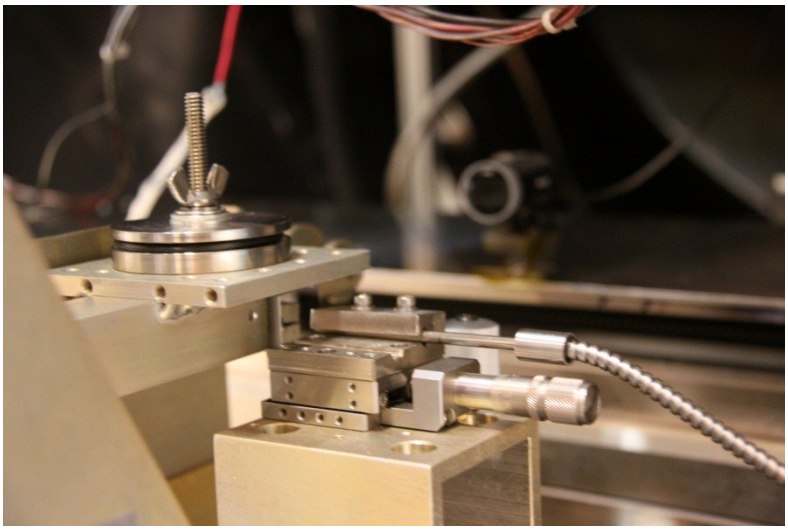

Figure 28. Laser displacement sensor mounted on micrometer translation stage.

The LDS had two linear ranges to select between for the desired application [47]. The linear range used in this study had a sensitivity of -15.3 mV/mil. The other range was so sensitive–17 times the response rate of the range selected—that it was virtually useless given the magnitude of the low frequency oscillations introduced by vibration through the chamber. The LDS proved to be incredibly stable and was especially useful, because it provided a method to account for displacement drift over time. This was essential in order to account for what the current distance between the two calibration electrodes was. This was important because the attractive force, F_{cal}, generated by the electrodes was a function of the potential difference induced between the electrodes, V_{cal}, and the distance, d, between the electrodes, as shown in (18) [47].

$$F_{cal} = \frac{(1.262\times10^{-9})(1+138.1\times d){V_{cal}}^2}{d^2} \tag{18}$$

A view of calibration electrode design is provided in Figure 29. The distance between these calibration electrodes was adjustable in 10 μm increments using a micrometer translation stage attached to the smaller electrode.

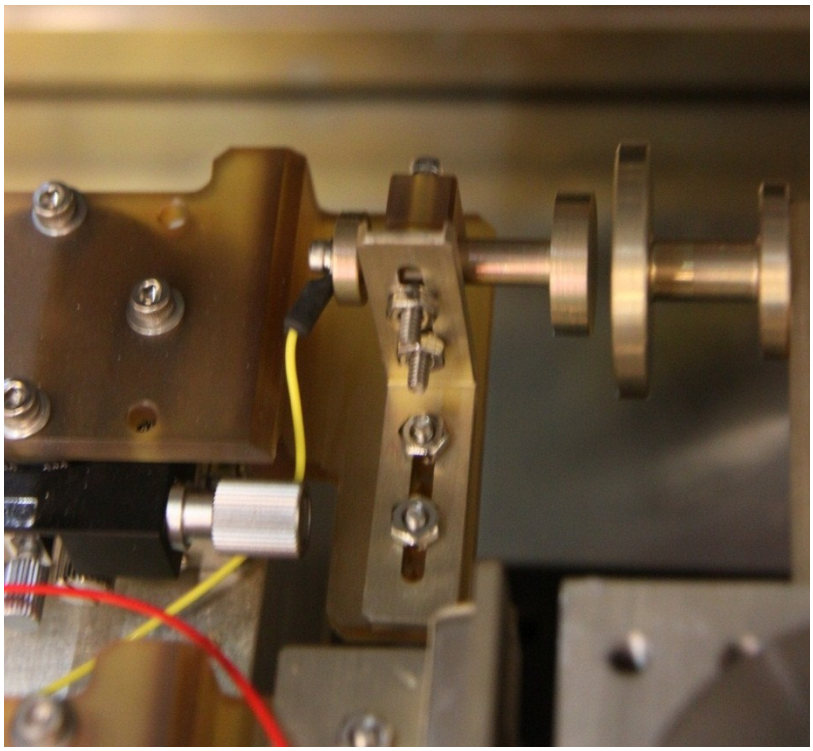

Figure 29. Torsion balance calibration electrodes.

Calibrations runs were performed immediately before and after thrust measurements in order to establish the baseline position and response function. A calibration voltage of 800 V was used in all cases. It was generated by cycling power (3.082 V with a 2 A limit) from an Agilent E3631A power supply that was routed through an EMCO model F121 high voltage amplifier to step the voltage to 800 V. The initial distance between the electrodes was set to 1.5 mm ±5 μm, and the initial LDS voltage was noted. Changes in LDS voltage were directly attributable to changes in position, so a corrected distance was calculated as part of each calibration run. The

analog voltage from the LDS was read using an Agilent 54622D, and the voltages were recorded using Agilent's IntuiLink Data Capture software, as illustrated in Figure 30. Data collection periods of 50 s were used for calibration runs, and individual thrust measurements.

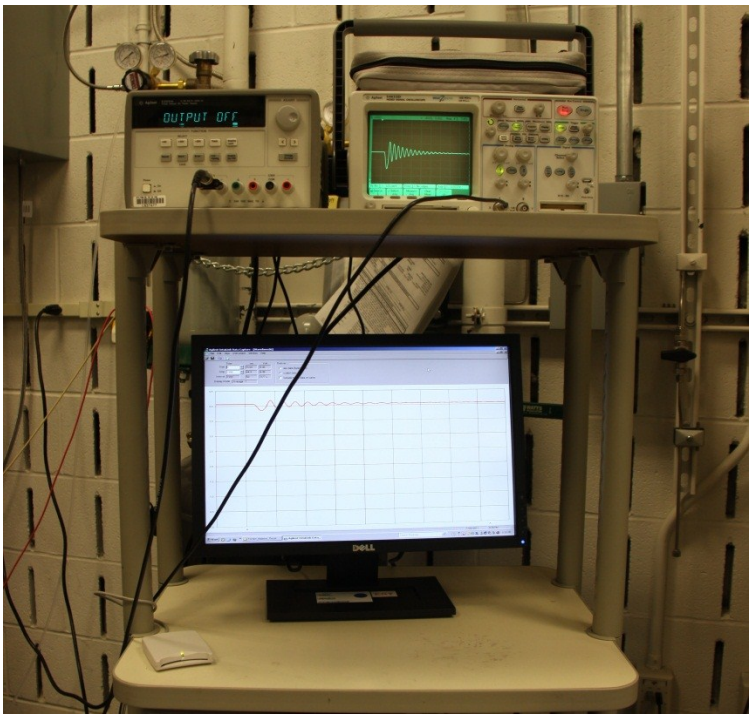

Figure 30. Torsion balance data acquisition setup.

Special care had to be taken when integrating the BHT-20 onto the torsion balance, because of the instrument's extreme sensitivity. The center of mass of the thruster was determined by balancing each axis on a knife edge. The COM of the thruster was then located above the center of thruster platen on one side of the balance arm, and a counterbalance was placed equidistance on the opposite side of the balance arm. The counterbalance was made by stacking washers above a vacuum pass-through cover until the combined total weight was within 2.5 grams of the thruster, as shown in

Figure 31. A large single loop of FTTP propellant line was used to transfer xenon to the anode in order to produce a stable spring constant, as shown in Figure 32. The cathode was mounted externally to the torsion balance, as illustrated by Figure 33.

Figure 31. Thruster counterbalance.

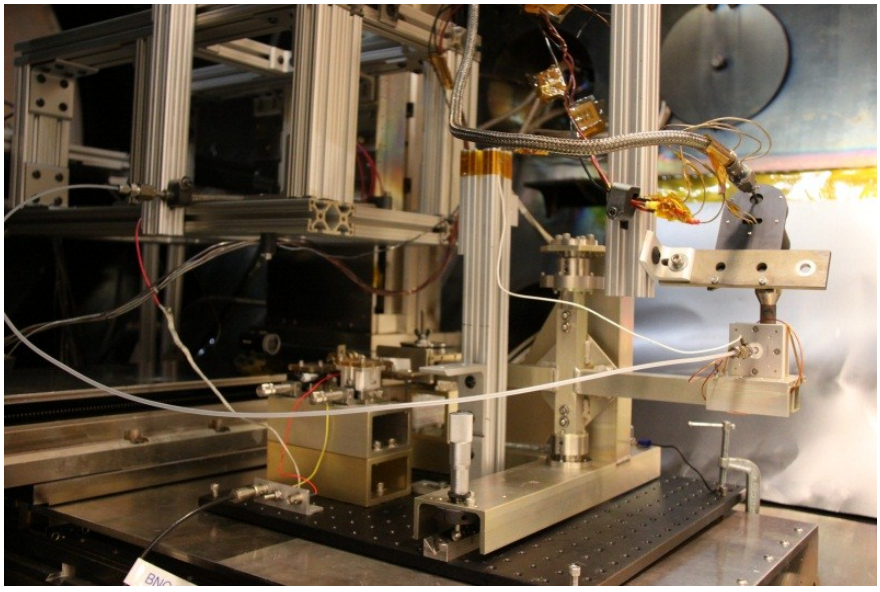

Figure 32. Back view of thruster integration onto torsion balance.

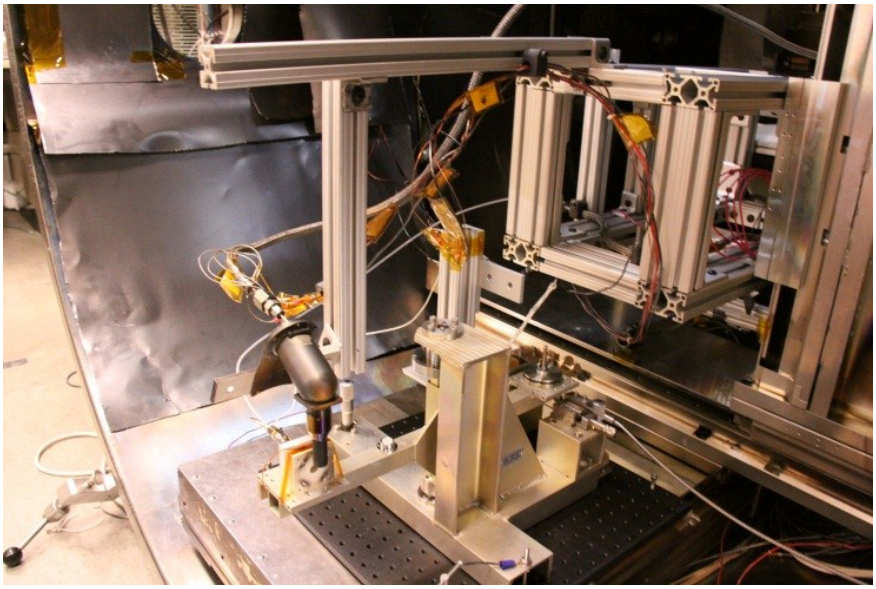

Figure 33. Front view of thruster integration onto torsion balance.

Error Analysis

The first element of error that was quantified for the torsion balance was the standard error associated with the thrust measurements. At each operating point, five 50 s collections were performed at 40 Hz. Each of these data collections was then averaged and the standard deviation, σ, associated with these averages calculated. The standard error, with a confidence factor of 95%, was then calculated using the method discussed previously.

The calibration bias, Δb_{cal}, was determined for each operating point. A range of two to seven calibration runs were performed for each operating point, and it was desirable to capture the variation in resulting calibration slopes values, y_i. This was done by first calculating the average of the calibration slopes, $\bar{y}$, and then using (19) to calculate Δb_{cal}.

$$\Delta b_{cal} = \sqrt{\frac{\sum(y_i - \bar{y})}{N}} \quad (19)$$

The error associated with the thruster drift, Δb_d, was also quantified. The calculation of Δb_d consisted of a comparison of the voltage baseline before, V_{zero-}, and after thrust measurements, V_{zero+}, using (20).

$$\Delta b_d = \frac{(V_{zero-} - V_{zero+})}{2} \quad (20)$$

The error for the resolution bias, Δb_{res}, of the LDS was also calculated. The Agilent data capture software captured voltage to 1 mV. The resolution bias was obtained by dividing that value in half and then multiplying by the measured change in voltage produced by firing the thruster. In all cases, this change in voltage was less than the change in voltage produced by the calibration force.

The total thrust stand measurement error was calculated using the relationship expressed in (21).

$$error = \sqrt{SE^2 + \Delta b_{cal}^2 + \Delta b_d^2 + \Delta b_{res}^2} \quad (21)$$

IV. Results

This chapter enumerates the performance results of the BHT-20 derived from the experiments outlined above. The voltage-current characteristics of this thruster are outlined. A maximum suggested operating power is provided for the thruster. Faraday data is reviewed for multiple cases in order to make attributions about beam current, beam efficiency, and the influence of cathode position on plume divergence. Thrust measurement results are tabulated and reported both with and without the inclusion of the BHC-1500 in order to differentiate the influence of the cathode on the results, especially with relation to I_{sp} and efficiency.

Voltage-Current Characteristics

The anode current and voltage were measured at five flow rates during multiple thruster runs. In all of these cases the cathode and anode were both set to a flow rate of 1 sccm on startup and the discharge voltage was initially set to 170 V. Once thruster ignition occurred the anode flow rate was reduced and the current allowed to stabilize. The discharge voltage was then varied from 148 to 248 V, while the anode flow rate was held at a constant flow rate. This procedure was repeated for five flow rates. As expected, the rate at which discharge current increased with respect to an increase in anode potential became more pronounced as the flow rate increased. It was also observed that at some operating points the thruster did not settle to a stable or repeatable value. This was the case, for example, when the thruster was operating at 0.7 sccm and 180 V, as illustrated in Figure 34. It was believed that the cause of the fluctuations was due to ionization instability at those operating points, but further testing would be

required to confirm this point. Notably, this behavior seemed to occur over a limited discharge voltage range. The plot reveals that the BHT-20 provided many stable operating points spanning the range of 5 – 25 Watts.

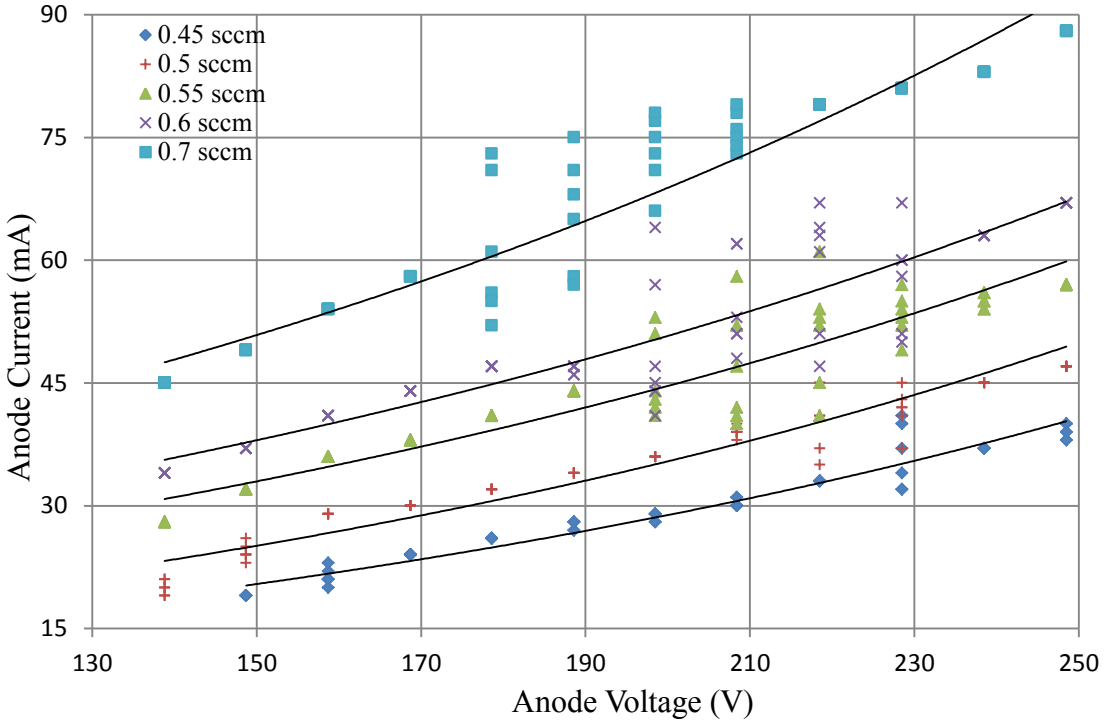

Figure 34. Voltage-current characteristics of BHT-20.

The experimental setup used for the collection of voltage-current data also enabled the simultaneous capture of a high resolution image of the thruster at each operating condition. These side-view images illustrate how the plasma plume shape became more pronounced and extended farther from the thruster face as the discharge voltage was increased from 148 to 248 V at the constant anode flow rate of 0.45 sccm. The two extreme cases are shown in Figure 35 and 36. The remaining nine images associated with the 0.45 sccm curve are included in Appendix B. The appreciable pink glow discharge in these images was a byproduct of the comparatively significant 1 sccm

flow rate through the cathode that was being used during testing. The typical blue glow discharge associated with ionized xenon is difficult to separate at the low voltage cases, but it becomes increasingly pronounces as the discharge voltage was increased. In all cases the discharge looked reminiscent of a 'ball plume' mode for a traditional Hall effect thruster. As noted, the central portion of the plume shape is difficult to identify at low voltages, but the shape high density discharge beam was readily apparent at higher discharge voltages. Further insight into the reason for the plume shape seen in these images is included with the Faraday results section. An attempt was initially made to extend the voltage current curves beyond the range presented in Figure 33, but it was found that this was highly detrimental to thruster longevity.

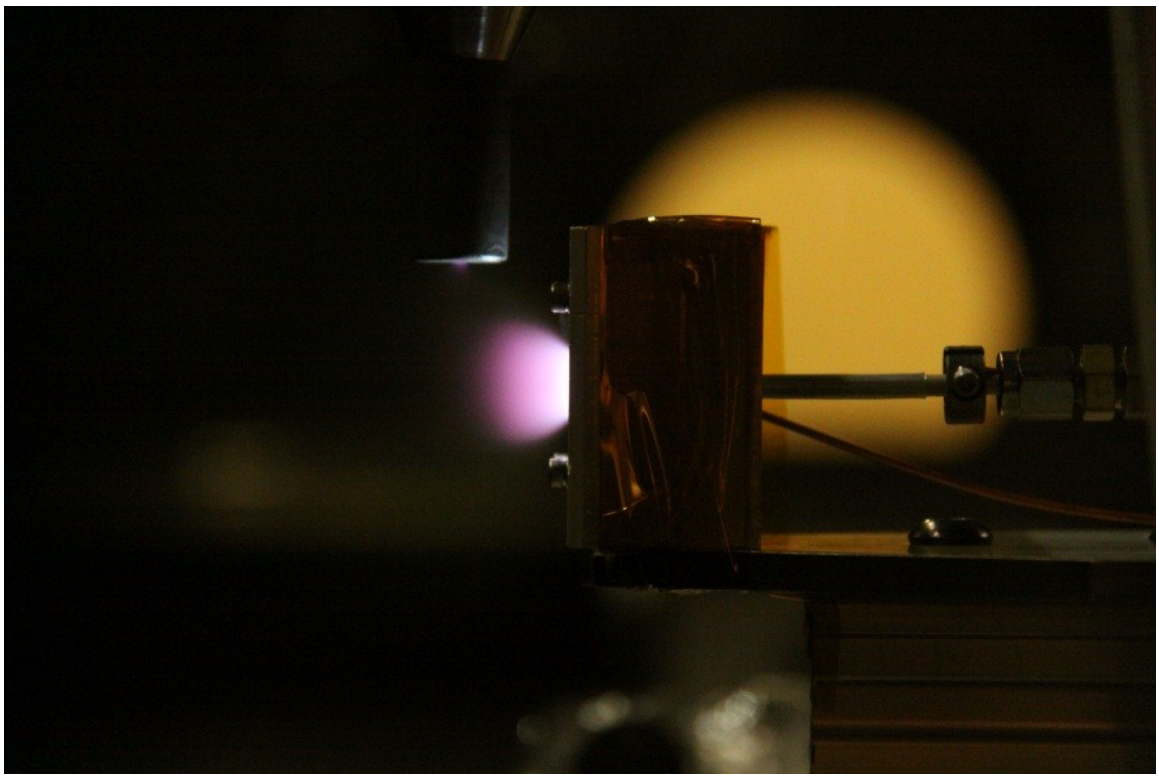

Figure 35. BHT-20 plume with V_d of 138 V and m_a of 0.45 sccm.

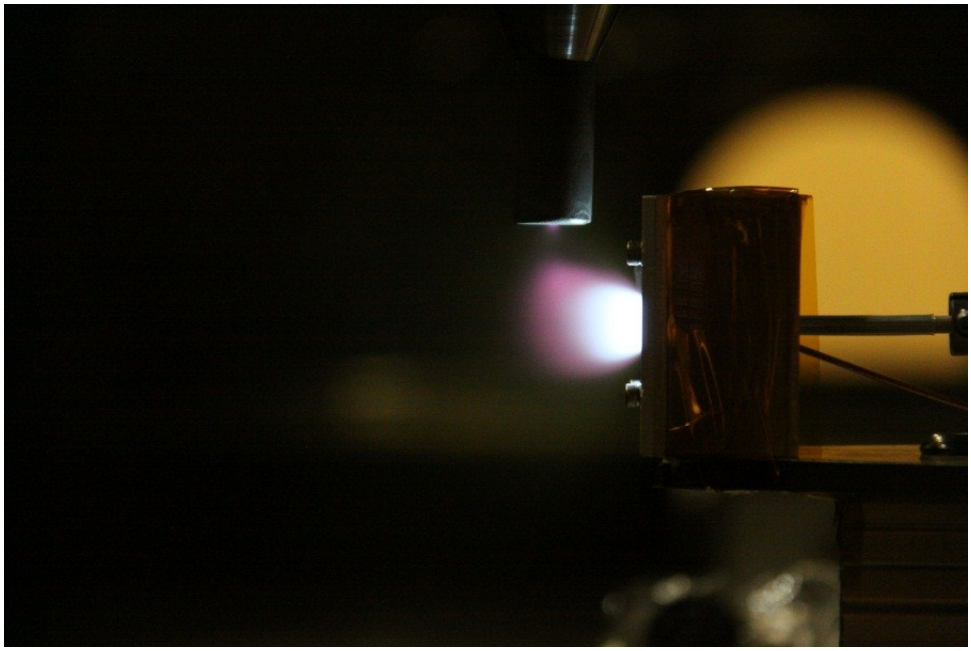

Figure 36. BHT-20 plume with V_d of 248 V and m_a of 0.45 sccm.

BHT-20 Operating Limits

The BHT-20 was originally designed with the intention to operate with a discharge power of 20 W. Early experimentation was done to determine the effect of operating beyond this point in order to understand if there would be any implications for thruster longevity. It was quickly discovered that operating at 25 Watts for hours produced negligible degradation of the thruster's anode post, while operating at 45 Watts rapidly degraded the post. After three hours of operation with power levels ranging from 20-45 Watts, the BN anode post was eroded to the point where the mounting screw that held it in place was mostly exposed, as illustrated by Figure 37. If thruster operation were to continue at this power level for an extended period of time then it is expected that anode damage would occur and thruster performance would degrade. Fortunately, the anode post was designed to be easily replaced in order to facilitate such experimentation.

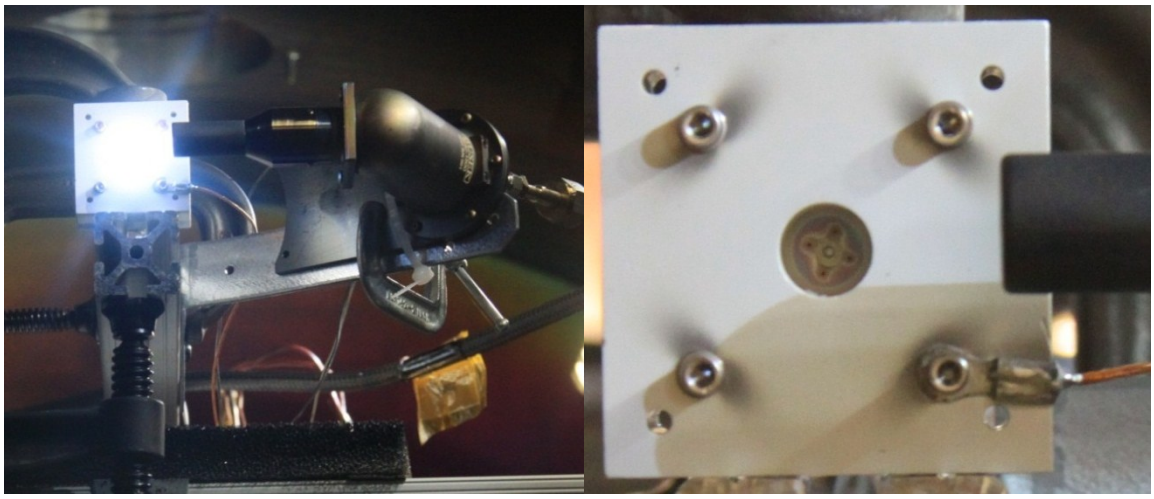

a) Thruster operating at peak of 45 W b) Resulting damage to BN anode post.

Figure 37. Damage to thruster after operation beyond design limit.

Alternatively, when the thruster was operated over a range of 5-25 Watts for more than 70 hours, no apparent degradation in the condition of the anode post occurred, as shown in Figure 38. It is proposed that this is an area of interest that should be monitored in all future testing due to the necessity of low power electric propulsion devices to compensate for low thrust levels with reasonable Isp values and long operational lifetimes. For obvious reasons, further testing was limited to less than 25 W.

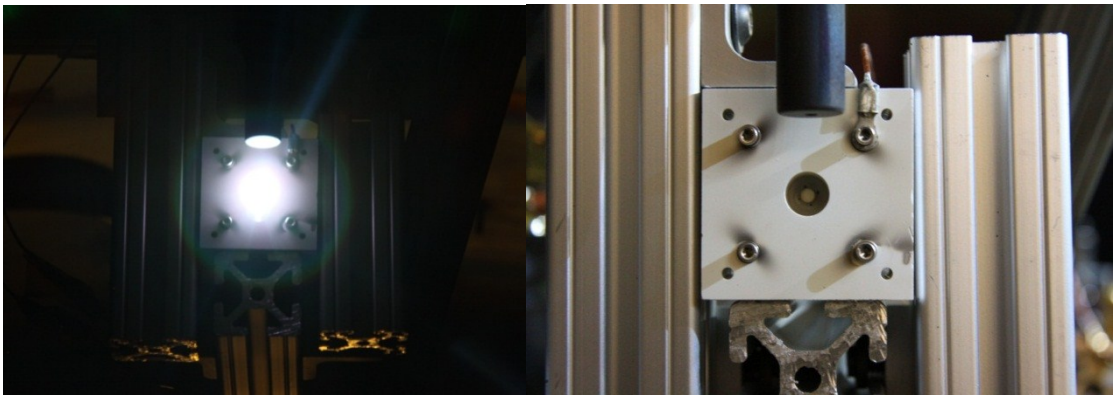

a) Thruster operating at peak of 25 W b) No damage to BN anode post.

Figure 38. No damage to thruster after extended operation at design limit.

Faraday Data

The Faraday probe is a well-established instrument that has been widely used to characterize electric thrusters. The two most important traditional values that can be derived from Faraday data are the beam current and divergence angle. The beam current can be used to calculate a beam efficiency that relates how effectively the thruster is using the current flowing from the cathode to anode to generate the ions that produce the plasma plume. The divergence angle has important implications for spacecraft integration, especially with regard to components that are especially susceptible to sputtering erosion, such as solar panels. The divergence angle is also related to the thrust factor that conveys how efficiently momentum transferred to ions in the plume will translate to propulsive thrust.

The experimental techniques for conducting Faraday probe measurements of a Hall effect thruster are well established, which is always ideal when trying to establish baseline performance values for a new thruster design. For this study, Faraday probe measurements were taken at different power levels, thruster orientations, and with the cathode in different positions relative to the thruster in order to identify how these changes affected the performance measures described above. Further, the shapes of the current density versus view angle plots are useful for making comparisons with existing Hall effect thruster designs. However, before useful comparative Faraday data was collected, it was decided that an appraisal of the noise floor should be performed.

The first Faraday probe data collected was a measurement of the background noise level in the chamber. This was done at a vacuum level of $9.7 \cdot 10^{-8}$ torr without current or propellant flowing to the thruster and cathode. The derived average current

densities at radii of 13 and 15 cm were -2.05 · 10^{-5} and -2.02 · 10^{-5} $\frac{mA}{cm^2}$, respectively. These averages were more than three orders of magnitude below the peak current density measured for the thruster when operating at 5 Watts, and the two distributions were random without any statistical correlation to distance, as illustrated by Figure 39. Given these factors, no offset correction was performed on the measured data to correct for the noise floor. This was a conservative omission as a correction to the data would have resulted in a positive offset. Once an understanding of the noise inherent in the instrument was obtained, an examination of appropriate test radii was conducted.

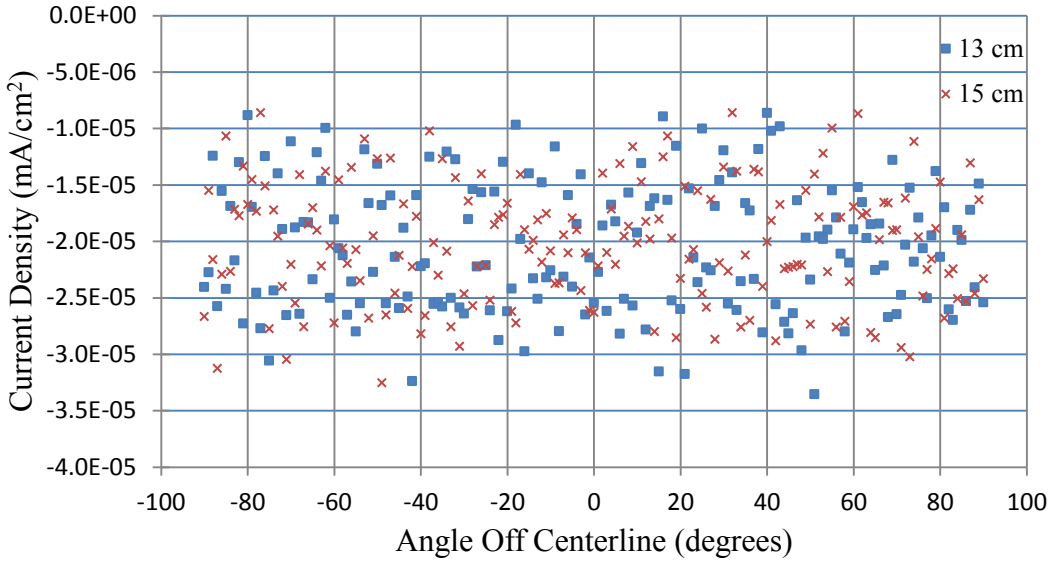

Figure 39. Background noise for Faraday probe measurements.

The second Faraday test was used to select and validate two sweep radii that were utilized throughout the remainder of Faraday measurements in order to ease direct comparisons of current density distributions at various operating conditions. The current density in a plasma plume reduces quadratically with increased distance from the source, which necessitated the selection of measurement radii that produced reasonable signal to

background noise ratios. The low power output of the BHT-20 called for performing Faraday sweeps at a reduced distance from the thruster face when compared to previous research performed at AFIT using the higher power BHT-200 and BHT-1500 thrusters. However, previous research performed using this Faraday probe also suggested that if measurements were taken too closely to the source then the thruster itself would influence the measured data due to the generation of electromagnetic noise [42]. Initial Faraday runs were taken at constant radii varying between 30 and 40 cm, but the resulting current levels were deemed lower than was desirable. Additional testing at radii of 13 and 15 cm yielded acceptable measured current levels for all of the operating points of interest.

The derived values generated from the average of five successive Faraday sweeps at 13 and 15 cm were then compared with the derived values generated from five successive sweeps at 11 and 17 cm. The objective was to determine if the current density distribution, beam efficiency, and divergence angle remained consistent between sweeps that were conducted at different times and different radii. The results from this test proved to be sufficiently consistent to instill confidence in the validity of using 13 and 15 cm radii for the remainder of Faraday measurements, as illustrated by Table 2 and Figure 40. The beam efficiency, η_b, dropped slightly due to plume loss factors and divergence angle, θ, increased slightly due to ion repulsion. The magnitude of the current density plot declined appropriately with distance, as substantiated by the consistency between the integrated beam current values, I_b, and the shape of the distribution remained consistent as the measurement radius increased. For comparison, the value for the beam efficiency was approximately 40% across all cases, but an efficiency of approximately 60% would

have been expected for a highly tuned 200 Watt class annular Hall effect thruster [48]. Further, traditional Hall thrusters tend to produce highly symmetric discharge plumes, so it was decided that the incongruencies between the left and right halves of Figure 39 warranted further investigation.

Table 2. Derived beam parameters for 4 W operating condition.

Vacuum (torr)	Radius (cm)	Power (W)	V_d (V)	I_d (mA)	I_b (mA)	η_b (%)	θ (deg)	F_a	SE (%)
9.51E-07	11	4.05	168.7	24	9.77	40.71	69.16	0.052	0.38
9.32E-07	13	4.05	168.7	24	9.68	40.32	68.92	0.056	0.24
9.32E-07	15	4.05	168.7	24	9.63	40.11	68.95	0.048	0.08
9.51E-07	17	4.05	168.7	24	9.63	40.10	70.01	0.053	0.13

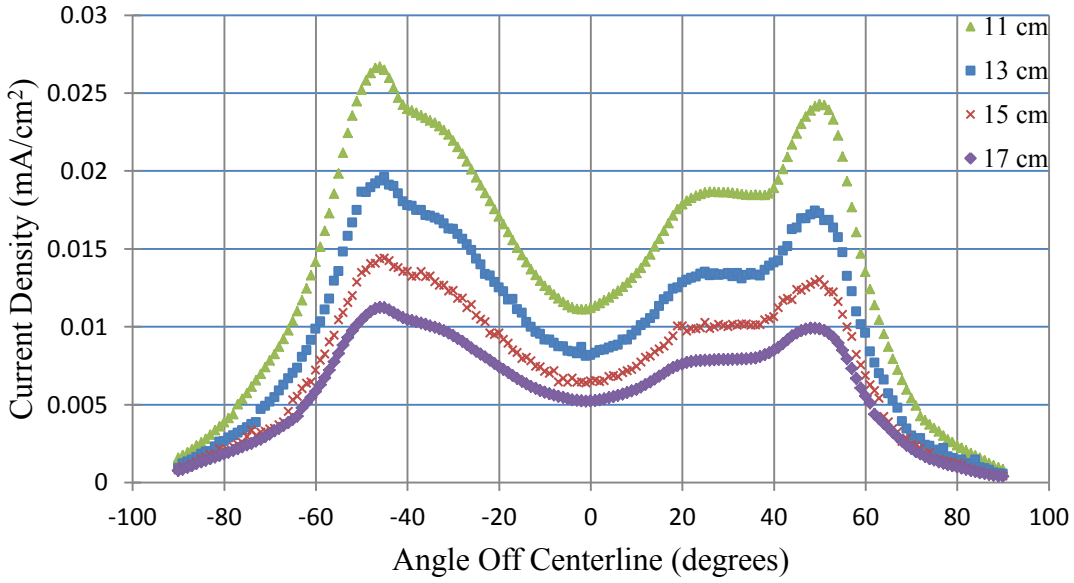

Figure 40. Current density curves for 4 W operating condition, showing consistent profiles and appropriate quadratic falloff.

Plume Symmetry

The current density profiles generated from operation at 4 W illustrated two initially surprising attributes. The first was that the peak current density measurement did

not occur along the centerline of the thruster, as was typical of annular Hall effect thruster designs [49]. The "halo" shape was also not typical of curricular Hall effect thruster designs with electromagnetic coils, which also generated their peak current density along the thruster centerline, but with a higher divergence angle than was typical of annular designs [50]. Instead, the distribution was reminiscent of the results generated by circular Hall effect thrusters with permanent magnets, which have current density profiles characterized by twin peaks with a substantially lower centerline value [51]. Extensive studies of the latter phenomenon by the Princeton Plasma Physics Laboratory suggest that the cause of the halo shape resulted from inconsistencies in the magnetic field topology in the vicinity of the discharge channel exit [52]. It was believed that the same explanation was also a viable cause of the relative asymmetry between the left and right halves of the current density distribution.

Additional Faraday measurements were performed at 4.7 and 13.6 W operating points in order to determine if the halo distribution and asymmetry were consistently present. The thrust asymmetry factor, F_a, for these cases is provided in Table 3 and 4. The results suggest that thrust asymmetry and the general shape observed at 4 W were consistent issues, but the degree of asymmetry present in the 13.6 W case was less than half that of the 4 or 4.7 W case. Unfortunately, the beam efficiency and divergence angle were both less desirable in the 13.6 W case. A graph of the current density distribution for 4.7 and 13.6 W operating points is provided in Figure 41 and 42. The shapes of the 4 and 4.7 W distributions were remarkably similar, whereas the shape of the right peak for the 13.6 W case was substantially more uniform–without any appreciable step on the right half of the plume.

Table 3. Derived beam parameters for 4.7 W operating condition.

Vacuum (torr)	Radius (cm)	Power (W)	V_d (V)	I_d (mA)	I_b (mA)	η_b (%)	θ (deg)	F_a	SE (%)
1.00E-06	13	4.72	168.7	28	11.79	42.09	69.24	0.058	2.48
1.00E-06	15	4.72	168.7	28	11.70	41.78	69.43	0.053	1.55

Table 4. Derived beam parameters for 13.6 W operating condition.

Vacuum (torr)	Radius (cm)	Power (W)	V_d (V)	I_d (mA)	I_b (mA)	η_b (%)	θ (deg)	F_a	SE (%)
1.25E-06	13	13.57	178.6	76	27.17	35.75	73.92	0.032	0.77
1.25E-06	15	13.57	178.6	76	27.14	35.71	74.20	0.029	0.44

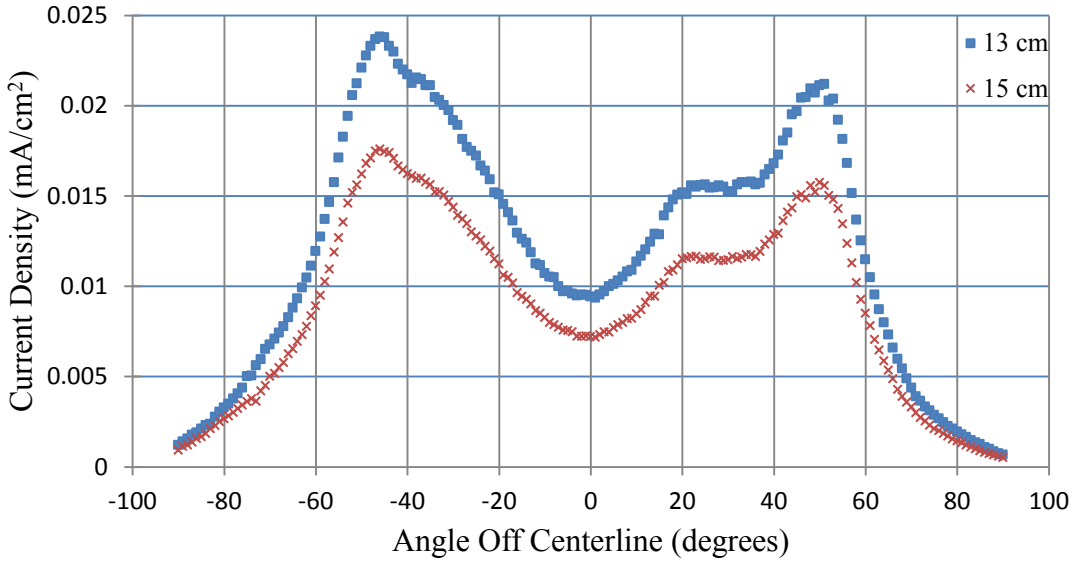

Figure 41. Current density curves for 4.7 W operating condition.

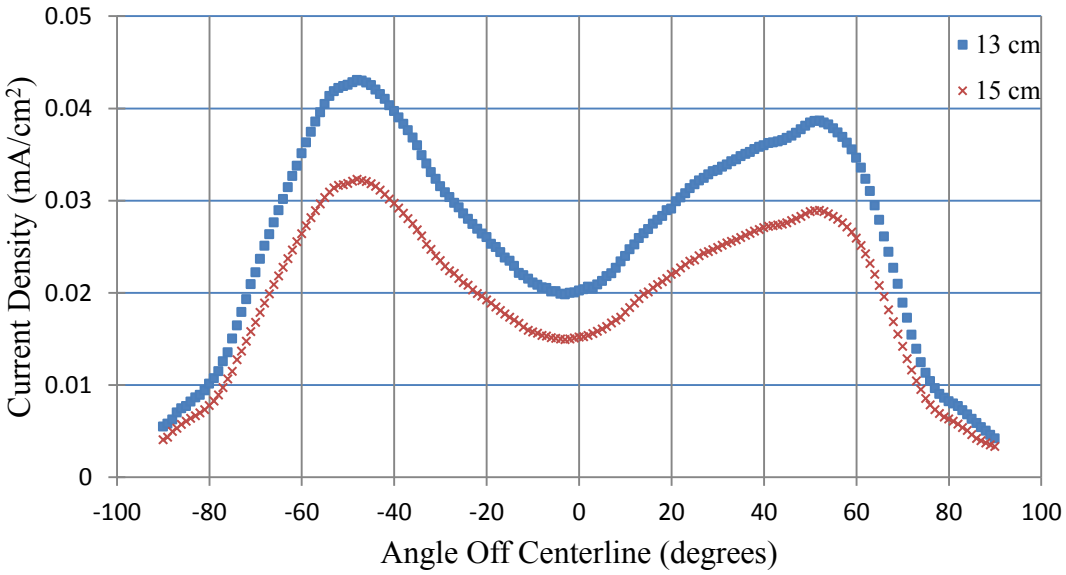

Figure 42. Current density curves for 13.6 W operating condition.

Conclusions about current density asymmetry from the first three cases had one significant limitation. The measurements were all taken along the same bisecting plane and the asymmetry phenomenon was inherently a three dimensional attribute. Thus, in order to gain a better understanding of the asymmetry, the 4.7 and 13.6 W cases were repeated after the thruster had been rotated 90 degrees clockwise, with respect to the front face. The thrust asymmetry factor for these cases is provided in Table 5 and 6. The results for both of these cases were consistently lower thrust asymmetry factors than for the values reported above at the same respective power levels. This suggests that many rotations at finer degree increments would be required in order to accurately define the true thrust asymmetry. Similarly, the beam efficiency improved for the 4.7 W case and degraded for the 13.6 W case, with respect to the previous measurements, and the divergence angle broadened for the 4.7 W case and narrowed slightly for the 13.6 W case. These observations provide further motivation for future plume studies on this

thruster to include numerous thruster rotations. A graph of the current density distribution for these 4.7 and 13.6 W operating points is provided in Figure 43 and 44. The general shape of these distributions was consistent with the previous test, but fine details near the peaks illustrate subtle changes that resulted from the 90 degree thruster rotation. The distribution for the rotated 4.7 W case illustrates a broadening of the left peak and an increase in the right plateau relative to the right peak. The distribution for the rotated 13.6 W case illustrates a five degree shift towards the centerline for the left peak. These changes serve to reinforce the validity of the changes in the reported F_a values. It was suggested that the cathode position may have some influence on the shape of the current density curves, so a study was devised to look at the impact of varying cathode position in small increments.

Table 5. Derived beam parameters at 4.7 W operating condition with thruster rotated 90 degrees with respect to configuration for Table 3.

Vacuum (torr)	Radius (cm)	Power (W)	V_d (V)	I_d (mA)	I_b (mA)	η_b (%)	θ (deg)	F_a	SE (%)
9.73E-07	13	4.72	168.7	28	11.14	39.78	67.61	0.023	0.10
9.73E-07	15	4.72	168.7	28	11.13	39.77	67.75	0.020	0.09

Table 6. Derived beam parameters at 13.6 W operating condition with thruster rotated 90 degrees with respect to configuration for Table 4.

Vacuum (torr)	Radius (cm)	Power (W)	V_d (V)	I_d (mA)	I_b (mA)	η_b (%)	θ (deg)	F_a	SE (%)
1.20E-06	13	13.75	178.6	77	27.75	36.03	75.05	0.006	0.19
1.20E-06	15	13.75	178.6	77	27.77	36.06	75.12	0.004	0.14

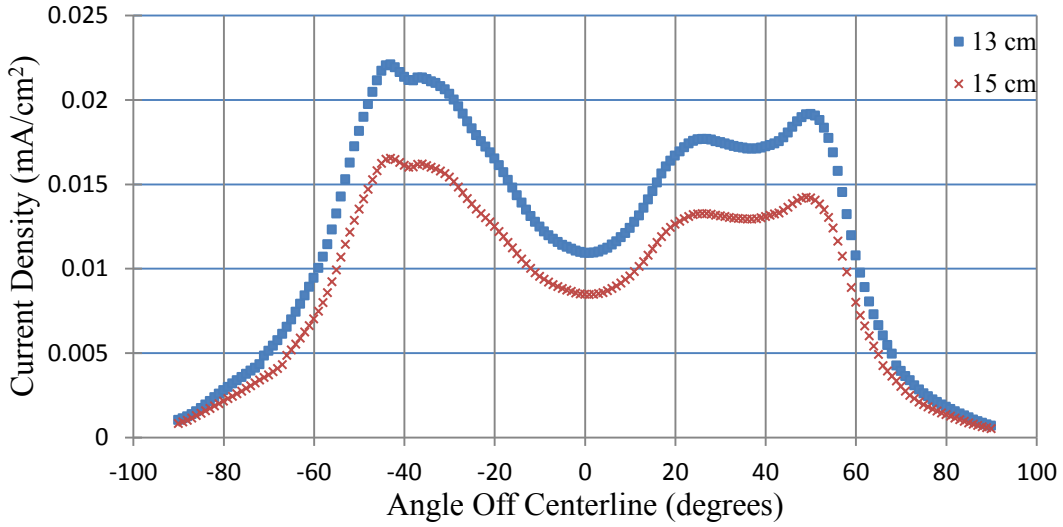

Figure 43. Current density curves for 4.7 W operating condition with thruster rotated 90 degrees with respect to configuration for Figure 40.

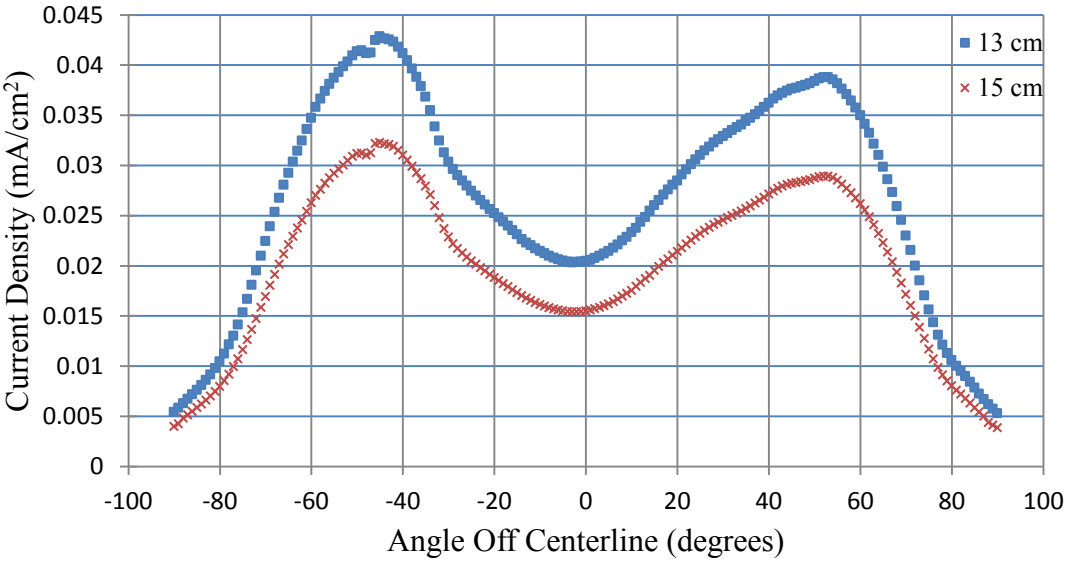

Figure 44. Current density curves for 13.6 W operating condition with thruster rotated 90 degrees with respect to configuration for Figure 41.

Variation of Cathode Position

The BHT-20 was initially operated with the hollow cathode limited to a single position; the cathode exhaust port was 1.59 cm above the centerline of the thruster discharge channel and 1.59 cm from the front face of the thruster. This placement would

pose particular challenges for integration onto a very small spacecraft, so it was desirable to look at the impact of moving the cathode relative to the thruster. The cathode was moved farther away from the thruster centerline in 1 mm increments over a range of 1.59 to 2.09 cm. The cathode was also moved relative to the thruster face in 1 mm increments over a range of 1.39 to 1.89 cm. The two axes the cathode was moved along are illustrated in Figure 45. In all cases the anode mass flow rate was held constant at 0.48 sccm.

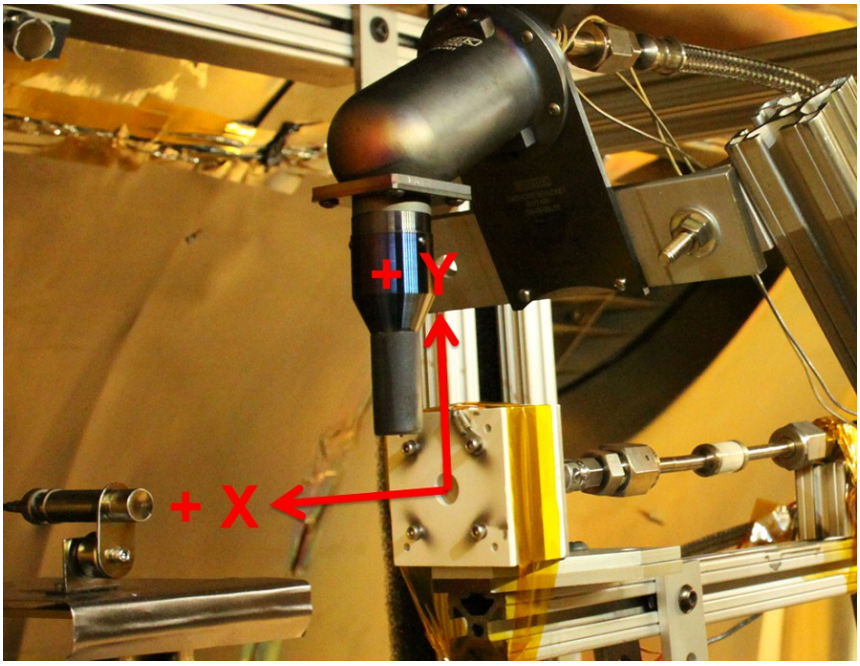

Figure 45. Axes used for movement of the cathode relative to the thruster face and centerline.

It was found that the shape of the current density plot and divergence angle were the only two derived performance measures that significantly changed over the 11 test cases conducted at varying cathode positions. Results from the two extreme points are included below in Table 7 and 8 and Figure 46 and 47 to illustrate the point. It is notable that increasing the distance from the centerline consistently increased the divergence

angle and decreasing the distance relative to the thruster face consistently increased the divergence angle, as illustrated by Figure 48. Thus, the divergence angle reported in Table 7 shows a nearly six degree reduction in divergence angle when compared to the values in Table 8, It was believed that changes in the cathode coupling voltage were responsible for the observed relationship between cathode position and divergence angle based on previous results from Sommerville and King on Hall effect thrusters [53]. The left peak of the current density plot for Figure 44 was shifted nearly 10 degrees closer to the thruster centerline relative Figure 45. The plateau in Figure 44 became the right peak, whereas the right peak for Figure 45 was consistent with previous results at 4.7 W. Quantitative results from the additional test cases are included in Appendix C. The next step in the characterization of the thruster was to expand the Faraday data to capture the extreme points of the BHT-20 operating range.

Table 7. Derived beam parameters for 4.7 W operating condition with cathode 1.59 cm above thruster centerline and 1.29 cm from thruster face.

Vacuum (torr)	Radius (cm)	Power (W)	V_d (V)	I_d (mA)	I_b (mA)	η_b (%)	θ (deg)	F_a	SE (%)
9.39E-07	13	4.72	168.7	28	11.20	39.99	64.99	0.021	1.02
9.39E-07	15	4.72	168.7	28	11.20	39.99	64.56	0.016	0.93

Table 8. Derived beam parameters for 4.7 W operating condition with cathode 2.09 cm above thruster centerline and 1.59 cm from thruster face.

Vacuum (torr)	Radius (cm)	Power (W)	V_d (V)	I_d (mA)	I_b (mA)	η_b (%)	θ (deg)	F_a	SE (%)
9.39E-07	13	4.72	168.7	28	11.06	39.52	70.07	0.021	0.82
9.39E-07	15	4.72	168.7	28	11.14	39.77	70.94	0.022	0.97

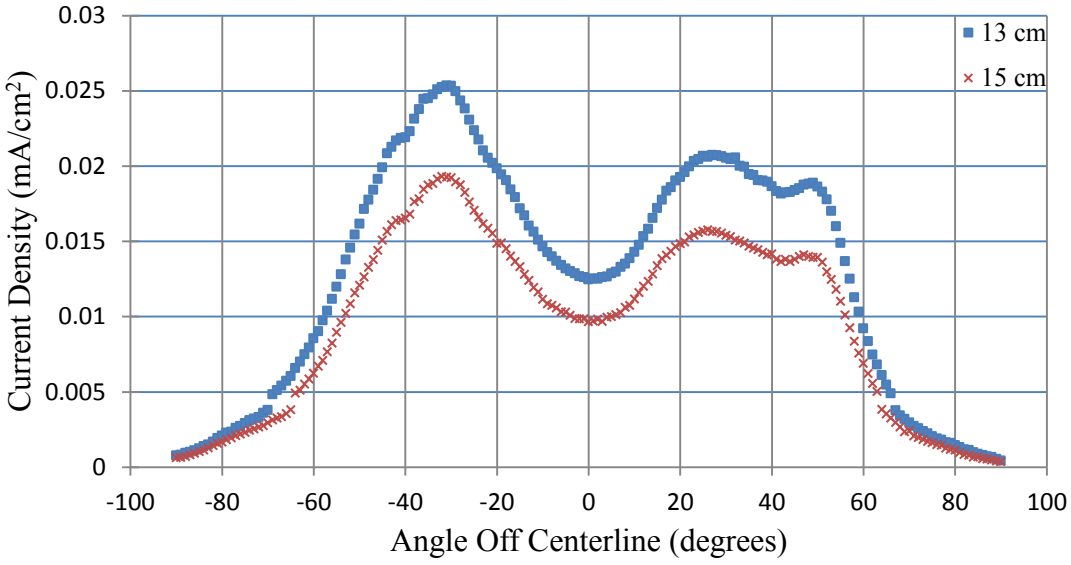

Figure 46. Current density curves for 4.7 W operating condition with cathode 1.59 cm above thruster centerline and 1.29 cm from thruster face.

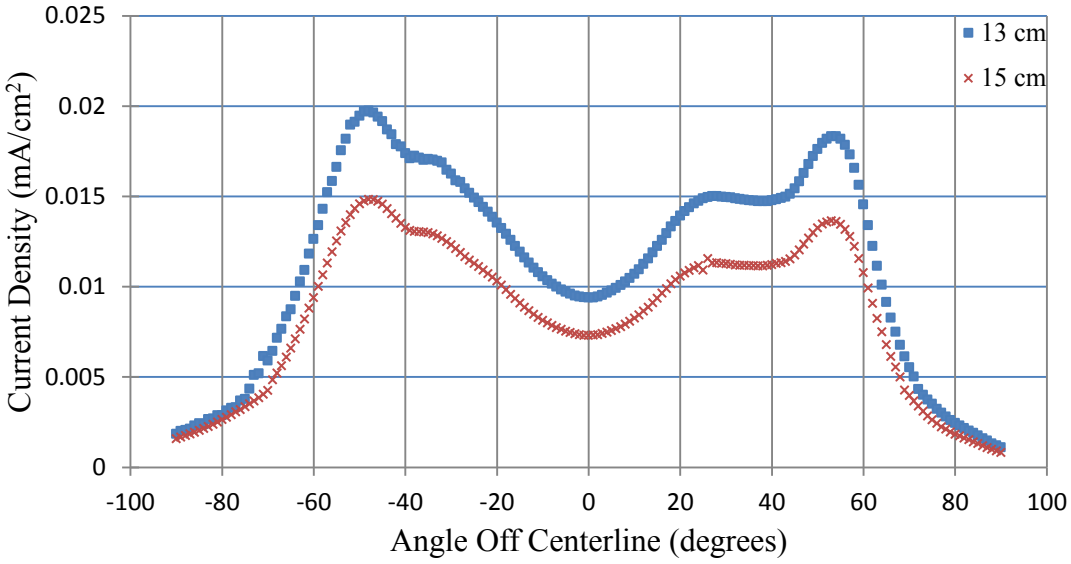

Figure 47. Current density curves for 4.7 W operating condition with cathode 2.09 cm above thruster centerline and 1.59 cm from thruster face.

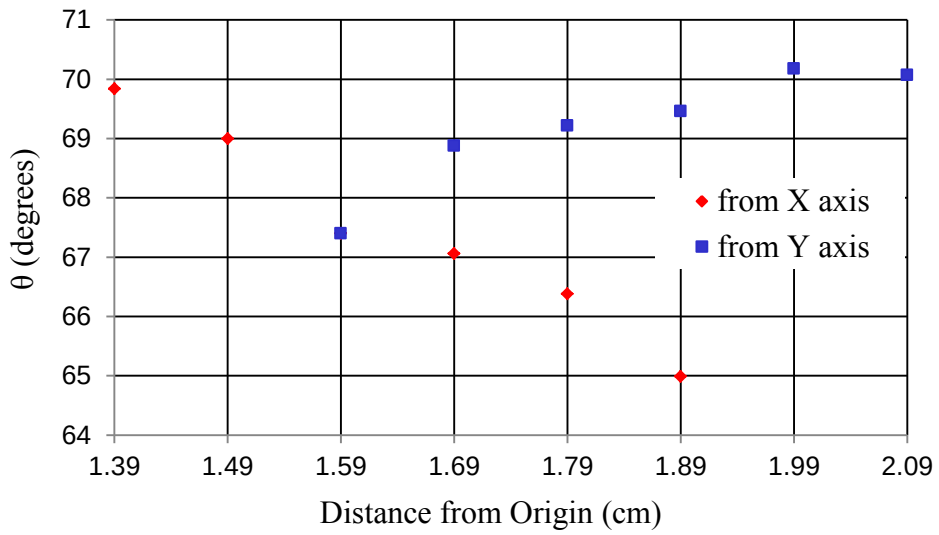

Figure 48. Plot of divergence angle as a function of distance from the X and Y axis, respectively.

Performance Envelope

As evidenced by the previous test cases, the author had a strong interest in the ability of the BHT-20 to operate at power levels below the rated 20 W for the thruster. This concentration stemmed from the suggestion that the thruster was a possible candidate for very small satellites with highly constrained power budgets. Nonetheless, it was also prudent collect Faraday data over the entire thruster operating range in order to understand how the derived performance parameters varied with discharge power.

On the low end of the scale, it was possible to stably and repeatedly operate the thruster down to a power level of 2.5 W. The derived results for that operating condition are provided in Table 9 and Figure 49. The values presented are consistent with those reported for operation at 4 and 4.7 W, but it was noteworthy that the beam efficiency was the highest of any operating condition tested over the entirety of this study. Similarly, the shape of the current density plot was similar to the 4 and 4.7 W cases, but a noticeable

narrowing of the beam was visible. On the opposite end of the spectrum, a 20 W case was identified for comparison purposes.

Table 9. Derived beam parameters for 2.5 W operating condition.

Vacuum (torr)	Radius (cm)	Power (W)	V_d (V)	I_d (mA)	I_b (mA)	η_b (%)	θ (deg)	F_a	SE (%)
1.00E-06	13	2.53	148.7	17	7.26	42.71	69.70	0.035	0.53
1.00E-06	15	2.53	148.7	17	7.31	43.03	69.87	0.032	0.62

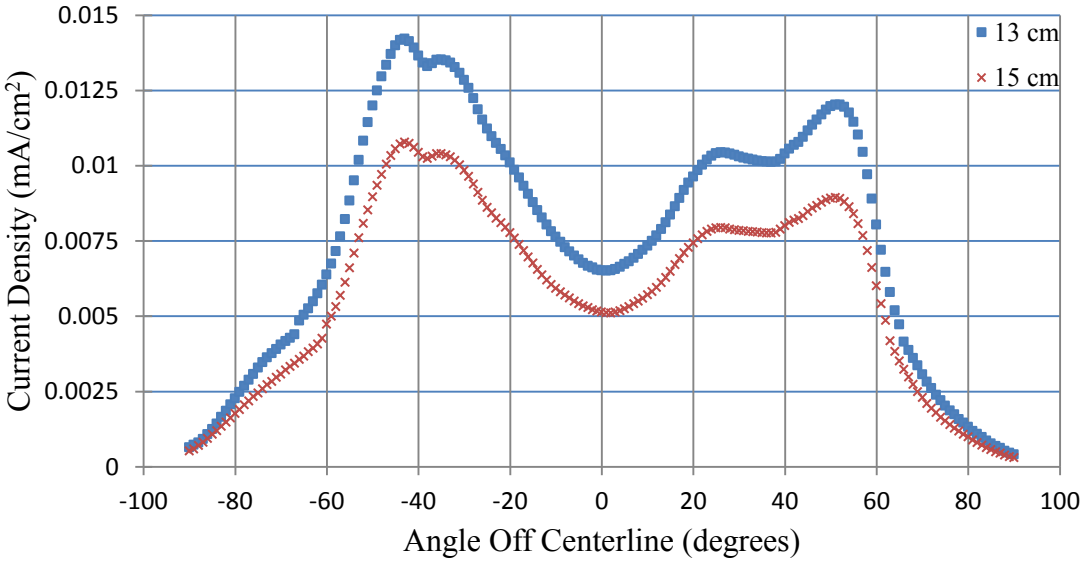

Figure 49. Current density curves for 2.5 W operating condition.

The channel size and SmCo magnet were originally selected based on a 20 W operating condition, so it was anticipated that the derived performance parameters would peak around that operating condition. However, it was found that the only performance parameter that was optimal at 20 W was the thrust asymmetry term, which reached a minimum value of 0.3%. That was roughly one tenth the degree of asymmetry found for the 2.5 W operating case. Unfortunately, the beam efficiency and divergence angle were only marginally better than the 13.6 W case, but worse than all others. The results are

provided in Table 10 and Figure 50. The current density distribution was similar to the shape observed at 13.7 W, but the distribution appeared to broaden and a double peak manifested itself on both sides of the 20 W case. It was observed during testing of the extreme cases that it was possible to get the thruster to operate in an additional—more diffuse—mode, so the performance associated with the new mode was measured.

Table 10. Derived beam parameters for 20 W operating condition.

Vacuum (torr)	Radius (cm)	Power (W)	V_d (V)	I_d (mA)	I_b (mA)	η_b (%)	θ (deg)	F_a	SE (%)
1.00E-06	13	20.02	238.3	84	31.00	36.90	74.35	0.006	0.26
1.00E-06	15	20.02	238.3	84	30.90	36.79	74.64	0.003	1.22

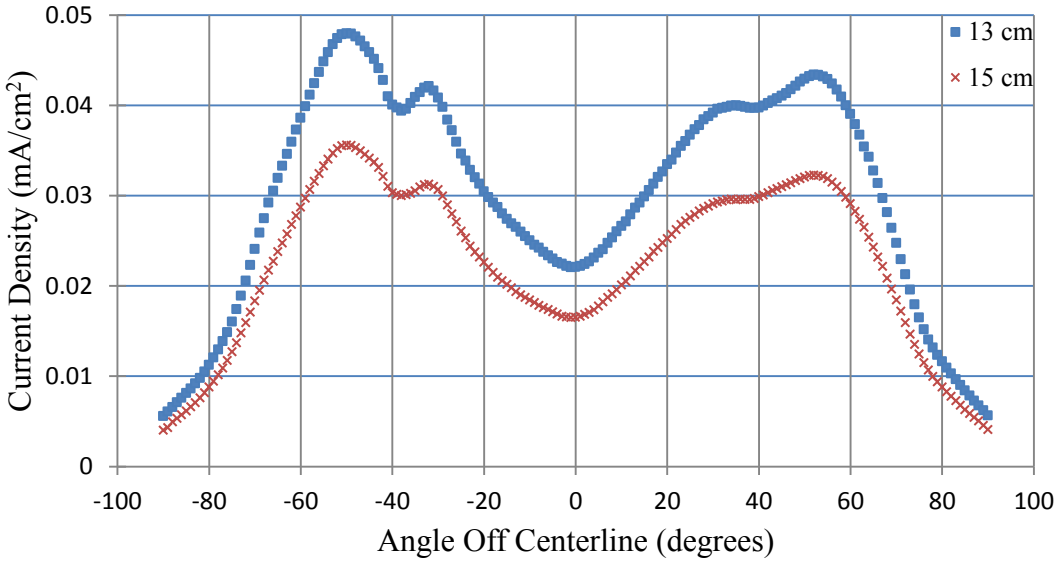

Figure 50. Current density curves for 20 W operating condition.

Comparison of Plume Modes

During testing the author discovered it was possible, with careful control of the anode flow rate, to settle the thruster to the same discharge power level with different mass flow rates through the anode. This was generally achieved after thruster startup by

setting the discharge voltage to a desired level and then crashing the mass flow rate from 1 sccm to a flow rate slightly below that which was generally necessary to achieve a desired discharge current when incrementally decreasing the flow rate. In all of the 4.7 W cases that were detailed above, the mass flow rate was approximately 0.45 sccm. The derived values detailed in Table 11 and Figure 51 were for a 4.7 W operating condition where the anode flow rate was only 4 sccm.

Table 11. Derived beam parameters for 4.7 W operating condition with reduced anode mass flow rate.

Vacuum (torr)	Radius (cm)	Power (W)	V_d (V)	I_d (mA)	I_b (mA)	η_b (%)	θ (deg)	F_a	SE (%)
9.42E-07	13	4.72	168.7	28	6.91	24.66	80.90	0.053	0.18
9.42E-07	15	4.72	168.7	28	6.78	24.23	80.71	0.057	0.26

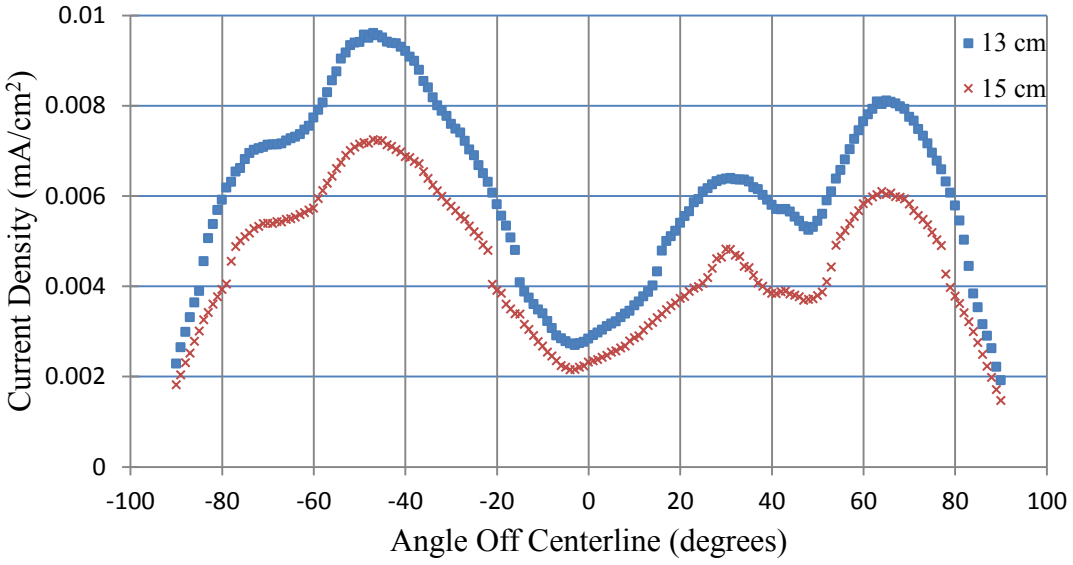

Figure 51. Current density curves for 4.7 W operating condition with reduced anode mass flow rate.

The ability to achieve the same discharge power with a lower mass flow rate is always desirable, but in this case, the cost of reducing the flow rate was significant

degradation of the other performance measures. The shape of the current density plot revealed significantly reduced peak currents when compared to higher flow rate cases and the centerline value was reduced to the level of the extreme wings. The result of the reduction in measured current density was a significantly lower estimate for the total beam current. In-turn, this reduced the beam current efficiency by approximately 40% when compared to the higher flow cases. The other significant attribute was a broadening of the plasma plume, which was illustrated by the largest divergence angle measured for any test case. This test concluded the Faraday analysis performed on the thruster.

Thrust Measurement

Measurement of the thrust produced by the BHT-20 was especially challenging due to the relatively low magnitude of the force generated by the thruster when operating over a range of 2.8 to 21.9 W. An attempt was made to measure thrust with the inverted pendulum stand detailed above, but the noise inherent in the instrument simply dwarfed the signal. This necessitated reconfiguring the chamber to accept the torsion balance, which proved to be the ideal instrument for this application. Four different successful test cases were conducted and their results summarized.

The first experiment performed with the torsion balance involved conducting 14 calibration runs with the cathode on and the thruster off. The cathode was left on to ensure that its operation did not influence the linearity assumption for the LDS response to a change in force. The 14 cases consisted of two runs at seven different calibration force conditions. The seven cases were produced by setting the electric potential between

the calibration electrodes values of 200 to 800 V, in 100 V increments. When plotted, the result was a curve of LDS voltage change as a function of applied calibration force, as depicted in Figure 52. The curve that resulted had a least squares regression value of 0.9996 and spanned beyond the range of measured thrust values for the BHT-20, which provided positive validation of resolution and linearity of torsion balance. Therefore, it was decided that thrust testing could commence with the torsion balance.

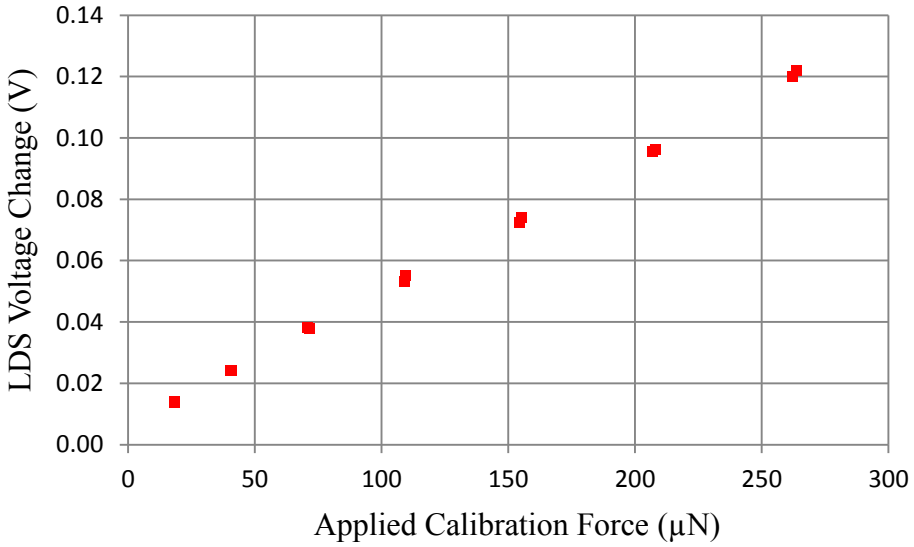

Figure 52. LDS voltage change as a function of applied calibration force.

The results provided in this section disregarded the mass flow rate associated with the BHC-1500 cathode, because a much different cathode would be paired with the BHT-20 for operational applications. Therefore, the value for I_{sp} included below is systematically higher than was actually observed during this research effort, but it serves to provide a reasonable estimate for the I_{sp} that would result if the thruster were paired with a thermionic cathode. Results from all previous attempts to scale down Hall thrusters to low power levels suggested that efficiency would decrease nonlinearly, so it

was not surprising that thrust data from the BHT-20 validated that general rule, as shown in Table 12.

Table 12. BHT-20 measured thrust and derived values using the torsion balance.

Anode Potential (V)	Anode Current (A)	Power (W)	Mass Flow (μg/s)	Thrust (μN)	Error (%)	η_a (%)	I_{sp} (s)
148.73	0.019	2.83	44.24	44	3.22	0.76	100.72
168.62	0.028	4.72	44.24	75	2.23	1.36	173.58
178.56	0.120	21.43	60.95	170	1.00	1.23	299.42
238.50	0.092	21.94	49.15	181	3.77	1.52	375.27

The anode efficiencies reported for the BHT-20 are lower than desirable and suggest further optimization is necessary prior to operational use. Nonetheless, the I_{sp} values do offer some promise that with optimization the thruster could be a viable contender for some missions. It was noteworthy that the highest I_{sp} was achieved at the highest discharge voltage, which is consistent with electrostatic thruster theory. Circular Hall effect thrusters also tend to perform better at relatively high discharge voltages, often above 300 V, so this suggests further testing should be performed at higher voltages.

Impact of Cathode on Performance

The results provided in Table 13 illustrate why it would not be reasonable to pair the BHT-20 with a cathode that was originally designed to be paired with a 1500 W annular Hall effect thruster. In several cases the required xenon flow rate for the cathode was more than twice the flow being used by the anode to generate ions, which is evidenced by the cathode efficiency values, η_c. Accounting for the total mass flow means that the actual Isp values were 31.26, 52.08, 114.59, and 125.09 s for the 2.83, 4.72,

21.43, and 21.94 W operating cases, respectively. To make matters worse, the electrical efficiency, η_o, was also extremely poor due to the amount of power required by the cathode. These two factors were compounded when the total efficiency, η_T, was calculated.

Table 13. BHT-20 measured thrust and derived values using the torsion balance.

Keeper Potential (V)	Keeper Current (A)	Cathode Power (W)	Discharge Power (W)	Cathode Mass Flow (μg/s)	Anode Mass Flow (μg/s)	η_c (%)	η_o (%)	η_T (%)
21.5	0.6	12.90	2.83	98.30	44.24	31.04	17.97	0.04
21.3	0.6	12.78	4.72	98.30	44.24	31.04	26.98	0.11
20.5	0.6	12.29	21.43	98.30	60.95	38.27	63.55	0.27
20.2	0.6	12.13	21.94	98.30	49.15	33.33	64.40	0.33

Findings

The BHT-20 represented a step forward in the ability to operate electrostatic thrusters at very low discharge powers. The thruster was found to have many stable operating points over the range of 2.5 to 25 W, and no degradation in the thruster was observed while operating at those power levels. However, operation at 45 W caused rapid erosion of the anode post, so the remainder of tests focused on operating points in the 2.5 to 20 W region. Plume sweeps conducted with a Faraday probe revealed that the thruster shares many attributes with small permanent magnet circular Hall thruster designs. The plume shape exhibited a characteristic halo distribution with a relatively broad divergence angle when compared with efficient annular Hall thruster designs. It was also note that at certain operating points the distribution of the ions was quite asymmetric, which is not a desirable attribute, but it could likely be curtailed with magnetic shunting, as described in chapter 5. It was observed that variation of the

cathode position over a narrow range caused changes in the current density distribution profile and divergence angle, but did not significantly impact any other performance measures. Thrust measurements revealed that the BHT-20 had a lower I_{sp} and total efficiency than the preponderance of Hall thruster designs previously employed; however, to a degree this was expected based on empirical results with scaling Hall thrusters to low power. Of course, the observed values were significantly influenced by the use of an unnecessarily large and power hungry cathode for this application.

V. Conclusions and Recommendations

This chapter presents preliminary findings based on this body of work. Conclusions regarding the BHT-20's performance are put forth and recommendations for further work with this thruster are provided. Possible avenues for further improvement of the thruster and test instruments are suggested. The BHT-20 was both a prototype and a novel departure from previous Hall effect thruster design, so a broad range of questions remain to be answered by future efforts.

Nonetheless, all of the initial objectives of this research effort were met. The BHT-20 was operated at discharge powers ranging from 2.5 to 20 W. Operating procedures and integration challenges were identified, viable solutions implemented, and documentation generated for future efforts. Voltage-current curves were produced at five flow rates and stable operating points identified for investigation with the techniques previously described. Faraday measurements were performed and the associated derivative values reported. The ion current density profiles revealed the thruster behaved like a permanent magnet circular Hall thruster in terms of plot shape and calculated divergence angle. Thrust was measured at four operating points, and this was used to generate values for I_{sp} and efficiency. The values produced by this analysis were lower than associated with nearly all Hall effect thrusters designed to operate at 20 to 100 W, but the measured values do suggest that further investigation is warranted for CubeSat applications where most current electric thrusters are simply too power hungry to be viable.

Voltage Current Curve Implications

The voltage-current curves generated as part of this research effort provide a useful tool for further investigations, but it is recommended that additional data be gathered to resolve some of the peculiarities presented in this study. The development of complete VI curves was complicated by the fact that anode post was found to rapidly degrade when operated near 40 W. No current limited mode was identified for the thruster at any flow rates, because the author did not desire to push the thruster above its 20 W design point and kept too relatively conservative discharge voltages. In retrospect, the similarities exhibited between the operation of the BHT-20 and a circular Hall thruster suggest that the thruster may have performed better at higher discharge voltages. For this reason it is suggested that at low flow rates, which do not result in the thruster exceeding 25 W, the VI curves be expanded by including discharge voltages up to 400 V.

The second part of the VI curves that deserve more study are the unstable operating points. Data acquisition software should be used to capture the anode current fluctuations at those operating points. The author suggests initially starting with a 100 Hz sampling rate, which would enable the experimenter to study behavior occurring at below 50 Hz according to Nyquist criterion. It is proposed the instability may be a result of high frequency breathing modes, but further investigation will be required to test this hypothesis.

BHT-20 Thruster

This thruster represents the first Hall effect variant to successfully operate in the 2.5-5 W range. The fact the thruster will operate stably and without apparent degradation

over a range that spans 2.5 to 25 W is no less significant. The efficiencies and I_{sp} values achieved over this range are lower than would warrant immediate integration onto any operational system, but with further refinement it is possible that this thruster design will evolve into a viable propulsion source for very small power limited satellites. Unless substantial improvements to all of the performance parameters are made then it is not suggested that this design be considered as a viable alternative in the 10+ W category due to the wide availability of competitive alternatives. Thus, one logical next-step would be to refine the understanding of this technology through the formulation and execution of a design of experiments aimed at better characterizing the current performance envelope of this design.

The performance characterization in this effort explored the results for a wide range of operating conditions, but it was not a parametric study intended to identify optimal operating points in terms of I_{sp}, thrust, or efficiency. It is likely that with further investigation operating points could be identified that exceed the best performance results found in this study. Nonetheless, it is suggested that such an effort be limited to low power points in order to reduce the trade-space and focus the study where this thruster design holds the possibility to mature into a viable operational technology. It is suggested that before such an effort is undertaken a better suited cathode be paired with the BHT-20.

The impact of the BHC-1500 cathode on the total efficiency and I_{sp} values found in this study reveal that the only way this thruster would be of any operational value is if it were paired with a thermionic cathode. HeatWave Labs, Inc. is currently the author's leading candidate to supply such a device, but other manufacturers, such as Kymball

Physics and Heat Wave Labs, Inc., also make single crystal emitters that are large enough to generate an electron current of greater than 30 mA. It is known that pairing a single crystal LaB_6 would cause nearly all of the performance measurements in this study to change, but it is not currently possible to accurately predict exactly how these measures would change due to a lack of prior work in this area. It is known that the elimination of the 1 sccm of xenon that was supplied to the cathode would yield significant improvements in the I_{sp}, cahode efficiency, and total efficiency terms. It is also known that the power required to operate an appropriately sized single crystal emitter will be lower, so nearly all of the performance numbers are expected to improve. This, coupled with the BHT-20's ability to operate at discharge power levels below any previous Hall thruster design provides a compelling argument to pursue further experimentation.

One of the most exciting discoveries that occurred while operating the BHT-20 was its ability to function stably at discharge powers down to 2.5 W. This suggests it would be possible, when paired with a thermionic cathode, to serve as a propulsion system on a 3U CubeSat. The electrical efficiency is concerning, because it suggests a significant percentage of the applied power is going to loss mechanisms, some of which are producing heating that may be difficult to manage on a CubeSat. If possible, design variations should be pursued that aim to improve the electrical efficiency of this thruster, but an increase in the I_{sp} would likely be seen as an even more important area of focus. Small satellites must be good stewards of their available power, but at least the power comes from an external source. The I_{sp} relates how effectively the propellant that is brought with the satellite is being used to produce a momentum exchange. The latter is an area where future evolutions of this design could potentially compete effectively against

the current competition in the 5 W thruster class. A continuous operating power of 5W is deemed reasonable for integration onto current CubeSats, because AFIT is currently preparing to launch a CubeSat with a 20 W average orbital power that is generated via a deployable seven-panel solar array.

The BHT-20 is rife with possible areas for experimentation. Increasing the magnetic field strength, altering the frit design, and resizing the thruster channel around operation at 5 W–instead of 20 W–all hold promise. The wide range of suggestions is possible, in part, due to the relatively simple and inexpensive design of the BHT-20. For comparison, this thruster could be modified to become a circular Hall thruster with the integration of a magnet in place of the BN anode post at the center of the discharge channel. Of course, this suggestion would only make sense if the additional magnet could be maintained at temperatures well below its Curie temperature. Alternatively, this magnet could be integrated into the center of the anode, below the anode post, where it might be better protected from the thermal environment, but would still provide an appreciable radial component to the magnetic field lines within the thruster channel. This would enable the thruster to generate a magnetic trap via the electron gyration radius that is expected to increase the ionization efficiency of the thruster. One immediate suggestion to improve the current design is to shunt the magnetic field lines outside of the channel exit, because this has been shown to eliminate the halo plume associated with permanent magnet circular Hall thruster designs [51]. In-turn, one could reasonably expect an improvement in the thrust factor and thrust asymmetry factor associated with the current design. The latter could be verified with additional Faraday sweeps.

Faraday Probe

The Faraday probe provided useful and repeatable measurements that were fundamental in establishing a preliminary theory for how the BHT-20 functioned. One of the important insights provided by Faraday probe measurements was the asymmetry typically associated with most operating points. However, the F_a term was derived based on measurements from a single plane passing through the centerline of the thruster, and measurements performed along two different planes displayed different F_a values, as was expected. It is suggested a rotisserie be constructed which could rotate the thruster about its centerline without the need to open the chamber between measurements. This would enable the rapid generation of a three-dimensional estimate for F_a. Ultimately, this could be used to predict the magnitude and direction of the actual thrust asymmetry inherent in this design. Similarly, the other instruments used in this characterization would also benefit from some minor modifications.

Inverted Pendulum Thrust Stand

The inverted pendulum thrust stand proved to be a reliable instrument, but the author suggests that its use be limited to the measurement of thrust levels above 2 mN in order to achieve a reasonable signal to noise ratio. One suggested improvement for the current thrust stand configuration is the integration of a higher flow water pump in order to keep the heat rejection rate constant; the current setup was unable to keep a constant flow rate over the timespan necessary to complete a single calibration run. Another suggestion for future researchers is to use the HD webcam in the chamber to view the calibration weight placement in order to ensure repeatable calibration curves. The author

had improved success with the introduction of the latter technique. However, the author does not feel any improvements to the inverted pendulum stand would make it a viable alternative to the torsion balance for the direct measurement of the thrust output of the BHT-20.

Torsion Balance

The torsion balance proved to be the ideal tool for measuring the relatively low thrust levels associated with the BHT-20. The results were repeatable and the associated error was very low considering the associated signal. Nonetheless, a couple of minor changes could dramatically improve the user experience. Surfaces within large vacuum chambers can change orientation slightly after the chamber achieves its operating pressure and thousands of pounds of force are exerted against its external structure. This behavior was observed with the inverted pendulum stand via its inclinometer. Such a device could easily be integrated onto the torsion stand. Of course, in order for such a tool to be useful the two level adjustment micrometers on the torsion balance would need to have externally controlled stepper motors attached to them. Along the same line, it would also be very useful to attach similar stepper motors to the LDS and calibration electrode micrometer translation stages. Future testing of the BHT-20 at AFIT will undoubtedly involve the inverted pendulum stand, but some additional instruments should also be considered.

Other Diagnostic Techniques

This study was limited in scope to the use of a Faraday probe and torsion balance, but other tools would be required in order to validate the life expectancy of the BHT-20

and to develop a better understanding of how it operates. The author believes one pressing study that remains is the thermal characterization of this thruster. It is speculated that thermal heating is not an issue for this thruster due to the fact that no discernable change in magnetic field strength occurred after more than 70 hours of testing, but this fact would need to be verified prior to a long endurance space mission. Further, it would be desirable to identify the steady state temperature of the anode in order to determine if this design could be morphed into a circular or end Hall thruster design without special cooling requirements. Laser induced fluorescence is another technique that could be used to validate the operating assumptions surrounding how this thruster generates plasma and where the ion acceleration occurs. The theory underlying both of these techniques is included in Appendix D.

Appendix A. BHT-20 Operating Procedures

The following procedures were used for the operation of the BHT-20 plasma thruster and the BHC-1500 cathode being used with it. Please see operating manuals on SPASS laboratory computers for instructions on how to operate various test instruments identified in Capt de La Harpe's thesis.

1. Ensure vacuum chamber pressure is below $5 \cdot 10^{-7}$ torr.
2. Purge xenon propellant lines;
    a. Open xenon gas bottle valve.
    b. Set propellant regulator valve to 20 psi.
    c. Turn on MKS four-channel readout.
    d. Set flow controllers for anode and cathode to 1 sccm.
    e. Open propellant Swagelok valves (if applicable).
    f. Allow propellant to flow for 30 minutes.
    g. Secure flow controllers.
3. Condition Cathode
    a. If the cathode has been exposed to ambient atmospheric conditions for a considerable amount of time (>4 days), then set flow controller for cathode to 0.5 sccm during conditioning process. Otherwise no flow.
    b. Turn on the PPU power supply and cooling fan.
    c. Start BPU-600 LabView program.
    d. Set heater current to 2 A for 90 minutes.
    e. Increase heater current to 4 A for 90 minutes.
    f. Increase heater current to 6 A for 30 minutes.

g. Turn off heater current.

4. Prepare Propellant Lines
    a. Open mass flow controller to cathode and set to a flow rate of 1 sccm.

5. Light Cathode
    a. Set cathode heater current to 6.5 A until breakdown voltage reaches 5.9 V (~10 minutes).
    b. Set cathode keeper current to 0.6 A.
        i. Cathode ignition is indicated by a drop in keeper voltage.
        ii. If keeper voltage remains above 100 V, cathode failed to break down. Repeat from step 5.
    c. Secure cathode heater: set cathode heater to 0 A.

6. Light Thruster
    a. Set anode mass flow controller to 1 sccm.
    b. Set discharge voltage to 170 V.
        i. Blue glow discharges at the anode face indicates the thruster is lit.
        ii. If thruster fails to light then confirm that cathode is lit and reattempt step 6.

7. Set to desired discharge power.
    a. Use voltage current curves from Capt de La Harpe's Master's thesis to identify desired operating point based on discharge voltage and discharge current.

b. Reduce anode flow rate to the flow rate associated with the desired operating point. This should be done within 20 seconds of lighting thruster in order to ensure thruster does not dwell at power level above 25 W.

c. Set discharge voltage to desired value

    i. Allow current to decrease from starting value and stabilize before adjusting discharge voltage.

    ii. Move discharge voltage to desired value in 10 V incriments.

d. Adjust anode flow rate until desired discharge current is achieved.

8. Allow thruster to stabilize and conduct testing. Ensure chamber pressure remains below ~$1x10^{-5}$ torr.

9. Securing Thruster

    a. Secure power to the anode and keeper.

    b. Secure xenon flow to the anode and cathode.

    c. Close propellant Swagelok valves (if applicable).

    d. Close xenon bottle valve.

    e. Close Host Simulator software and secure power to the PPU.

    f. Turn off PPU cooling fans after allowing PPU to cool for 10 minutes.

    g. Turn off all power supplies.

10. If restoring the vacuum chamber atmospheric pressure:

    a. Ensure the cathode has had at least 60 minutes to cool after operation.

    b. Push red button on vacuum control panel.

c. Fill chamber with dry nitrogen once cryo-pumps have ceased operation. Ensure that chamber door clamps are not secured tightly to avoid creation of pressure vessel.

Appendix B. BHT-20 Plume Pictures at Increasing Discharge Voltages.

A series of photos are presented that illustrate how the discharge plume changes as the discharge voltage is increased and the anode flow rate is held constant at 0.45 sccm xenon. The photos presented here are associated with voltages ranging from 158 to 238 V, in 10 V increments. A discussion of the trend across the entire voltage range is included in chapter 4, and additional insight into the phenomena visible in these images is provided by the analysis of Faraday data included in chapter 4. At a discharge voltage of 158 V the cathode discharge significantly obscures the typical blue illumination associated with ionized xenon. Close observation reveals a ball-like plume just protruding from the discharge channel where the ion density is sufficient to provide a nearly white illumination, as illustrated in Figure 53.

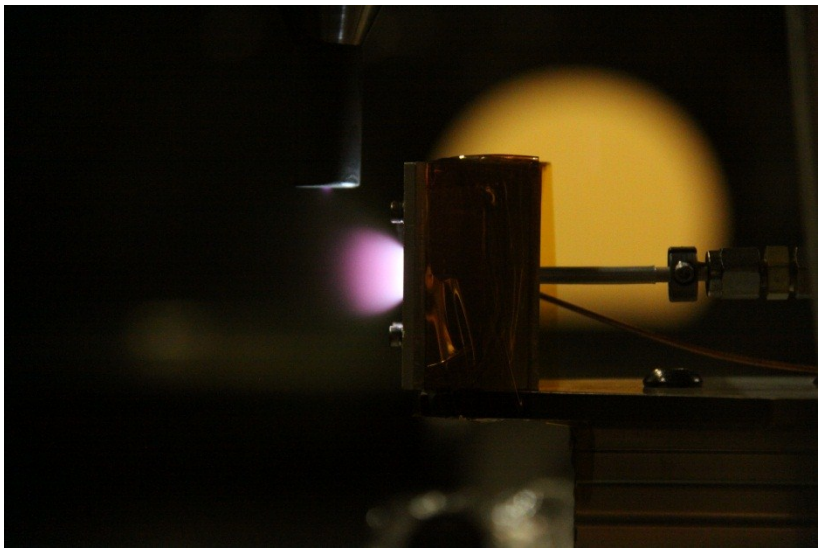

Figure 53. BHT-20 plume with V_d of 158 V and m_a of 0.45 sccm.

Increasing the discharge voltage to 168V does not substantially change the visible behavior illustrated above, but the central portion of the plume does become slightly more prominent, as shown in Figure 54.

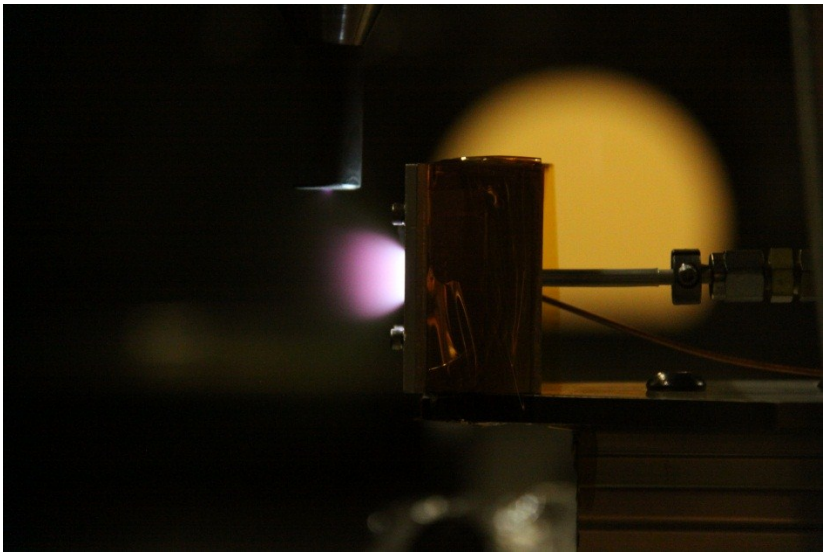

Figure 54. BHT-20 plume with V_d of 168 V and m_a of 0.45 sccm.

When the discharge voltage is increased to 178 V, the plume becomes incrementally more defined, as illustrated by Figure 55.

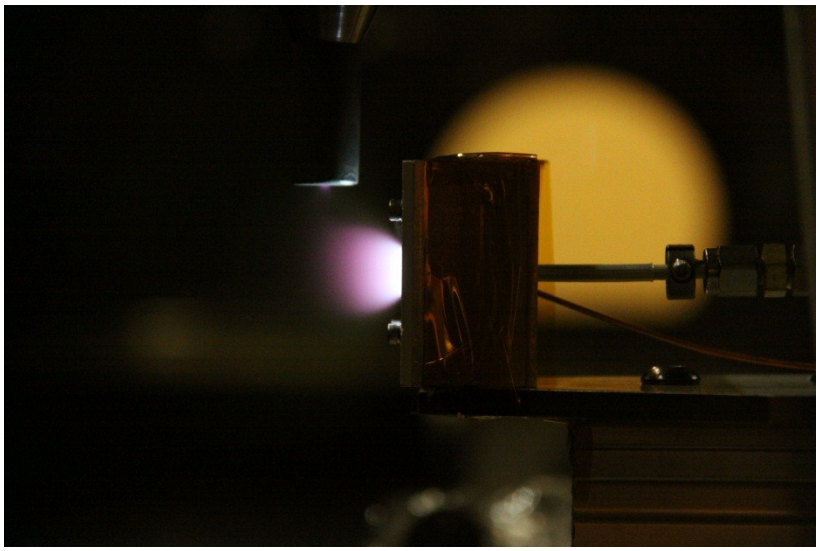

Figure 55. BHT-20 plume with V_d of 178 V and m_a of 0.45 sccm.

Again, increasing the discharge voltage to 188 V causes the high density discharge beam to become more distinctly differentiated from the cathode discharge, as depicted in Figure 56.

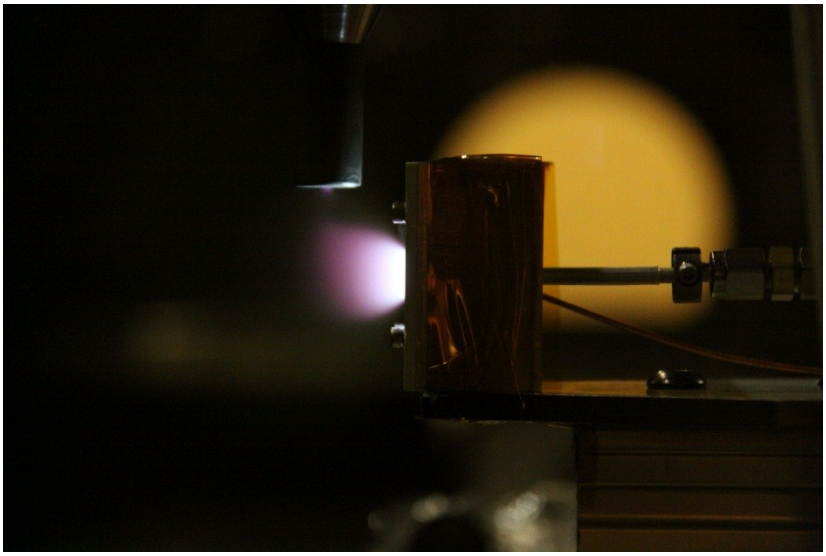

Figure 56. BHT-20 plume with V_d of 188 V and m_a of 0.45 sccm.

At a discharge voltage of 198 V, the ball-like nature of the plasma plume is readily apparent and relatively easy to differentiate from the cathode discharge, as illustrated by Figure 57. At this increment, the impact of the electric field lines on the cathode plume also becomes more pronounced.

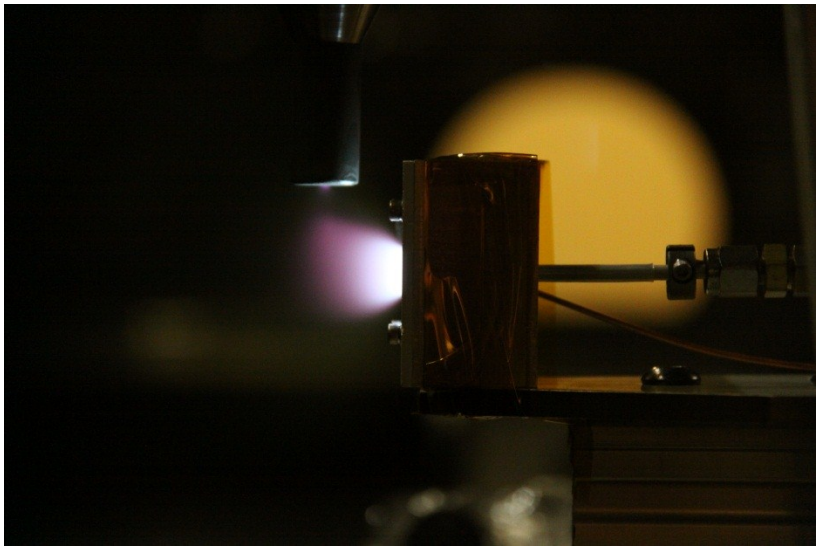

Figure 57. BHT-20 plume with V_d of 198 V and m_a of 0.45 sccm.

The general trend established above continues to hold with an increase in the discharge voltage to 208V, as shown in Figure 58.

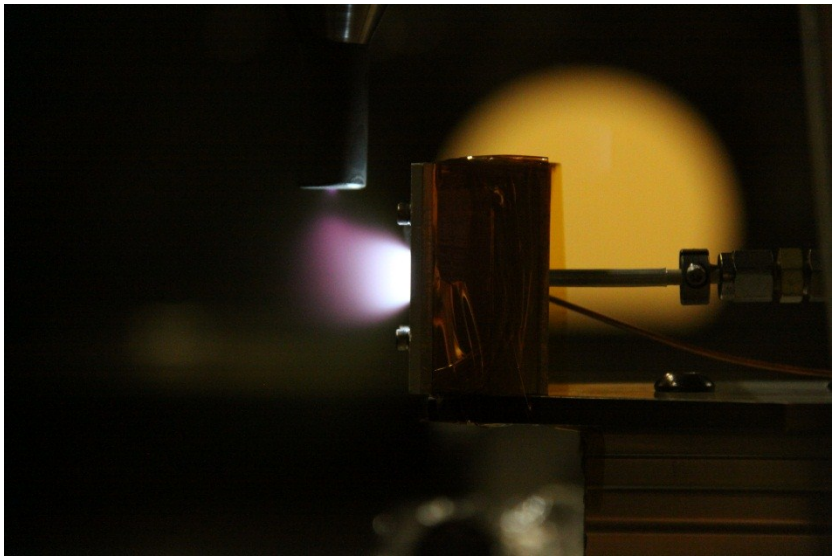

Figure 58. BHT-20 plume with V_d of 208 V and m_a of 0.45 sccm.

The established trend continues to hold with an increase in the discharge voltage to 218V, as shown in Figure 59.

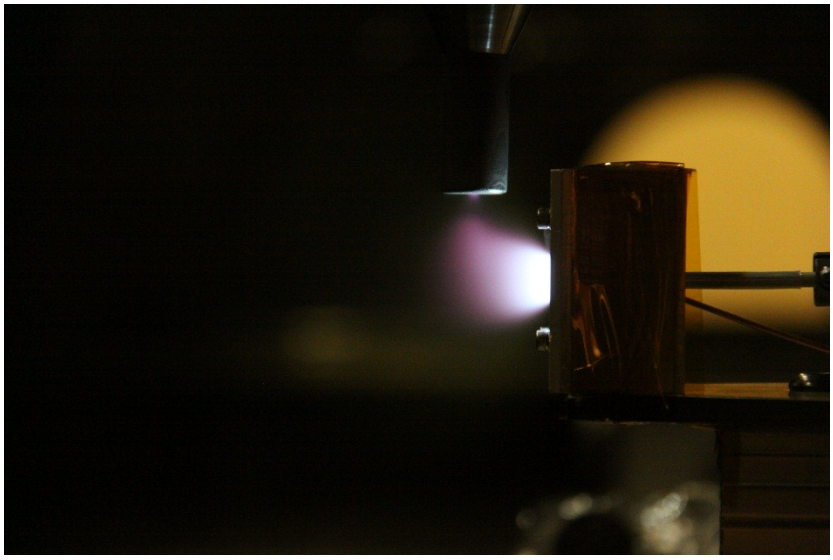

Figure 59. BHT-20 plume with V_d of 218 V and m_a of 0.45 sccm.

The established trend continues to hold with an increase in the discharge voltage to 228V, as shown in Figure 60.

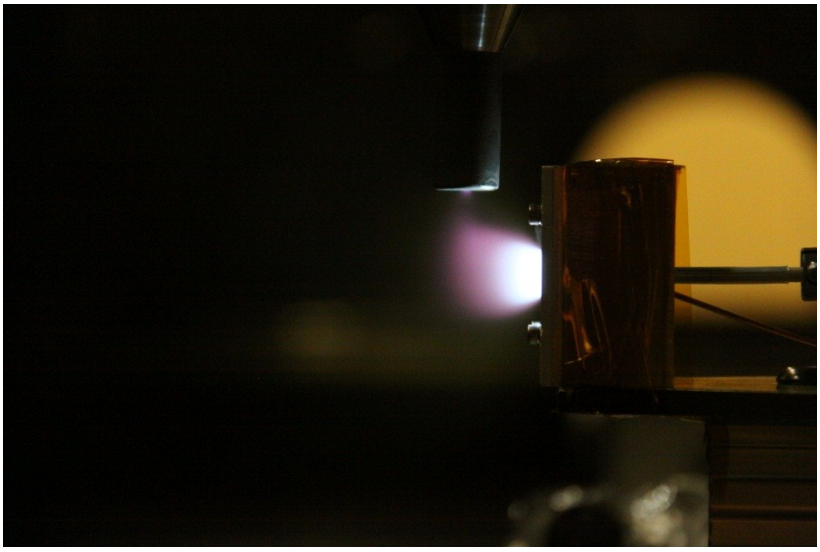

Figure 60. BHT-20 plume with V_d of 228 V and m_a of 0.45 sccm.

The established trend continues to hold with an increase in the discharge voltage to 238V, as shown in Figure 61. The luminosity produced by the central plume has increased substantially over the nine cases and the central plume is now easily distinguishable.

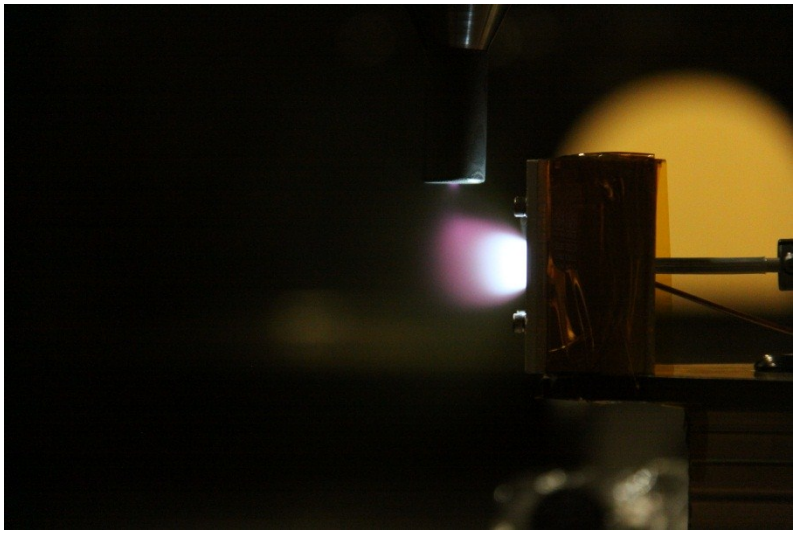

Figure 61. BHT-20 plume with V_d of 238 V and m_a of 0.45 sccm.

Appendix C. Faraday Probe Data

The data included in this section illustrates the impact of moving the cathode relative to the thruster. The cathode's position was varied relative to the thruster centerline and thruster face in 1 mm increments. Table 14 identifies the specific test cases included in this section. In all cases the anode mass flow rate was held constant. It was found that the shape of the current density plot and divergence angle were the only two derived performance measures that significantly changed. It was found that increasing the distance from the centerline consistently increased the divergence angle and decreasing the distance from the thruster face consistently increased the divergence angle.

Table 14. Test cases included in Appendix C.

Position	Figure Number	Table Number	Distance from Cathode to Thruster Centerline (cm)	Distance from Cathode to Thruster Face (cm)
A	62	15	1.59	1.59
B	63	16	1.59	1.39
C	64	17	1.59	1.49
D	65	18	1.59	1.69
E	66	19	1.59	1.79
F	67	20	1.69	1.59
G	68	21	1.79	1.59
H	69	22	1.89	1.59
I	70	23	1.99	1.59

Position A represents the baseline run, because it was performed with the cathode in the position specified by the manufacturer of the BHT-20. The plume shape revealed in Figure 62 aligns well with the expectations established after operating the thruster at numerous operating conditions. The beam efficiency, divergence angle, and thrust asymmetry factor reported in Table 15 also align well with the behavior reported in chapter 4.

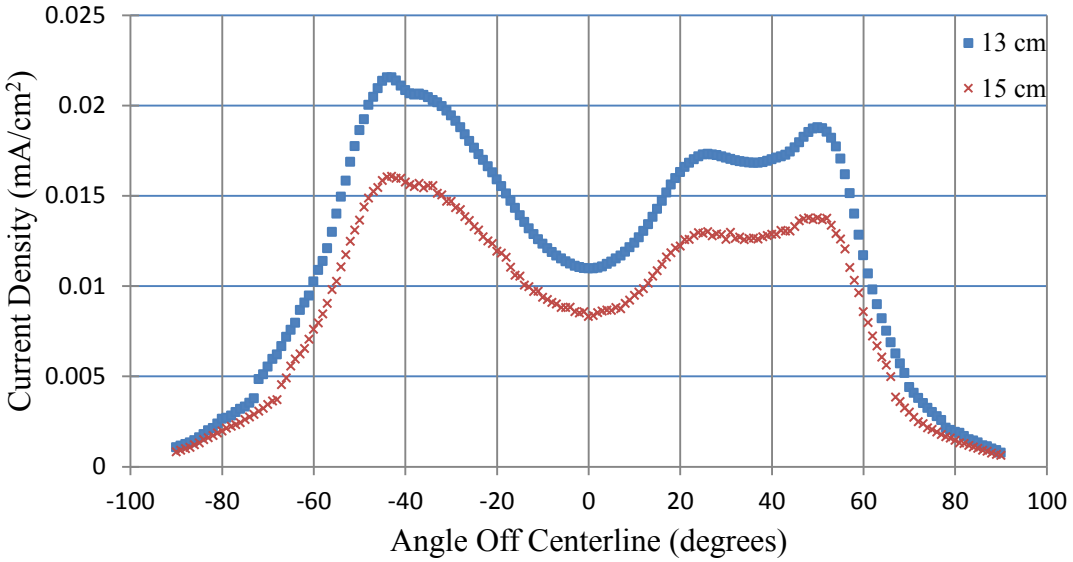

Figure 62. Current density curves for 4.7 W operating condition with cathode in position A.

Table 15. Derived beam parameters for 4.7 W operating condition with cathode in position A.

Vacuum (torr)	Radius (cm)	Power (W)	V_d (V)	I_d (mA)	I_b (mA)	η_b (%)	θ (deg)	F_a
9.40E-07	13	4.72	168.7	28	11.19	39.98	67.40	0.017
9.40E-07	15	4.72	168.7	28	11.06	39.49	66.49	0.013

The distance from the cathode to the thruster face was reduced by 2 mm for position B, relative to position A. The plume shape revealed in Figure 63 illustrates an appreciable decrease in the peak current density measurement and an appreciable broadening of the curve. These visual cues are substantiated by the results presented in Table 16, which reports that the divergence angle increased while the other figures of merit remained relatively constant.

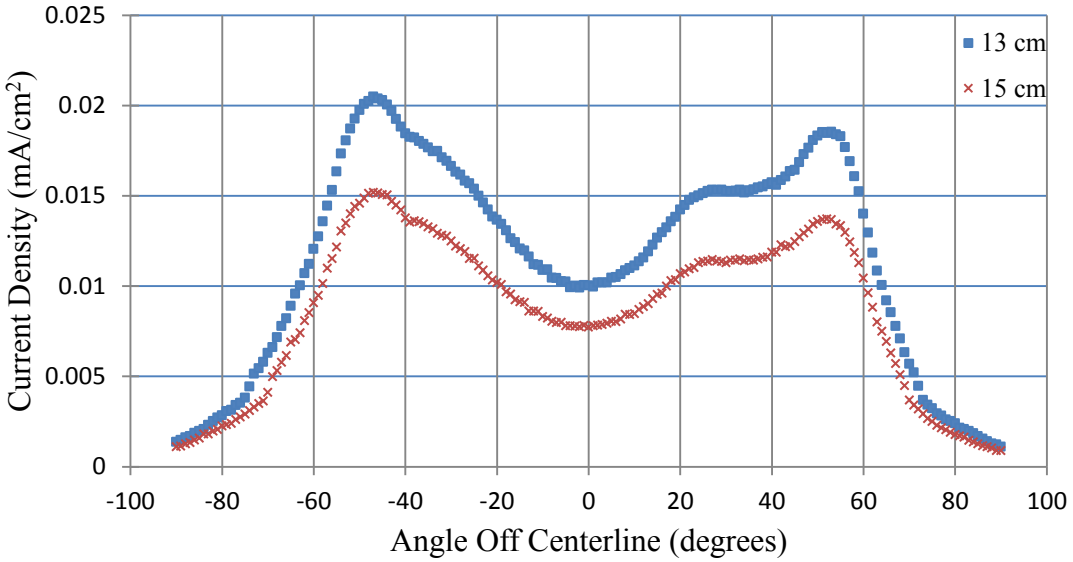

Figure 63. Current density curves for 4.7 W operating condition with cathode in position B.

Table 16. Derived beam parameters for 4.7 W operating condition with cathode in position B.

Vacuum (torr)	Radius (cm)	Power (W)	V_d (V)	I_d (mA)	I_b (mA)	η_b (%)	θ (deg)	F_a
9.09E-07	13	4.72	168.7	28	11.21	40.05	69.84	0.017
9.09E-07	15	4.72	168.7	28	11.13	39.76	69.53	0.012

The distance from the cathode to the thruster face was reduced by 1 mm for position C, relative to position A. The plume shape revealed in Figure 64 illustrates a slight decrease in the peak current density measurement and a slight broadening of the curve. These visual cues are substantiated by the results presented in Table 17, which reports that the divergence angle increased while the other figures of merit remained relatively constant, with respect to the baseline case. The divergence angle for position C was between those measured at position A and position B, so this serves to form the initial basis of a trend.

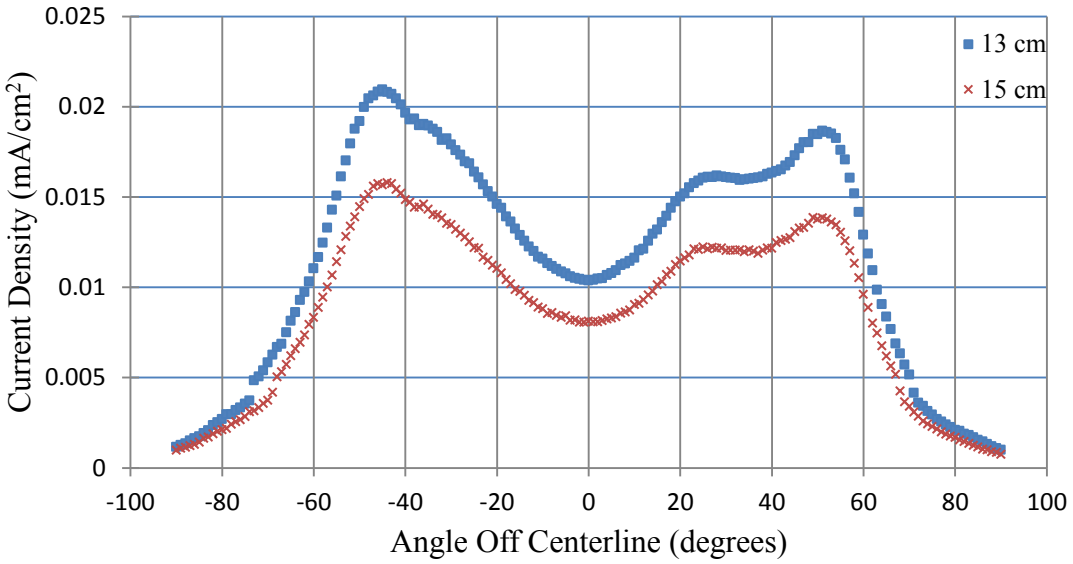

Figure 64. Current density curves for 4.7 W operating condition with cathode in position C

Table 17. Derived beam parameters for 4.7 W operating condition with cathode in position C.

Vacuum (torr)	Radius (cm)	Power (W)	V_d (V)	I_d (mA)	I_b (mA)	η_b (%)	θ (deg)	F_a
9.56E-07	13	4.72	168.7	28	11.17	39.88	69.00	0.017
9.56E-07	15	4.72	168.7	28	11.16	39.87	68.83	0.014

The distance from the cathode to the thruster face was increased by 1 mm for position D, relative to position A. The plume shape revealed in Figure 65 illustrates a slight increase in the peak current density measurement and a slight narrowing of the curve, relative to the baseline case. These visual cues are substantiated by the results presented in Table 18, which reports that the divergence angle decreased while the other figures of merit remained relatively constant, with respect to the baseline.

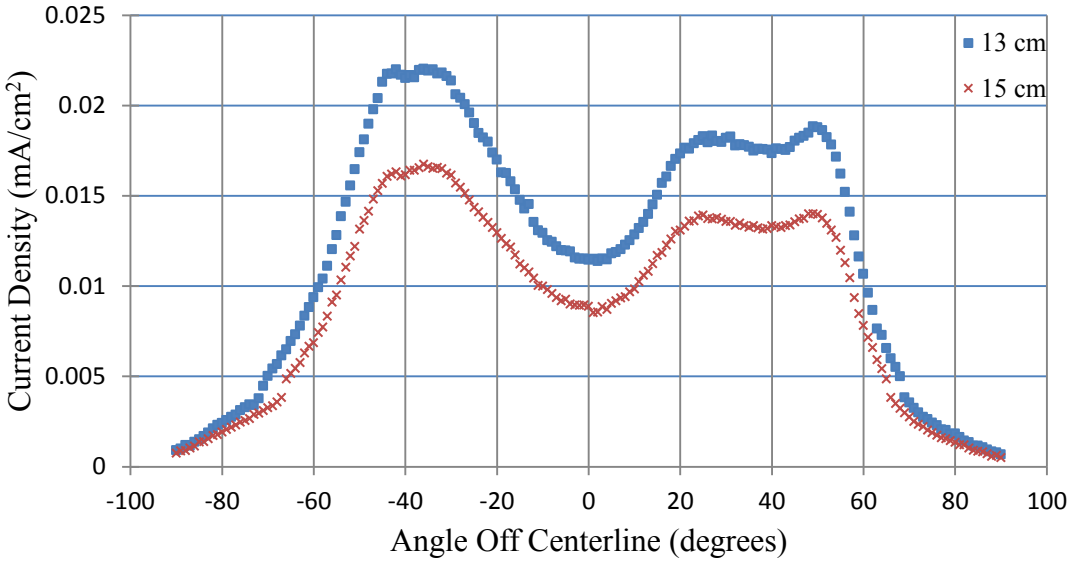

Figure 65. Current density curves for 4.7 W operating condition with cathode in position D.

Table 18. Derived beam parameters for 4.7 W operating condition with cathode in position D.

Vacuum (torr)	Radius (cm)	Power (W)	V_d (V)	I_d (mA)	I_b (mA)	η_b (%)	θ (deg)	F_a
9.73E-07	13	4.72	168.7	28	11.08	39.56	67.06	0.020
9.73E-07	15	4.72	168.7	28	11.07	39.53	66.83	0.015

The distance from the cathode to the thruster face was increased by 2 mm for position E, relative to position A. The plume shape revealed in Figure 66 illustrates an appreciable increase in the peak current density measurement and an appreciable narrowing of the curve, relative to the baseline case. These visual cues are substantiated by the results presented in Table 19, which reports that the divergence angle decreased while the other figures of merit remained relatively constant, with respect to the baseline. The results for divergence angle as a function of distance from the thruster face showed a consistent improvement, over the range tested, as the distance increased.

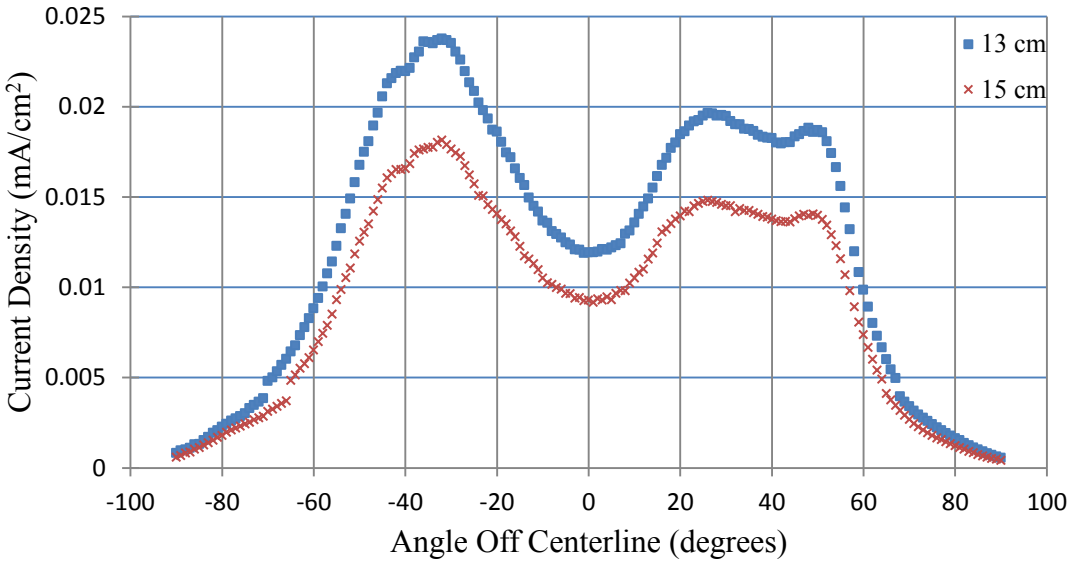

Figure 66. Current density curves for 4.7 W operating condition with cathode in position E.

Table 19. Derived beam parameters for 4.7 W operating condition with cathode in position E.

Vacuum (torr)	Radius (cm)	Power (W)	V_d (V)	I_d (mA)	I_b (mA)	η_b (%)	θ (deg)	F_a
9.39E-07	13	4.72	168.7	28	11.16	39.87	66.38	0.019
9.39E-07	15	4.72	168.7	28	11.17	39.90	65.94	0.012

The distance from the cathode to the thruster centerline was increased by 1 mm for position F, relative to position A. The plume shape revealed in Figure 67 illustrates a slight decrease in the peak current density measurement and a slight narrowing of the curve, relative to the baseline case. These visual cues are substantiated by the results presented in Table 20, which reports that the divergence angle increased while the other figures of merit remained relatively constant, with respect to the baseline.

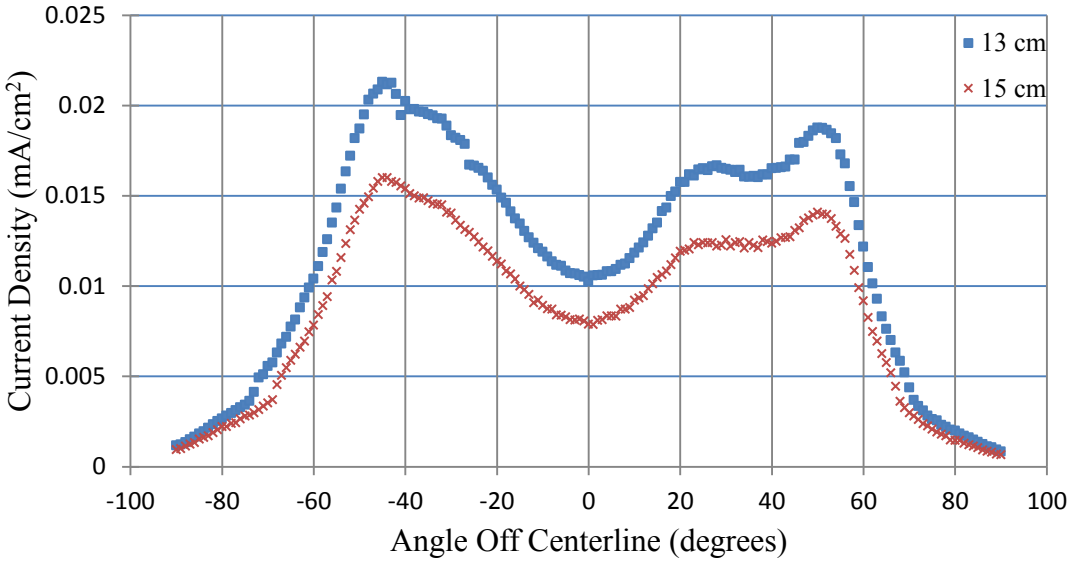

Figure 67. Current density curves for 4.7 W operating condition with cathode in position F.

Table 20. Derived beam parameters for 4.7 W operating condition with cathode in position F.

Vacuum (torr)	Radius (cm)	Power (W)	V_d (V)	I_d (mA)	I_b (mA)	η_b (%)	θ (deg)	F_a
9.33E-07	13	4.72	168.7	28	11.06	39.51	68.88	0.021
9.33E-07	15	4.72	168.7	28	11.08	39.56	68.51	0.017

The distance from the cathode to the thruster centerline was increased by 2 mm for position G, relative to position A. The plume shape revealed in Figure 68 illustrates an appreciable decrease in the peak current density measurement and an appreciable narrowing of the curve, relative to the baseline case. These visual cues are substantiated by the results presented in Table 21, which reports that the divergence angle increased while the other figures of merit remained relatively constant, with respect to the baseline.

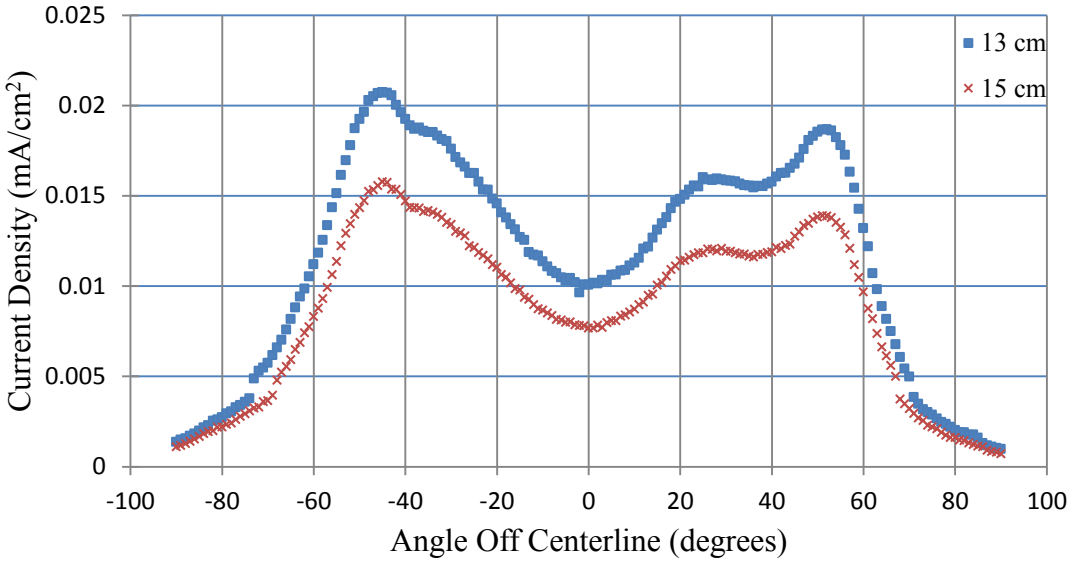

Figure 68. Current density curves for 4.7 W operating condition with cathode in position G.

Table 21. Derived beam parameters for 4.7 W operating condition with cathode in position G.

Vacuum (torr)	Radius (cm)	Power (W)	V_d (V)	I_d (mA)	I_b (mA)	η_b (%)	θ (deg)	F_a
9.42E-07	13	4.72	168.7	28	11.07	39.55	69.22	0.022
9.42E-07	15	4.72	168.7	28	11.06	39.51	68.99	0.019

The distance from the cathode to the thruster centerline was increased by 3 mm for position H, relative to position A. The plume shape revealed in Figure 69 illustrates an appreciable decrease in the peak current density measurement and an appreciable narrowing of the curve, relative to the baseline case. These visual cues are substantiated by the results presented in Table 22, which reports that the divergence angle increased while the other figures of merit remained relatively constant, with respect to the baseline.

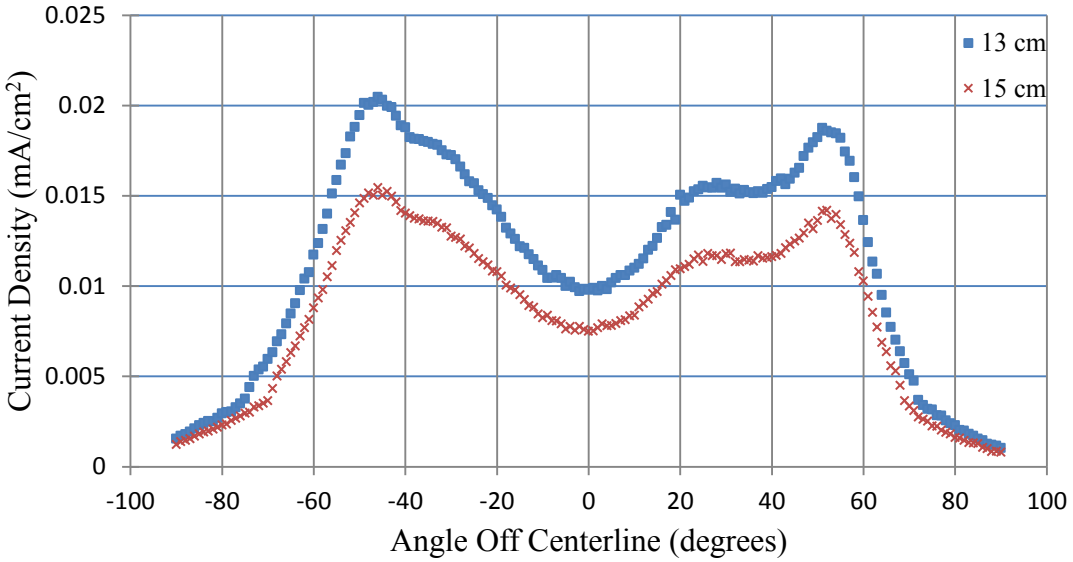

Figure 69. Current density curves for 4.7 W operating condition with cathode in position H.

Table 22. Derived beam parameters for 4.7 W operating condition with cathode in position H.

Vacuum (torr)	Radius (cm)	Power (W)	V_d (V)	I_d (mA)	I_b (mA)	η_b (%)	θ (deg)	F_a
9.70E-07	13	4.72	168.7	28	11.11	39.66	69.46	0.022
9.70E-07	15	4.72	168.7	28	11.07	39.55	69.04	0.017

The distance from the cathode to the thruster centerline was increased by 4 mm for position I, relative to position A. The plume shape revealed in Figure 70 illustrates an appreciable decrease in the peak current density measurement and an appreciable narrowing of the curve, relative to the baseline case. These visual cues are substantiated by the results presented in Table 23, which reports that the divergence angle increased while the other figures of merit remained relatively constant, with respect to the baseline. The results for divergence angle as a function of distance from the thruster centerline showed a consistent improvement, over the range tested, as the distance decreased.

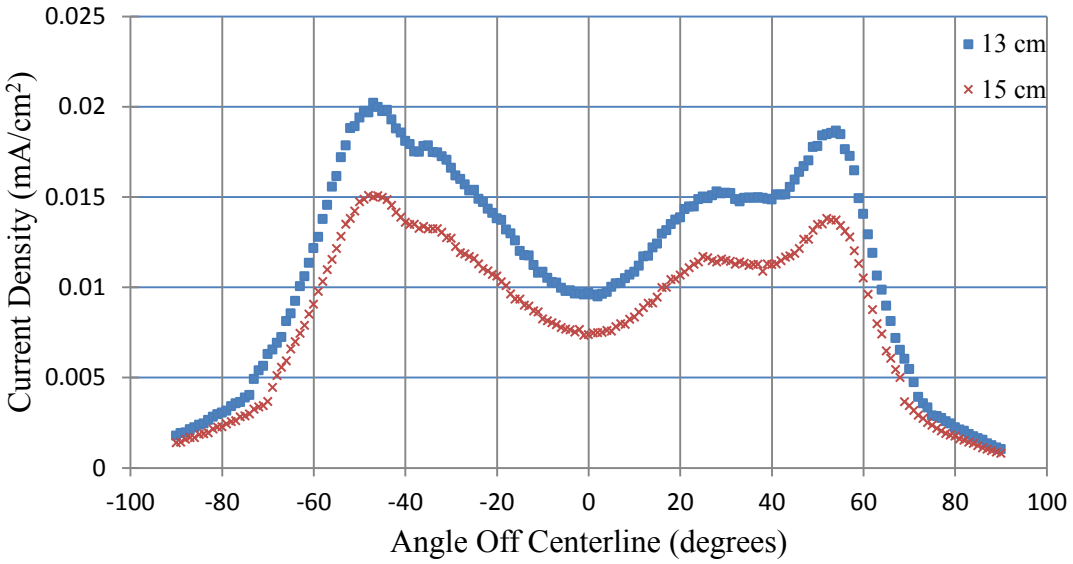

Figure 70. Current density curves for 4.7 W operating condition with cathode in position I.

Table 23. Derived beam parameters for 4.7 W operating condition with cathode in position I.

Vacuum (torr)	Radius (cm)	Power (W)	V_d (V)	I_d (mA)	I_b (mA)	η_b (%)	θ (deg)	F_a
9.44E-07	13	4.72	168.7	28	11.07	39.55	70.18	0.025
9.44E-07	15	4.72	168.7	28	11.03	39.40	69.40	0.019

Appendix D. Background and Theory of Further Diagnostic Techniques

Thermal Camera Background.

The next test suggested for the BHT-20 is thermal characterization using thermocouples and a FLIR camera. This test is necessary to ensure that the steady state operating temperature of the BHT-20 does not approach the Currie temperature of the SmCo permanent magnet being used in the design, because that would cause demagnetization that would degrade the thruster's performance. The infrared camera that is suggested is the ThermaCAM SC640, which has an operational range of -40°C to 1500°C with an accuracy of ±2% of reading [54]. This instrument is illustrated in Figure 71.

Figure 71. ThermaCAM SC640 Infrared Camera [54].

Thermal Camera Theory.

Matter above absolute zero emits electromagnetic radiation with wavelengths between 0.75 micrometers and 100 micrometers (infrared) that can be correlated to a surface temperature if the properties of the matter are known [4]. The ideal absorber and

emitter of radiation is a blackbody. The radiation emitted by a black body, $E_{\lambda,b}$, is idealized and can be represented as a function of wavelength and temperature.

$$E_{\lambda,b}(\lambda,T) = \frac{2\pi hc^2}{\lambda^5\left[e^{\left(\frac{hc}{\lambda kT}\right)}-1\right]} \tag{22}$$

T is the absolute temperature, h is Plank's constant, c is the speed of light, and k is Boltzmann's constant. Integrating this equation over all wavelengths produces the Stefan-Boltzmann Law for total blackbody power.

$$E_b = \int_0^\infty \frac{2\pi hc^2}{\lambda^5\left[e^{\left(\frac{hc}{\lambda kT}\right)}-1\right]} d\lambda = \sigma T^4 \tag{23}$$

σ is the Stephan-Bolzmann constant.

Kirchhoff's Law relates the emissivity of a surface to its absorptivity, where α is the ratio of spectral radiant power absorbed to incident power and ε is the emissivity.

$$\alpha_\lambda = \varepsilon_\lambda \tag{24}$$

These two equations can be combined to yield a relationship between the actual and measured temperature based on the optical characteristics of the test specimens [55].

$$T_{cam}^4 = \varepsilon\tau_{vp}T_{obj}^4 + (1-\varepsilon)\tau_{vp}T_{refl}^4 + \left(1-\tau_{vp}\right)T_{vp}^4 \tag{25}$$

T_{cam} refers to the blackbody temperature reported by the thermal camera, T_{obj} is the surface temperature of the specimen's surface, T_{refl} is the effective temperature or radiation incident on the surface, and T_{vp} is the temperature of the view port. The emissivity and transmissivity, τ, are a function of wavelength, temperature, and material. Emissivity is also function of the finish of the material, so published data for this value will need to be substantiated using an independent temperature measurement device, such a thermocouple.

Temperature measurements using the infrared camera will require special care. The quality of the data collected will be a product of alignment, view angle, and focus. Further, the vacuum chamber's viewport will need to be regularly polished in order to avoid increased thermal noise from deposits that will form on the window after thruster operation. Thermocouples will be used on external surfaces in order to have a source to substantiate the temperatures captured by the infrared camera.

Laser Absorption.

Initial visual observation of the micro-Hall thruster revealed that the greatest plasma luminescence was heavily concentrated toward to center of ionization channel. This observation should be verified using laser absorption. Laser absorption works based on the fundamental principle of spectroscopy that each ionization state for a given atom or molecule possesses unique spectral lines which represent the wavelength of light that the atom or molecule will absorb. The pattern of spectral lines observed for a specific element is related to the statistical distribution of the electrons for that element and the

associated quanta of energy, *ΔE,* that will cause one of the electrons to transition from one state, E_1, to another, E_2, which is described by (26) [56]:

$$\Delta E = E_2 - E_2 \tag{26}$$

The specific wavelengths of light that will be absorbed are related to the, *ΔE,* from (26) through the theory of wave-particle duality, which describes the energy a photon carries as a function of its energy level (E). Thus the wavelength that will cause a specific electron transition can be found using (27) where *h* is Plank's constant, *f* is the photon frequency, *c* is the speed of light and λ is the wavelength of the photon [56].

$$E = hf = \frac{hc}{\lambda} \tag{27}$$

The application of absorption to characterizing this electric thruster stems from the fact that it is possible to couple the properties above with some additional relationships in order to determine the number density of a specific atom within a given length. When a laser is emitting photons tightly distributed about the wavelength associated a strong spectral line is passed through a volume of gas that absorbs at that spectral line the result is a decrease in power, which can be modeled according to Beer's Law for absorption, which is given as (28) [56]. I_t is the beam intensity resulting from the energy lost to absorption, *l* is the length of the path through the volume of absorbing gas, N_i the number density of the atoms and σ_{abs} is the absorption cross-sectional area.

$$I_t = I_o e^{(-\sigma_{abs} l N_i)} \tag{28}$$

$$\sigma_{abs} = \frac{A_{21} c^2}{8\pi f^2} \frac{g_2}{g_1} \tag{29}$$

A_{21}, the Einstein spontaneous emission rate coefficient, and g_1 and g_2, which are degeneracy terms related to the transitioning level of the atom or molecule in question. The challenge is that one needs a reference for these values; however, the benefit is that one can solve (29) for number density, producing (30), in order to experimentally determine the concentration of a specific atom or molecule in a given volume by comparing the ratio of the laser reference intensity with the reduced intensity measured after the laser has passed through the gas of interest.

$$N_i = \frac{-ln\left(\frac{I_t}{I_0}\right)}{\sigma_{abs} l} \tag{30}$$

The absorption lines for the first three xenon ionization states are included in Appendix A. This study will focus on the identification of the first ionization state. The absorbance will measured by comparing the transmitted laser intensity to the etalon using a Matsui's methodology [57].

In order to take laser absorption measurements the baseline thruster design will need to be revised. Absorption measurements will require a focuses beam of laser light to pass uninterrupted through the xenon plasma within the ionization channel. The back plate of the thruster is currently opaque to infrared radiation, so the design and material selection for the back plate will need to be revised. The current proposed redesign would introduce the neutral xenon flow from the sides of the thruster and include cutouts in the back plate that would be sealed with a transparent diamond sheet in order to provide windows for laser transmission. The fabrication of this design will require additional investigation.

Bibliography

[1] J. R. Wertz and W. J. Larson, *Space Mission Analysis and Design*, 3rd ed. New York: Space Technology Library, 2008.

[2] R. W. Humble, G. N. Henry, and W. J. Larson, *Space Propulsion Analysis and Design*, 1st ed. New York: McGraw-Hill Companies, Inc., 1995.

[3] S. Paintal. (2010, May) Micro-Hall Thruster. Presentation.

[4] A. M. Bohnert, "Thermal Characterization of a Hall Effect Thruster," Air Force Institute of Technology, Dayton, OH, Master's Thesis AFIT/GA/ENY/08-M01, March 2008.

[5] J. Lui et al., "Thermal Stability and Radiation Resistance of Sm-Co Based Permanent Magnets," in *Proceedings of Space Nuclear Conference 2007*, Boston, MA, June 2007.

[6] D. J. Warner, "Advanced Cathodes for Next Generation Electric Propulsion Technology," Air Force Institute of Technology, Dayton, OH, Master's Thesis AFIT/GA/ENY/08-M07, 2007.

[7] R. G. Jahn, *Physics of Electric Propulsion*. Mineola, New York: Dover Publications, Inc., 1996.

[8] D. M. Goebel and I. Katz, *Fundamentals of Electric Propulstion: Ion and Hall Thrusters*. Hoboken, NJ: JPL Space Science and Technology Series, John Wiley & Sons, Inc., 2008.

[9] F. S. Gulczinski III and R. A. Spores, "Analysis of Hall-Effect Thrusters and Ion Engines for Orbit Transfer Missions," no. 32nd AIAA, ASME, SAE, and ASEE Joint Propulsion Conference and Exhibit, pp. 1-18, July 1996.

[10] W. A. Hargus Jr. et al, "Status of US Testing of the High Performance Hall System SPT-140 Hall Thruster," Propulsion Directorate, Edwards AFB, 1999.

[11] D. L. Brown et al., "Standardization of Hall Thruster Efficiency Analysis: Methodology and Historical Perspective," *Air Force Research Laboratory*, p. 27, Feb 2008.

[12] D. C. Byers and J. W. Dankanich, "In-space Propulsion Influences on COMSAT Missions," in *International Electric Propulsion Conference*, Florence, September 2007.

[13] E. J. Pencil, "Recent Electric Propulsion Development Activities for NASA Science Missions," January 2009.

[14] K. E. Witzberger and D. Manzella, "Performance of Solar Electric Powered Deep Space Mission Using Hall Thruster Propulsion," in *41st Joint Propulsion Conference and Exhibit*, Tucson, AZ, July Jul 2005.

[15] S. W. Kim and A. D. Gallimore, "Plume Study of a 1.35 kW SPT-100 Using an EXB Probe," *AIAA*, 1999.

[16] T. Ito et al., "Futher Development of a Micro Hall Thruster," vol. 42ng AIAA/ASME/SAE/ASEE Joint Propulsion Conference & Exhibit, July 2006.

[17] D. P. Schmidt, "A Low-power, Linear-geometry Hall Plasma Source with an Open Electron-drift," *Plasma Sources Sci. Technol.*, pp. 68-76, July 1999.

[18] O. A. Gorshkov, "Overview of Russian Activities in Electric Propulsion," no. 37th AIAA/ASME/SAE/ASEE Joint Propulsion Conference and Exhibit, July 2001.

[19] J. Mueller et al. (2008, April) A Survey of Micro-Thrust Propulsion Options for Microspacecraft and Formation Flying Missions. Presentation.

[20] T. Ito et al., "Ultra-Low Power Stationary Plasma Thruster," in *The 29th International Electric Propulsion Conference*, Princetron, NJ, Nov 2005.

[21] A. Smirnov, Y. Raites, and N. J. Fisch, "Plasma Measurments in a 100W Cylindrical Hall Thruster," in *39th AIAA/ASME/SAE/ASEE Joint Propulsion Conference and Exhibit*, Huntsville, AL, Jul 2003.

[22] NRO. (2011, February) NRO News. [Online]. http://www.nro.gov/PressReleases/stexpics.html

[23] ESA. (2011, February) ESA Images Multimedia Gallery. [Online]. http://www.esa.int/esa-mmg/mmg.pl?b=b&type=I&mission=SMART-

1&single=y&start=119

[24] W. A. Hargus Jr., "Investigation of the Plasma Aceleration Mechanism within a Coaxial Hall Thruster," Dept. of Mechanical Engineering, Stanford University, Stanford, CA, PhD Dissertation 2001.

[25] J. T. Yim and I. D. Boyd, "Hall Thruster Erosion Prediction Using a Hydrodynamic Plasma Model and Sputtering Simulation," in *30th International Electric Propulsion Conference*, Florence, September 2007.

[26] P. Y. Peterson and D. H. Manzella, "Investigation of the Erosion Characteristics of a Laboratory Hall Thruster," in *39th Joint Propulsion Conference and Exhibit*, Huntsville, July 2003.

[27] A. Kieckhafer and L. B. King, "Energetics of Propellant Options for High-Power Hall Thrusters," in *41st AIAA/ASME/SAE/ASEE Joint Propulsion Conference & Exhibit*, Tucson, July 2005.

[28] W. A. Hargus Jr. and J. Strafaccia, "Optical Boron Nitride Insulator Erosion Characterization of a 200W Xenon Hall Thruster," in *Joint Propulsion Conference*, vol. Joint Propulsion Conference, Tuscon, 2005.

[29] J. M. Ekholm and W. A. Hargus Jr., "Highly Oblique Ion Species Fraction Measurements of a 200W Xenon Hall Thruster," Air Force Research Laboratory, Edwards AFB, 2005.

[30] J. M. Ekholm and W. A. Hargus Jr., "EXB Measurements of a 200W Xenon Hall Thruster," Air Force Research Laboratory, Edwards AFB, 2007.

[31] K. A. Polzin et al., "Performance of a Permanent-Magnet Cylindrical Hall-Effect Thruster," in *45th AIAA/ASME/SAE/ASEE Joint Propulsion Conference & Exhibit*, Denver, CO, Aug 2009.

[32] T. Ito et al., "Experimental Characterization of a Micro-Hall Thruster," vol. 23, no. 5, pp. 1068-1074, Sep-Oct 2007.

[33] N. B. Meexan, N. Gascon, and M. A. Cappeli, "Linear Geometry Hall Thruster with Boron Nitride and Diamond Walls," in *27th International Electric Propulsion*

Conference, Pasadena, Oct 2001.

[34] A. Smirnov, Y. Raitses, and J. Fisch, "The Effect of Magnetic Field on the Performance of Low-Power Cylindrical Hall Thrusters," in *29th International Electric Propulsion Conference*, Princeton, NJ, Nov 2005.

[35] A. N. Smirnov, Y. Raitses, and N. J. Fisch, "Electron Cross-Field Transport in a Miniturized Cylindrical Hall Thruster," *IEEE Transactions on Plasma Science*, vol. 34, no. 2, pp. 132-141, Apr 2006.

[36] W. A. Hargus Jr. and M. R. Nakles, "Hall Effect Thruster Ground Testing Challenges," *25th Aerospace Testing Seminar*, Octover 2009.

[37] K. A. Polzin et al, "Thrust Stand for Electric Propulsion Evalutaion," vol. 77, pp. 105-108, 2006.

[38] J. J. Selstrom, "Thrust and Performance Study of Micro Pulsed Plasma Thrusters," Dayton, 2010.

[39] D. M. Goebel and R. M. Watkins, "LaB6 Hollow Cathodes for Ion and Hall Thrusters," vol. 41st AIAA/ASME/SAE/ASEE Joint Propulsion Conference & Exhibit, July 2005.

[40] D. M. Goebel, J. T. Crow, and A. T. Forrester, "Lanthanum Hexaboride Hollow Cathode for Dense Plasma Production," pp. 469-472, December 1978.

[41] MKS Instruments, "ALTA Series True Digital Mass FLow Meter/Controller with Analog I/O Instruction Manual," Wilmington, MA, 2004.

[42] J. E. Rotter, "An Analysis of Multiple Configurations of Next-Generation Cathodes in a Low Power Hall Thruster," Dayton, 2007.

[43] C. Farnell and J. D. Williams, "Faraday Probe Operating Manual," Fort Collins, Instrument Manual 2007.

[44] S. E. Tempkin, "Performance Characterization of a Three-Axis Hall Effect Thruster," Dayton, OH, 2010.

[45] Schaevitz Sensors, "Schaevitz MP Series Microprocessor-Based LVDT Readout/Controller Operating Instructions," Hampton, VA, User Manual 2007.

[46] Thermo Scientific, "NESLAB RTE Series Refrigerated Bath," Newington, NH, User Manual 2007.

[47] Busek Co. Inc., "Torsional Balance System," Natick, MA, Operation Manual Oct 2007.

[48] Y. Azziz, "Experimental and Theoretical Characterization of a Hall Thruster Plume," Department of Aeronautics and Astronautics, Massachusetts Institute of Technology, Boston, MA, PhD Dissertation 2007.

[49] Y. Azziz, "Instrument Development and Plasma Measurements on a 200-Watt Hall Thruster," Boston, Master's Thesis June 2003.

[50] A. Shirasaki and H. Tahara, "Plume Measurements and Miniturization of the Hall Thrusters with Circular Cross-Sectional Discharge Chambers," , Princeton, Nov 2005.

[51] Y. Raites et al., "Effect of the Magnetic Field on the Plasma Plume of the Cylindrical Hall Thruster with Permantent Magnets," , Nashville, Jul 2010.

[52] Y. Raitses et al., "Cylindrical Hall thrusters with permanent magnets," *Journal of Applied Physics*, vol. 108, no. 9, Nov 2010.

[53] J. D. Dommerville and L. B. King, "Effect of Cathode Position on Hall-Effect Thruster Performance and Cahtode Coupling Voltage," , Cincinnati, Jul 2007.

[54] J. W. Tomaszewski, "Characterization of a Hall Effect Thruster Using Thermal Imaging," Dayton, 2007.

[55] T. S. Matlock, W. A. Hargus Jr., and C. W. Larson, "Thermographic Characterization and Comparison of 200W and 600W Hall Thrusters," vol. 43rd AIAA/ASME/SAE/ASEE Joint Propulsion Conference, July 2007.

[56] B. K. Morgan, "Building of a Laser Diagnostic Tool to Measure the Ion Velocity in a Low Power Hall Thruster," Dayton, 2010.

[57] M. Matsui et al., "Number Density Distribution of Xenon Atoms in Hall Thruster Plumes," vol. 43rd AIAA/ASME/SAE/ASEE Joint Propulsion Conference & Exhibit, July 2007.

Vita

Captain John-David C. de La Harpe attended the University of Portland under the Air Force's Reserve Officers' Training Corps scholarship program and graduated magna cum laude with a Bachelor of Science degree in Mechanical Engineering in 2006. He was commissioned a Second Lieutenant in the United States Air Force in December 2005 and attended the Air and Space Basic Training Course in January 2006 where he received awards for Outstanding Academic Performer, Top Flight, and Most Athletic Flight.

Captain de La Harpe's first assignment was working in the Air Force Research Laboratory's Air Vehicles Directorate. He managed projects and performed exploratory research in the area of conformal load bearing antenna structures. During his four years in the research laboratory, he also completed his Master's in Business Administration degree from The Ohio State University, graduating with honors.

In 2009, Captain de La Harpe reported to the Air Force Institute of Technology. Following his graduation from AFIT he will move to Colorado Springs to work for the Space Innovation and Development Center at Schriever Air Force Base.

REPORT DOCUMENTATION PAGE		Form Approved OMB No. 0704–0188

1. REPORT DATE (DD–MM–YYYY)	2. REPORT TYPE	3. DATES COVERED (From — To)
24-03-2011	Master's Thesis	September 2009 – March 2011

4. TITLE AND SUBTITLE	5a. CONTRACT NUMBER
Performance Characterization of a Novel Plasma Thruster to Provide a Revolutionary Operationally Responsive Space Capability with Micro- and Nano-Satellites	5b. GRANT NUMBER
	5c. PROGRAM ELEMENT NUMBER
6. AUTHOR(S) de La Harpe, John-David C., Captain, USAF	5d. PROJECT NUMBER
	5e. TASK NUMBER
	5f. WORK UNIT NUMBER
7. PERFORMING ORGANIZATION NAME(S) AND ADDRESS(ES) Air Force Institute of Technology Graduate School of Engineering and Management (AFIT/ENY) 2950 Hobson Way WPAFB OH 45433-7765	8. PERFORMING ORGANIZATION REPORT NUMBER AFIT/GA/ENY/11-M02
9. SPONSORING / MONITORING AGENCY NAME(S) AND ADDRESS(ES) Air Force Research Laboratory Space and Missile Propulsion Division Att: Mr. Michael Huggins (Michael.Huggins@edwards.af.mil) 1 Ara Rd. Edwards, AFB CA 93524	10. SPONSOR/MONITOR'S ACRONYM(S) AFRL/RZS
	11. SPONSOR/MONITOR'S REPORT NUMBER(S)

12. DISTRIBUTION / AVAILABILITY STATEMENT
APPROVED FOR PUBLIC RELEASE; DISTRIBUTION UNLIMITED

13. SUPPLEMENTARY NOTES
This material is a declared work of the U.S. Government and is not subject to copyright protection in the United States.

14. ABSTRACT
Few options currently exist to provide propulsion for extremely small satellites due to design constraints on power, volume, and weight. However, future operation will require a capability to conduct orbital maneuvers, momentum dumping, and precision pointing for these low cost satellites. The research presented here represents the first effort to operate and quantify the performance of a new micro plasma thruster design which provides a novel solution to these disparate competing constraints. The thruster in this study represents a deviation from traditional circular Hall thruster design practices, because it eschews a central magnetic circuit, which results in nearly parallel electric and magnetic field lines within the thruster discharge channel. This design decision reduces thruster complexity and thermal susceptibility, but it also reduces the ionization efficiency. The cornerstone of this study involved the direct measurement of thrust in order to quantify the efficiency and specific impulse of this innovative thruster. The investigation also included characterization of the thruster exhaust plume, voltage-current characteristics, and operating limits. Results are enumerated and suggestions for improvement provided.

15. SUBJECT TERMS
Space Propulsion, Hall Thruster, CubeSat

16. SECURITY CLASSIFICATION OF:			17. LIMITATION OF ABSTRACT	18. NUMBER OF PAGES	19a. NAME OF RESPONSIBLE PERSON
a. REPORT	b. ABSTRACT	c. THIS PAGE	UU	137	Richard E. Huffman, Jr., Lt Col, USAF
U	U	U			19b. TELEPHONE NUMBER (Include Area Code) (937) 255-6565, ext 7490 Email: (richard.huffman@afit.edu)

Standard Form 298 (Rev. 8–98)
Prescribed by ANSI Std. Z39.18